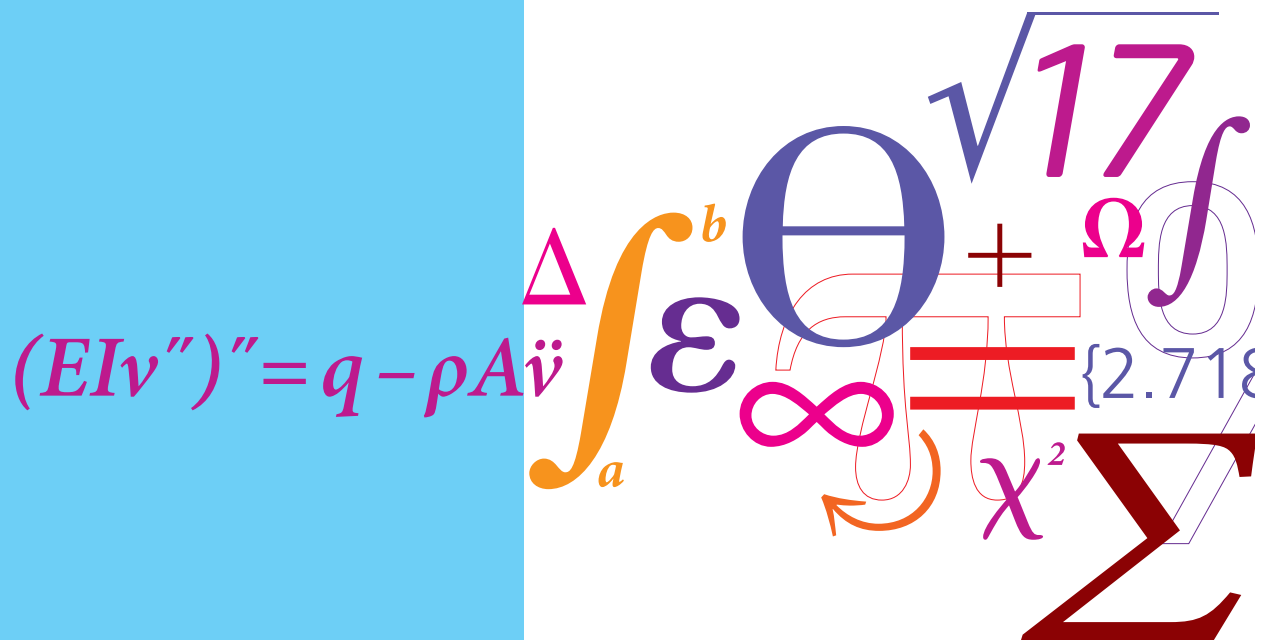


Design of advanced materials for linear and nonlinear dynamics

PhD Thesis



Niels Morten Marslev Frandsen
 DCAMM Special Report No. S201
 April 2016

PhD Thesis:

Design of advanced materials for linear and nonlinear dynamics

April 30, 2016

by

Niels Morten Marslev Frandsen

Supervisors

Professor Jakob Søndergaard Jensen
Associate Professor Jon Juel Thomsen



Technical University of Denmark

DTU Mechanical Engineering
Department of Mechanical Engineering

Title of the thesis:

Design of advanced materials for linear and nonlinear dynamics

PhD Student:

Niels Morten Marslev Frandsen

E-mail: nimmfr@mek.dtu.dk

Supervisors:

Jakob Søndergaard Jensen

E-mail: json@elek.dtu.dk

Jon Juel Thomsen

E-mail: jjt@mek.dtu.dk

Address:

Department of Mechanical Engineering, Solid Mechanics

Technical University of Denmark

Nils Koppels Allé, Building 404

2800, Kgs. Lyngby

Denmark

Copyright ©2016 Niels Morten Marslev Frandsen

DCAMM Special Report no. S201

ISBN: 978-87-7475-450-3

PREFACE

This thesis is submitted in partial fulfilment of the requirements for obtaining the Danish PhD degree. The work has been carried out primarily at the Section of Solid Mechanics (FAM), Department of Mechanical Engineering (MEK) at the Technical University of Denmark (DTU) under the supervision of Professor Jakob Søndergaard Jensen and Associate Professor Jon Juel Thomsen. Part of the work was carried out at the Department of Aerospace Engineering Sciences at the University of Colorado Boulder, in collaboration with Associate Professor Mahmoud I. Hussein and (at the time) PhD student Osama R. Bilal. The work has been funded by the ERC Starting Grant no. 279529 INNODYN.

I would like to extend my deepest gratitude to both the main supervisor, Jakob S. Jensen and co-supervisor, Jon J. Thomsen. Throughout the project period, Jakob has shown great patience with me and entertained my (sometimes unrealistic) ideas for the next step in the research, while keeping me from straying too far from the road of realistic achievements. Both Jakob and Jon have provided invaluable advice and constructive feedback, continually pushing the project in the right direction. I would also like to offer my appreciation to Dr. Hussein for hosting me at the University of Colorado, Boulder, during the fall 2014/winter 2015. A major part of this thesis was founded by the work that I did while visiting Dr. Hussein and his research group, and in particular Dr. Osama R. Bilal deserves recognition for his constant availability as a sparring partner.

Furthermore, I would like to thank my colleagues for providing a pleasant working environment and in particular my fellow PhD students in Office 131, Rasmus Ellebæk Christiansen and Christopher Nelleman, deserves acknowledgement for our fruitful discussions on the mathematical representation and physical behaviour of wave and vibration related phenomena as well as always providing valuable second opinions. Moreover, the insisting by Rasmus on keeping any presentation mathematically strict and self-contained yet still simple has definitely improved my presentations over the years.

Finally, I would like to thank mechanical engineer Jonas Syders Knudsen for his constructive feedback on the prepared manuscript, and last but definitely not least, my wife Mirja Frello Hansen deserves an enormous praise for her support during the entire project period, and in particular for her patience during the final intense months of finishing the manuscript. She, and our son Aske, are continuous sources of inspiration and motivation to me.

Lyngby, April 2016

Niels Frandsen

ABSTRACT

The primary catalyst of this PhD project has been an ambition to design advanced materials and structural systems including, and possibly even exploiting, nonlinear phenomena such as nonlinear modal interaction leading to energy conversion between modes. An important prerequisite for efficient design is accurate and somewhat simple analysis tools, as well as a fundamental understanding of the physical phenomena responsible for the relevant effects. The emphasis of this work lies primarily in the investigation of various advanced material models, developing the necessary analytical tools to reveal the fundamental dynamic characteristics and thus the relevant design parameters.

The thesis is built around the characterization of two one-dimensional, periodic material systems. The first is a nonlinear mass-spring chain with periodically varying material properties, representing a simple but general model of inhomogeneous structural materials with nonlinear material characteristics. The second material system is an “engineered” material in the sense that a classical structural element, a linear elastic and homogeneous rod, is “enhanced” by applying a mechanism on its surface, amplifying the inertia of the system, thus creating a new “material” with improved properties for wave attenuation.

Both materials are investigated by Floquet-Bloch analysis, a powerful tool for determining the dynamic material characteristics of periodic materials. An asymptotic approach is utilized for the direct application of the Floquet-Bloch analysis on the nonlinear chain. The wave-characteristics are determined, exploring the effect of nonlinear modal interaction on the band structure as well as the potential for energy conversion through higher harmonic generation. While modal interaction definitely affects the band structure, the potential for energy conversion appears to be limited. The material with amplified inertia however, shows great promise for low-frequency and broadband wave attenuation, requiring a significantly lower mass than what is needed in comparable systems to obtain a similar effect. This is demonstrated both analytically, numerically and experimentally. This makes the material a strong candidate for mechanical filtering for sound and vibration isolation purposes, not least for systems with varying natural frequencies such as nonlinear structures or structures with variable mass due to, e.g., human loading.

DANSK RESUMÉ

Den primære katalysator til dette ph.d.-projekt har været en ambition om at designe avancerede materialer og strukturelle systemer, der inkluderer, og måske endda udnytter, ikke-lineære fænomener som eksempelvis ikke-lineær modal interaktion, der kan føre til energikonvertering mellem svingningsformer. En vigtig forudsætning for effektivt design er nøjagtige og relativt simple analyseværktøjer samt en grundlæggende forståelse for de fysiske fænomener, der ligger til grund for de pågældende effekter. Hovedvægten af dette arbejde er på at undersøge forskellige avancerede materialemodeller og dermed udvikle de nødvendige analytiske værktøjer til at bestemme de grundlæggende dynamiske egenskaber.

Afhandlingen er fokuseret på karakteriseringen af to en-dimensionale, periodiske materialsystemer. Det første er en ikke-lineær masse-fjeder kæde med periodisk varierende materialeegenskaber, der repræsenterer en simpel men generel model for inhomogene strukturelle materialer med ikke-lineære materialeegenskaber. Det andet materiale er et "konstrueret" materiale i den forstand, at et klassisk strukturelt element, en lineær elastisk og homogen stang, er "forbedret" ved at en mekanisme, designet til at forsærke stangens inert, påføres stangens overflade. Således skabes et nyt "materiale" med forbedrede bølgedæmpningsegenskaber.

Begge materialer undersøges ved Floquet-Bloch-analyse som er et kraftfuldt værktøj til bestemmelse af de dynamiske materialeegenskaber for periodiske materialer. Der benyttes en asymptotisk metode for at kunne anvende Floquet-Bloch analysen direkte på den ikke-lineære kæde. Kædens bølgeudbredelses-karakteristika bliver bestemt, hvorved effekten af modal interaktion på båndstrukturen samt potentialet for energikonvertering via generation af højere harmoniske bølger undersøges. Hvor modal interaktion bestemt påvirker båndstrukturen, lader potentialet for energikonvertering til at være begrænset. Materialet med forstærket inert viser sig dog meget lovende for lavfrekvent og bredspektret bølgedæmpning, endda ved en betydeligt lavere masse end der er behov for i sammenlignelige systemer for at opnå en lignende effekt. Dette er påvist både analytisk, numerisk og eksperimentelt. Dermed er materialet en stærk kandidat til et mekanisk filter der kan bruges til isolering af lyd eller vibrationer. Ikke mindst for systemer med varierende egenfrekvenser såsom ikke-lineære konstruktioner eller konstruktioner med variabel masse forårsaget af eksempelvis menneskelig belastning.

PUBLICATIONS

The following publications are a part of the PhD thesis.

- [P1] Frandsen, N. M. M. and Jensen, J. S. (Under Review). “Modal Interaction and Higher Harmonic Generation in a Weakly Nonlinear, Periodic Mass-Spring Chain”. *Wave Motion*.
- [P2] Frandsen, N. M. M., Bilal, O. R., Jensen, J. S. and Hussein, M. I. (2016). “Inertial Amplification of Continuous Structures - Large Band Gaps from Small Masses”. *Journal of Applied Physics* **119**, 124902.

Contents

Preface	i
Abstract	ii
Dansk Resumé	iii
Publications	iv
Contents	v
1 Introduction	1
1.1 Periodic material/structural design	1
1.2 Why nonlinearity?	1
1.3 Original contributions and structure of the thesis	3
2 Fundamentals	5
2.1 Periodic systems	5
2.1.1 Band diagrams	6
2.1.2 Band gaps	7
2.1.3 Band gap mechanisms	10
2.2 Nonlinear systems	12
2.2.1 Sources of nonlinearity	12
2.2.2 Effects of nonlinearity	14
3 Nonlinear periodic materials	19
3.1 A simple material model	19
3.1.1 Nonlinear dispersion shifts	20
3.1.2 Generation of higher harmonics	23
4 Inertial amplification	29
4.1 A brief historical account	29
4.2 Inertial amplification of continuous structures	31
4.3 Band structure	32
4.3.1 Attenuation profiles	34
4.3.2 Performance compared to other methods	37

4.4	Band gap limits and antiresonances	38
4.4.1	Low-frequency gap design	40
5	Inertial amplification extensions	45
5.1	Is it real?	45
5.1.1	Flexible connecting beams	45
5.1.2	Experimental transverse vibrations	48
5.2	Nonlinear kinematics	54
5.2.1	Governing equations	54
5.2.2	Numerical experimental setup	55
5.2.3	Simulation results	56
6	Concluding remarks	59
6.1	Modal interaction and energy conversion in nonlinear, periodic materials	59
6.2	Low-frequency and broadband wave attenuation by inertial amplification	60
6.3	Future work	60
	References	62
A	Modal expansion	67
B	Numerical model for nonlinear inertial amplification	71
B.1	Nonlinear kinematics	71
B.2	Nonlinear constraint forces	72
B.2.1	Approximation	73
B.3	Discretized hybrid system	74
B.3.1	State space format	75
[P1]	Modal Interaction and Higher Harmonic Generation in a Weakly Nonlinear, Periodic Mass-Spring Chain	77
[P2]	Inertial Amplification of Continuous Structures - Large Band Gaps from Small Masses	95

Chapter 1

Introduction

The present thesis is concerned with the dynamics of advanced material and structural systems. The systems considered are generally periodic materials or structures, some of which also exhibit nonlinear characteristics. Part of the motivation for considering periodicity and nonlinearity is found in the fact that both phenomena introduce interesting dynamic effects that might be utilized for improved dynamic performance. Further motivation is found in the fact that both phenomena are frequently encountered in nature, and thus also in science and technology. In particular the quest for optimized designs in terms of, e.g., longer/taller, more slender and light-weight structures as well as the continuous effort to optimize the performance of various dynamic system components, increase the significance of nonlinearity in material and structural dynamics.

1.1 Periodic material/structural design

Periodicity is often found in nature, from the small scale crystal lattice structures found in, e.g., salt and crystalline metals, to the cancellous part of the human bone and the honeycomb structures of beehives. The latter two have served heavily as inspiration to engineering design, and in particular the honeycomb structure has become so synonymous with aerospace structures, due to its beneficial stiffness/density ratio, that some might even have forgotten its natural origin. In addition to the nature-inspired engineering designs, periodicity is often practical or even a simple consequence of designs as in railroads, multispan bridges, high-rises or ribbed plates. Since the periodicity is there, we might as well utilize it in the design. This is a main theme of this thesis, considering two different types of periodic materials in [P1] and [P2] respectively.

1.2 Why nonlinearity?

Where the natural occurrence of periodicity is widely accepted in practical engineering design due to its beneficial effects, the presence of nonlinearity seems to represent more of a discrepancy between academia and the industry. The disregard of nonlinearities in practical engineering design conflicts slightly with the (paraphrased) quote presented to the author

during the introduction to an advanced vibration class:

“The real world is nonlinear, so your analysis better also be!”

which, while obviously biased by the subject matter of the class, and a somewhat crude representation, holds a great deal of significance. A more moderate statement, however, might be that:

“The real world operates in various ranges, so base your analysis accordingly!”

lacking the cut-throat nature of the original quote, but presenting a bit more nuanced perspective. The fact that linear analysis and design is so widely used in practice is often written off, by the nonlinear community, as the consequence of well-established linear mathematical methods and models, along with the increased complexity of nonlinear analysis. While this is probably partly true, another relevant argument is, that many systems are designed to operate in the linear regime, whereby a full nonlinear analysis might be superfluous. The question is then, *why* are systems designed to operate in the linear regime? The answer to that, in the the author’s opinion, falls within three categories.

1. Nonlinear analysis is complex and has a poor cost/benefit value.
2. Nonlinearity is the enemy and we must kill it!
3. Various system requirements leads to the linear range being “optimal”.

The first category has already been mentioned, while the second represents a common frame of mind in practical engineering design sometimes coupled with the third. Examples of the third include situations where spatial constraints between connecting structural elements enforces a specific requirement on, e.g., the displacement range; or comfort requirements of dynamically prone structures, enforcing a maximal acceleration of the structure. It is certainly true that reaching the nonlinear regime often leads to problems, e.g., when a column buckles, the nonlinear deformed shape is primarily of academic interest since the supported structure may have fallen down, nonlinear analysis or not. In terms of dynamic systems, an often used method for mitigating vibrations is the tuned mass damper (TMD), which is tuned to a specific resonance frequency. An effect of nonlinearity is that the resonance frequency of the structure changes with vibration amplitude, whereby the TMD will become mis-tuned and lose a great deal of efficacy. This problem can be resolved by enforcing a similar nonlinearity on the TMD as the host structure exhibits, as illustrated by Viguié & Kerschen (2009). This approach however, is still based on the notion of reacting to nonlinearity, i.e., detect nonlinearity and solve the problem. Another philosophy is to design nonlinear systems to obtain desirable properties by *utilizing* nonlinearities, as done for the frequency splitter in Qalandar, Strachan, Gibson, Sharma, Ma, Shaw & Turner (2014). The present thesis considers the problem of utilizing nonlinearities on a very initial stage, investigating the potential of the nonlinear, periodic material presented in [P1] to transfer vibration energy from one mode to another by nonlinear modal interaction.

1.3 Original contributions and structure of the thesis

Chapter 2 presents an introduction to the two central concepts of this thesis - periodic materials and nonlinearity. The chapter is intended to provide the reader with sufficient background information to benefit from the thesis, without drowning him/her with an abundance of very general and complicated theory.

Chapter 3 presents a nonlinear periodic material model which is analyzed in [P1]. Wave propagation in the material is investigated by an asymptotic solution approach, revealing modal interaction effects on the band structure of the material. Compared to the wave-interaction considered for a mono-atomic chain in Manktelow, Leamy & Ruzzene (2011) and the general 1,2 and 3-dimensional, multi-degree of freedom structures in Manktelow, Leamy & Ruzzene (2014*b*), the effects presented here arise from modal self-interaction rather than from the interaction with an injected control wave. The asymptotic approach is also used to investigate higher harmonic generation in the material, the results of which are verified by numerical simulations within the limits of the asymptotic approach. The focus is on the possibility for controlling the higher harmonic generation by manipulating, e.g., the nonlinear stiffness, and the potential for maximizing energy transfer to a higher mode. Previously the investigations into higher harmonic generation in nonlinear chains have focused on the existence and importance of an evanescent higher harmonic on the fundamental wave as demonstrated for finite chains with quadratic nonlinearity, both experimentally in Cabaret, Tournat & Béquin (2012) and numerically in Sánchez-Morcillo, Pérez-Arjona, Romero-García, Tournat & Gusev (2013). The higher harmonic generation in the model presented in [P1], and thus the potential for modal energy conversion, is seen to be limited however, at least within the constraints of the asymptotic approach. Recently, Ganesh & Gonella (2015) explored the concept of “mode-hopping” in a significantly more complex chain than considered in [P1], numerically and experimentally presenting a significant amount of modal energy transfer. In terms of finite structures, Dou & Jensen (2015) uses topology optimization on a doubly clamped beam to minimize and maximize the sub- and superharmonic resonance of the beam, where the emphasis here is towards a more general material description rather than a specific structure.

Chapter 4 introduces a novel application of a known mechanical filtering concept, where waves in continuous media are attenuated by periodically applying a mechanism designed to enhance the inertia of the host medium, a concept known as *inertial amplification*. The generic mechanical element providing inertial amplification is known as the *inserter*, (Smith 2002), however the phenomena can be realized by masses and levers as well. The inserter concept is utilized in the design of suspension systems for, e.g., Formula One racers, (Chen, Papageorgiou, Scheibe, Wang & Smith 2009) and optimization of base-isolation systems in Hu, Chen, Shu & Huang (2015). More recently, Krenk & Høgsberg (2016) developed an explicit design procedure for implementing an inserter-based system for resonant vibration damping of flexible structures. Inertial amplification has received limited attention in terms of wave attenuation in periodic structures, however Yilmaz and collaborators have revived the concept somewhat in recent years. In Acar & Yilmaz (2013), they utilize the concept by generating periodic lattice structures from unit cells designed for inertial amplification, while the effect of

inertial amplification mechanisms on FCC and BCC lattices is considered in Taniker & Yilmaz (2013). Recently, Yuksel & Yilmaz (2015) employed shape optimization to improve the band gap characteristic of the unit cell design in (Acar & Yilmaz 2013). The direct application of an inertial amplification mechanism to the surface of a continuous structure, as considered in [P2], has not been seen before. The continuous nature of the host structure increases the richness of the problem, while the surface-application of the mechanism is expected to allow for applying it directly on the surface of existing structures exhibiting dynamic problems. The attenuation effect works over a comparably large frequency range, making the material a promising candidate for practical wave and vibration mitigation systems.

Chapter 5 presents a number of extensions to the inertial amplification system from Chapter 4. The extensions include a relaxation of some of the idealizing assumptions made in [P2], illustrating that the concept does indeed have a practical potential, even in the presence of nonlinearity. The nonlinearity arises from the applied mechanism itself, and the focus is on investigating whether this nonlinearity impairs the filter properties determined by the linear analysis. This is done by numerical experiments of a single unit cell, applying harmonic loading within the band gap predicted by the linear model. This is similar to the investigation in Yousefzadeh & Phani (2015), however focusing on multiple harmonics rather than a transmission threshold and considering a single unit-cell rather than a periodic structure.

The practical applicability of the concept is further validated by experimental results for an inertial amplification system for transverse vibrations. The experiments were conducted as part of an M.Sc.-project, carried out by Mr. Mateusz Barys and supervised by Professor Jakob Søndergaard Jensen and myself.

My intention has been to make the thesis as enjoyable as possible, keeping the language light and level of technical detail to what is needed to explain the presented physical phenomena. Hence, the thesis should be readable by most people with a background in civil/mechanical engineering and knowledge of material/structural dynamics. Complex mathematics and algebra have been contained in the appended papers, [P1] and [P2], as well as in the appendices. Chapter 5 is slightly more technical than Chapters 1-4, however the preceding chapters should work as a preparation for the increased technical detail presented in Chapter 5.

Chapter 2

Fundamentals

This chapter is devoted to two very central concepts within the thesis, both of which have been briefly mentioned in the introduction. The chapter is intended to provide a general description of the, for the present work, relevant effects of periodicity and nonlinearity in structural and material dynamics, rather than an exhaustive account of either concept. The primary distinction made between material and structural dynamics here, is the presence of boundary conditions. Hence, an infinite medium is considered a material whereas a medium of finite extent is considered a structure. Which description is used depends primarily upon the purpose of the analysis, i.e., the description that is most convenient for obtaining the sought insights into the governing dynamics of the system will be used.

2.1 Periodic systems

A *periodic system* is, within this thesis, to be understood as a material or structure with a periodically repeating feature, such as periodically varying material properties or dimensions, periodic boundary conditions or periodically applied devices such as local resonators. Figure 2.1 shows three schematics of some commonly analyzed types of periodicities in material and structural dynamics, with the period indicated by a .

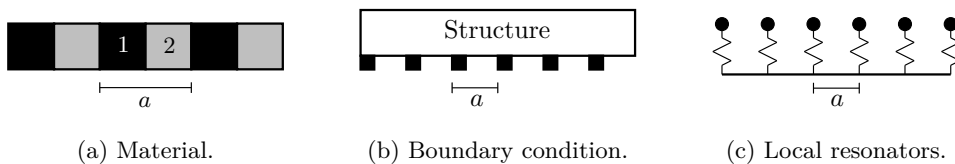


Figure 2.1: Schematics of various periodicities.

Periodic materials and structures are, in newer literature, often termed *phononic* materials and structures, probably inspired by research surge in *photonic* materials and structures developed for optical waves. The motivation for investigating periodic systems is two-fold. First of all, engineering structures often possess some form of periodicity, e.g., multi-span bridges, stiffened plates, multi-blade turbines and composite materials. Secondly, periodicity results in

some interesting effects that might be utilized for increasing the performance of a material or structure. The effect of primary importance for this thesis - the generation of band gaps - is presented in Section 2.1.2. A general introduction on wave-propagation in periodic structures can be found in Brillouin (1953), while the review papers (Elachi 1976, Mead 1996, Hussein, Leamy & Ruzzene 2014) provide an excellent account of the research carried out in the field since the 1950's. In particular, the civil engineer with a background in structural dynamics (i.e., the author's background), will enjoy the excellent paper by Mead (1996).

2.1.1 Band diagrams

The material description is often used to analyze the wave-characteristics of a system, since this description lends itself very well to wave-solutions. In particular the relation between wavenumber (or wavevector) and frequency, known as the dispersion relation, is of cardinal importance since it relates the spatial (wavenumber or wavelength) and temporal (frequency or period) characteristics of the wave. Hence, it represents the wave-equivalent of the relation between mode shape (spatial characteristic) and natural frequency (temporal characteristic) for structural systems.

The dispersion relation is graphically illustrated by the *band diagram* or *band structure*, depicting the propagation frequency as a function of the wavenumber. The propagation frequency of longitudinal waves in a linear, homogeneous medium is a linear function of the wavenumber, while flexural waves (in the presence of flexural stiffness) have a quadratic dependence between propagation frequency and wavenumber. The wave-description provides a continuous development of propagation frequency with wavenumber, while the structural description provides the discrete points in this spectrum, since the boundary conditions only allow for certain natural standing waves in the structure. As an example, the mode shapes, φ_n , and natural frequencies, ω_n , for longitudinal and transverse vibrations of a general fixed-free beam with stiffness E , density ρ and length l , are given as, (Inman 2009):

$$\varphi_n^l = \sin \mu_n^l x, \quad \omega_n^l = \mu_n^l \sqrt{\frac{E}{\rho}}, \quad (2.1a)$$

$$\varphi_n^t = \cosh \mu_n^t x - \cos \mu_n^t x - \sigma_n (\sinh \mu_n^t x - \sin \mu_n^t x), \quad \omega_n^t = (\mu_n^t)^2 \sqrt{\frac{EI}{\rho A}}, \quad (2.1b)$$

where A and I are the area and second moment of area of the beam respectively. The wavenumbers μ_n (and the constants σ_n) are determined by the boundary conditions, and in turn, so are the natural frequencies. The wave length of the (harmonic part of the) mode shape is $\lambda_n = 2\pi/\mu_n$. Figure 2.2 illustrates the longitudinal (dashed black) and flexural (solid black) dispersion curve for a general beam of a homogeneous material, along with the first few natural frequencies for some common boundary conditions (various markers). The wavenumber and natural frequency of the second longitudinal and transverse mode of the beam example in Eqs. (2.1) have been indicated by blue and red dash-dot lines respectively.

This basic relation between propagating-wave characteristics and fundamental frequencies

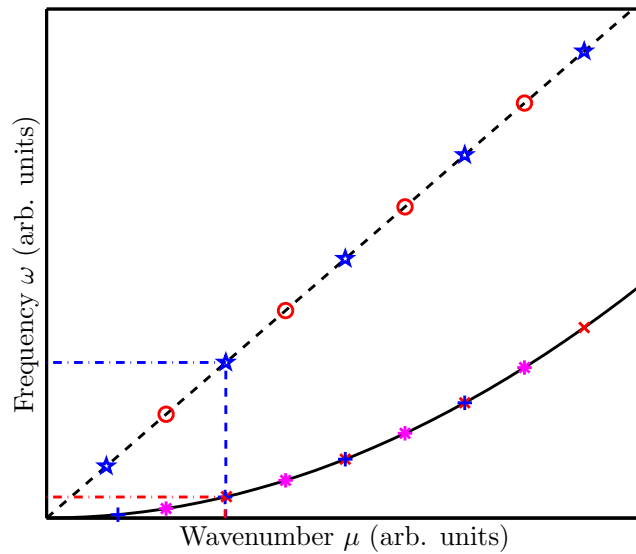


Figure 2.2: Dispersion versus natural frequencies.

is by no means ground-breaking, but serves to highlight the relation between waves and vibrations, and thus, between materials and structures.

2.1.2 Band gaps

A *band gap* is a gap in the band structure of the material, sometimes also termed a stop band. Considering the band structure in Fig. 2.2, a complete gap in the band structure would mean that for a certain frequency range - the gap range - waves could not propagate, and as a direct consequence, no resonances would fall within this range, regardless of boundary conditions. This possibility of designing the dynamics in a general way is very appealing and, unfortunately, a bit of a simplification. Going from the infinite to the finite case introduces boundary effects which can be more or less profound. Before this is illustrated, a brief introduction to the analysis of periodic materials is given. The introduction is given by example, using a simple one-dimensional system that is sufficient for illustrating the various effects without complicating the demonstration with an unnecessary general presentation. Consider the infinite bi-material rod in Fig. 2.3 made up of the two materials denoted 1 and 2.

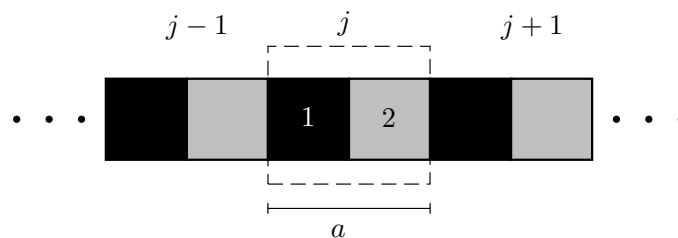


Figure 2.3: Bi-material rod.

The dashed box indicates the *unit cell* number j , while the period is given by the distance a .

For a wave travelling through the material at wavenumber μ and frequency ω , the dispersion relation describes the relation between ω and μ . The periodicity of the system causes the frequency to be periodic in the wavenumber as well, (Brillouin 1953), i.e.,

$$\omega(\mu) = \omega\left(\mu \pm j\frac{2\pi}{a}\right), \quad (2.2)$$

hence, it is sufficient to consider a partial range of the wavenumber when determining the band structure. This range is usually referred to as the *first Brillouin Zone* after the French physicist Léon Brillouin, whose book on wave propagation in periodic structures, (Brillouin 1953), provides an excellent introduction to and description of the topic. Particularly the first chapter is a great read for anyone with a scientific inclination, providing a brief historical description of the research in periodic materials and structures ranging from Newton in 1686 to Born in 1912. It is of interest that Brillouin himself notes the ambiguity of the dispersion when frequency is a periodic function of wavenumber since this means that an infinite number of waves correspond to the same frequency. The problem is dismissed with an argument of only disregarding a limited number of wavelengths when considering the first Brillouin Zone. While this is correct in the framework of the book, one should keep this limitation in mind when analyzing periodic systems, since the effect of the ambiguity presents itself on occasion, as will be illustrated by example shortly.

In addition to periodicity of the dispersion relation, the periodicity of the system also implies periodicity of the *solution*, i.e., the wave-field in the system. This is described by the paramount *Floquet-Bloch* theorem generally attributed to the mathematician Gaston Floquet and the physicist Felix Bloch. Floquet dealt with one-dimensional first-order differential equations with periodic coefficients, (Floquet 1883), while Bloch dealt with quantum theory of solids, describing the dynamics of electrons in crystal lattices, (Bloch 1929). The periodicity of the solution means that for the example in Fig. 2.3, the motion at points separated by one period can be related by a phase multiplier, i.e., if the motion of the material at position x and time t is given by $u(x, t)$, the Floquet-Bloch theorem states that

$$u(x + ja, t) = u(x, t)e^{i\mu ja} \quad (2.3)$$

where i is the imaginary unit. Hence the solution at any point can be determined by considering only the fundamental unit cell of the system.

Returning to the two-phase material in Fig. 2.3, the band structure can be determined by utilizing the Floquet-Bloch theorem. The band structure for the material will be compared to the natural frequencies and modes for two finite structures consisting of five unit cells, shown in Figure 2.4, where the unit cells are marked by dashed boxes.

Note that the finite structure in Figure 2.4a has an additional layer of “material 1” padded at the right end in order to make it symmetric, while the finite structure in Figure 2.4b is five unit cells without additional modifications. This symmetry breaking has consequences in terms of the relation between the band structure for the material and the natural modes of the finite structure, due to the existence of *localized modes* on the boundary of the structure. Figure 2.5 illustrates the band structure of the two-phase material along with the natural frequencies for the two systems in Figure 2.4. The wavenumbers of the natural frequency

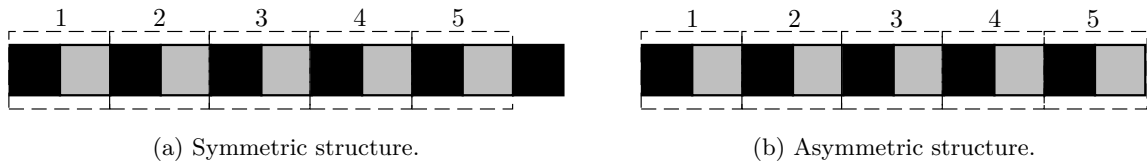


Figure 2.4: Finite structures.

points have been obtained by a spatial Fourier transform of the mode shape vector, hence the points indicate the wavenumber of the dominant part of the assumed harmonic deformed shape.

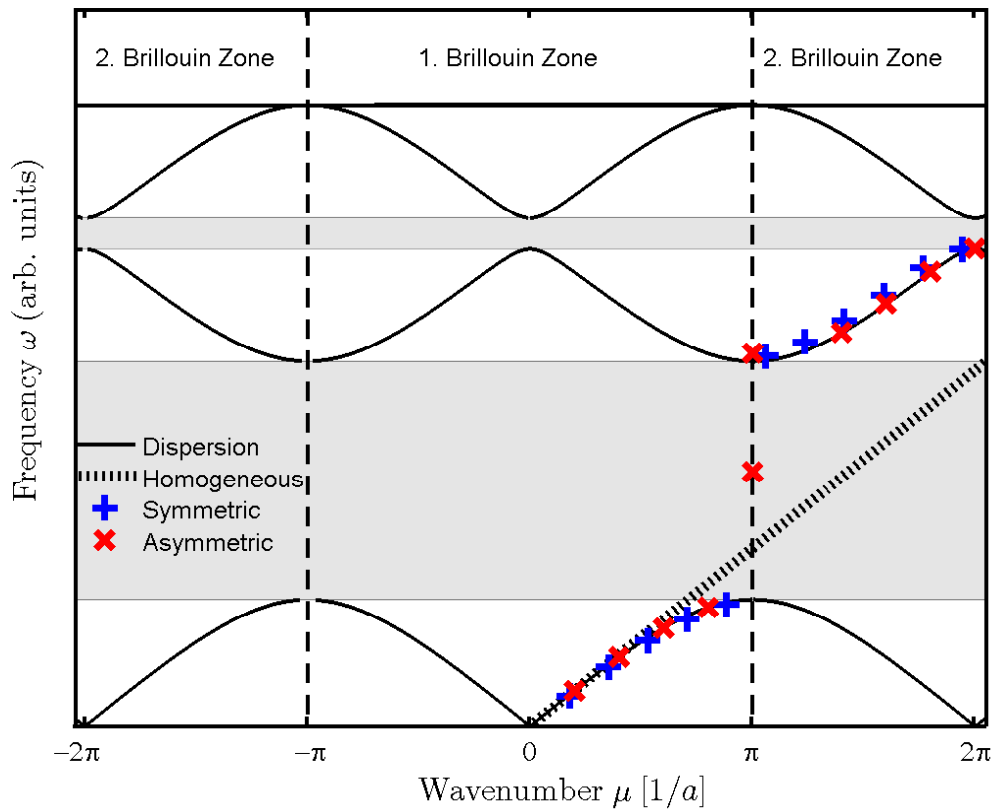


Figure 2.5: Band structures and natural frequencies.

The figure includes the first two Brillouin Zones to illustrate the periodicity of the frequency with wavenumber. The zones are symmetrical around zero, the higher zones being separated by the lower zones, as illustrated by the second zone being on either side of the first. The symmetry of the first zone is commonly utilized by only considering what is called the *Irreducible Brillouin Zone* (IBZ) when determining the band structure, which for the present example is the wavenumber range $\mu \in [0, \pi/a]$, where a is the unit cell length - the period of the system.

In addition to illustrate the symmetric and periodic nature of the band structure, Figure 2.5 draws attention to the physical interpretation of the higher branches of a band structure in the Irreducible Brillouin Zone. Even though the band structure is fully described by considering the IBZ, one should keep in mind that the representation is a condensed version of the full story. This is illustrated by the fact that the actual dominant wavenumbers of the standing waves of the finite structures increase with frequency, thus *not* falling within the IBZ, but rather an integer multiple thereof, as also mentioned in Hussein, Hulbert & Scott (2006). An interesting and relevant consequence of this becomes evident when considering the group velocity of the wave, which governs the propagation of energy in the system. The group velocity is given as the slope of the dispersion curve, i.e.,

$$c_g = \frac{\partial \omega}{\partial \mu}, \quad (2.4)$$

whereby a wrong assumption of which part of the dispersion branch the wave actually occupies could lead to erroneous conclusions about the direction of the energy transport in the system.

Finally, Figure 2.5 also shows how the periodic material exhibits band gaps (shaded areas) compared to the equivalent homogeneous material. Within these gaps waves will decay exponentially with distance rather than propagate freely, making the periodic material a candidate for a mechanical filter. Mathematically speaking, only wave-solutions with purely imaginary wavenumbers exist within the gap range, whereby a wave with amplitude A , frequency ω and wavenumber, $\mu = i\beta$ yields:

$$u(x, t) = Ae^{i(\mu x - \omega t)} = e^{-\beta x} Ae^{-i\omega t}, \quad (2.5)$$

from which it is clear that the magnitude of the imaginary part of the wavenumber, β , sometimes also termed the *attenuation constant*, is directly related to the strength of the attenuation of the wave. Hence, maximizing β is of great interest for optimizing the damping characteristics of a material.

Considering the natural frequencies of the two finite systems, the asymmetric system is seen to have a natural frequency approximately at the center frequency of the first gap, drastically reducing its efficacy as a filter at this frequency. The natural frequency corresponds to a *localized mode* of the system, meaning that it is localized at the “soft” end (material 2 is softer and lighter than material 1). The localized mode decays exponentially along the length of the rod, however for specific loading parameters it is still a resonant frequency, and relying strictly on the material description could prove fatal. The issue can be solved quite easily, as illustrated by the natural frequencies of the symmetric structure in Figure 2.4a, all outside of the stop bands. Guidelines for avoiding localized modes in this particular type of systems are given in Hladky-Hennion, Allan & De Billy (2005), but for the present purpose the point of not relying strictly on the infinite material analysis has been made.

2.1.3 Band gap mechanisms

Band gap design is a central theme of this thesis, being a part of [P1] and the main emphasis of [P2]. To intelligently design band gaps, a basic understanding of the mechanism

behind it is needed, hence the most common physical phenomena used for generating band gaps are presented. The first phenomena, known as *Bragg scattering* is the one utilized in the bi-material example from the previous section, and in [P1]. The impedance mismatch in the material causes propagating waves to be reflected, and the band gaps are frequency ranges where the reflected waves interfere destructively with the propagating waves, effectively prohibiting wave propagation. This effect occurs for any kind of periodicity for wavelengths that are comparable to the periodicity. The gap width increases with impedance mismatch, which allows for band-gap tunability by modifying the period and impedance mismatch of the system. The dependence on periodicity however, makes Bragg scattering inconvenient for some applications where wave attenuation is desired at lower frequencies, thus requiring impractically large unit cells.

The second phenomena is known as *local resonance*, where periodically distributed resonators interact with the propagating waves, opening up a band gap around their resonance frequency. This phenomena is basically a periodic application of the vibration absorber originally patented by Frahm, (Frahm 1911), which has been studied extensively from the point of view of structural dynamics since then. The resonator was not originally intended for periodic distribution, however since its re-introduction by Liu, Zhang, Mao, Zhu, Yang, Chan & Sheng (2000), it has been the topic of extensive research within periodic materials and structures, due to its ability to open up band gaps at frequencies governed by resonator parameters in ranges much lower than given by the unit-cell geometry.

For practical applications though, the local resonance phenomenon often requires significant mass increases for a relevant gap to open up. From a structural dynamics perspective, we know that a vibration absorber tuned to a specific mode is most efficient when it is placed at a position of high modal amplitude, that is, put the device where the displacement is largest. With this in mind, the periodic distribution of the local resonators decreases the efficacy of the added mass to mitigate structural vibrations, however applications where a distributed effect is more advantageous, such as sound barriers, the periodic distribution can be beneficial. Furthermore, as shown in Raghavan & Phani (2013), the periodic distribution is beneficial for creating additional band gaps at higher frequencies.

Another phenomenon for creating band gaps, which has received less attention in literature is the concept of *inertial amplification*. This concept utilizes a two-terminal mechanism attached to the material or structure, that provides a force that is proportional to the relative acceleration between the two points, thus representing the inertial equivalent of springs and dashpots. The ideal mechanism, known as the *inertor* was first described by Smith (2002), and has since enjoyed a great deal of attention and controversy¹ in the context of vehicle suspension systems. The working principle for band gap generation is the existence of antiresonance frequencies, where the enhanced inertial forces between the attachment points cancel the elastic forces, thus eliminating the propagating waves. In [P2] we investigate how applying inertial amplification mechanisms to a continuous material affects the band structure, illustrating great promise for this particular phenomenon.

¹The 2007 Formula One “Spy Scandal” about the “J-Damper”, was in reality about the inertor, (Chen et al. 2009)

2.2 Nonlinear systems

The large emphasis on periodic systems in this thesis is coupled with a focus on nonlinear effects. In [P1] we consider a system with an often encountered nonlinear material characteristic, while nonlinear kinematic relations are the source of the nonlinearity described in Chapter 5. Nonlinear dynamical systems can behave *qualitatively* different from linear systems, even if the nonlinearity is “small” or “weak”. Hence, it is important to identify possible nonlinearities in a system, as the linear design might break down in the presence of nonlinearity. A very fundamental and consequential difference between linear and nonlinear dynamic systems is found in the *energy dependence* of nonlinear systems, whereby the system behaviour depend on the energy level. Linear systems, on the other hand are “energy-invariant”, hence fundamental properties, such as the resonance frequencies, do not depend on the energy level. Furthermore the principle of superposition applies as well as the concept of “frequency in - frequency out”, neither of which applies to nonlinear systems. This increased complexity can be either appealing or frightening depending on whether you are interested in design from an academic or practical perspective. As researchers we tend to like increased complexity as it provides new opportunities and increased design spaces. When doing practical engineering design it is of pivotal importance that all design scenarios are covered, whereby the possibility of a radical change in behaviour from a small change in, e.g., the loading level or frequency seems nightmarish. Nonetheless, knowledge about how to deal with, suppress or even utilize nonlinearity is needed as we push the limits of technology and design, since the best approach is to “know your enemy” when designing engineering structures.

2.2.1 Sources of nonlinearity

It is outside the scope of this work to describe all and every kind of nonlinearity. The focus here is to present some common nonlinearities in relation to structural/mechanical systems partially to convince the reader that nonlinearity do in fact exist.

The fact that engineering design in practice is mostly based on linear models, taking nonlinearity into account on occasion when it is found to be relevant or present, might lead to the conclusion that nonlinearity is a special case. In fact it is the other way around, *linearity is the special case*, although a very common special case as described in the introduction. Linearity arises from linearizing the mathematical model around appropriate equilibrium points to be able to describe the dynamics near these points. The general case however, is inherently nonlinear as will be demonstrated by a few examples. Figure 2.6 illustrates two common nonlinearities, nonlinear material behaviour in Figure 2.6a and nonlinear kinematics or geometric nonlinearity in Figure 2.6b.

The schematics of typical stress-strain relations in compression for concrete and foam/rubber-type materials in Figure 2.6a illustrate that the stress in these materials do not depend linearly on the strain, but also that certain ranges can be considered linear to a reasonable approximation. The arrows indicate direction of loading, i.e., the foam material has different loading/unloading history, hence the material is dissipative in addition to being nonlinear. The concrete curve stops due to fracture after exhibiting *negative* stiffness, however, concrete structures are often designed to stay within the linear range of the curve, at least in the

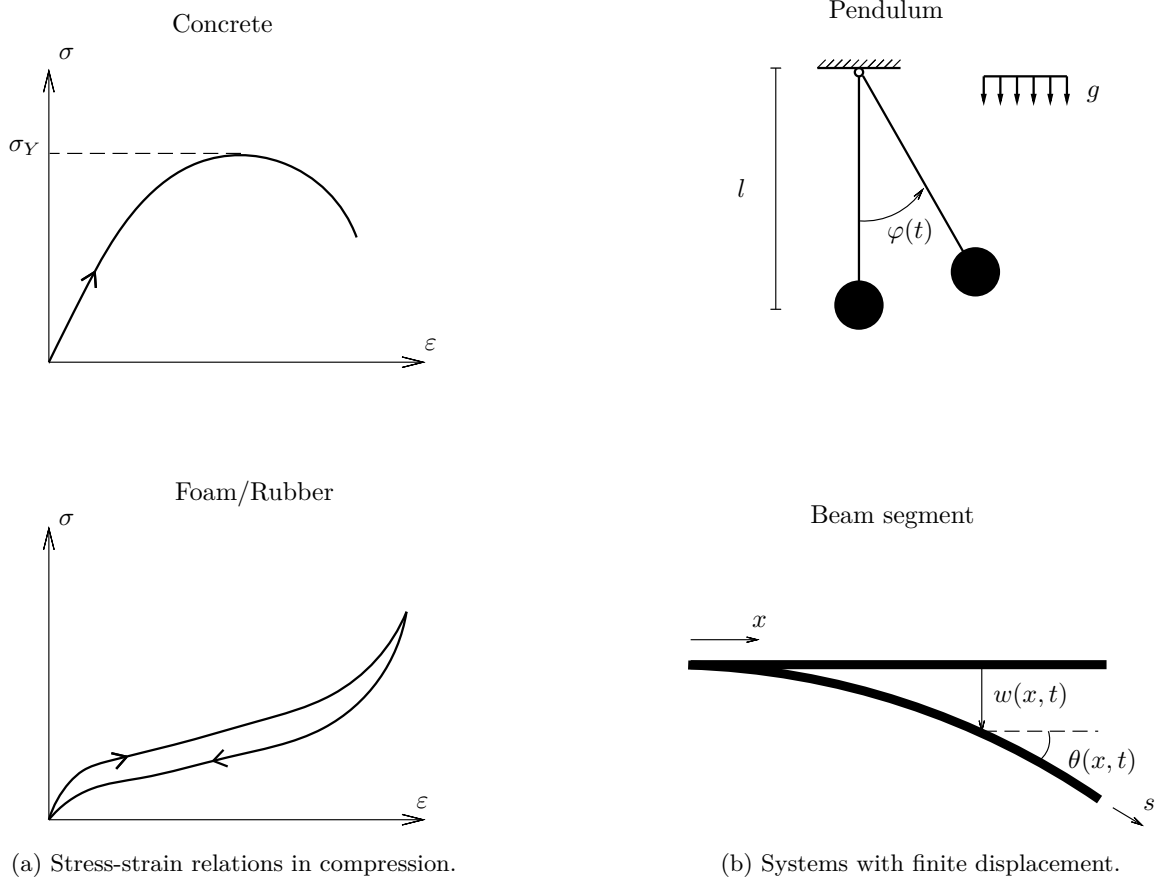


Figure 2.6: Schematical examples of nonlinearity.

serviceability limit state, describing the everyday conditions of, e.g., a concrete beam. In the ultimate limit state however, concrete beams are commonly allowed to develop a fully plastic stress distribution when calculating the carrying capacity, which in the context of Figure 2.6a would correspond to the stress at the peak of the concrete stress-strain curve, σ_Y . The schematics for a pendulum and an undeformed and deformed beam segment in Figure 2.6b illustrates two very common and “simple” systems with inherent nonlinear kinematics that are usually linearized. The governing equation for the pendulum in a gravity field contains a trigonometric function:

$$\ddot{\varphi} + \omega_0^2 \sin \varphi = 0, \quad \omega_0 = \sqrt{\frac{g}{l}}, \quad (2.6)$$

which for small rotations $|\varphi| \ll 1$ can be linearly approximated by $\ddot{\varphi} + \omega_0^2 \varphi = 0$. The cross-section inclination $\theta(x, t)$ of the beam segment is determined by $\sin \theta = \frac{dw}{ds}$, where s is the coordinate of the deformed beam axis. This means that the internal moment in the beam is given by:

$$M = EI\kappa = EI \frac{d\theta}{ds} = \frac{EI}{\cos\theta} \frac{d^2w}{ds^2} = \frac{EI \frac{d^2w}{ds^2}}{\sqrt{1 - \left(\frac{dw}{ds}\right)^2}}, \quad (2.7)$$

where EI is the bending stiffness of the cross-section and κ is the curvature. For small cross-section rotations, $|\theta| \ll 1$, Eq. 2.7 provides the classical expression, $M = EI \frac{d^2w}{dx^2}$. Hence, nonlinearity does not just occur for exotic cases with special structural elements or peculiar material properties, but is inherently present in nature and technology. The linear case arises as the special case which in many cases is very appropriate. However, as we push the limits of science and technology, optimizing materials and structures to be even more light-weight, slender and energy efficient, we also push the limits of the mathematical models and it is important that we remember to reassess whether the assumptions leading to linearization are still valid.

In addition to the two described types of nonlinearity, other physical sources include: Friction, damage and cracks, stop and play as well as state-dependent loads such as aero- and hydrodynamic dynamic loads. In short, nonlinearity is everywhere, whether you expect it or not. You might as well make the best of it.

2.2.2 Effects of nonlinearity

Including nonlinearity in the analysis introduces a vast amount of effects on the dynamics of the system. The effects depend on the type of nonlinearity, energy level and specific system design. The pendulum from Figure 2.6b will serve as an illustrative example, since it, in spite of its apparent simplicity, exhibits a range of interesting nonlinear phenomena.

Multiple equilibrium points

At an equilibrium point, the motion of the system is zero, i.e., the velocity and acceleration are zero. Equilibrium points are also termed singular points, fixed points or zeros. In linear systems, only a single equilibrium point exists - the rest state if you will. This corresponds to the pendulum hanging vertically with the mass down, $\varphi = 0$, or the beam being at rest $w(x, t) = 0$. Often this is the state that the model has been linearized around, whereby the linear model describes the dynamics in the vicinity of this equilibrium. Nonlinear systems often possess multiple equilibrium points, e.g., the pendulum in Figure 2.6b has the equilibrium points $\theta = j\pi$, $j = 0, \pm 1, \pm 2, \dots$. A single-mode approximation of a pre-stressed beam-column will reveal that the system has equilibrium points at zero deflection but also in the post-buckled state, if the pre-stress is large enough. The “upside down” equilibria of the pendulum will, in the absence of some stabilization effect, be unstable and the pendulum will not stay at this position. Hence, equilibria have the notion of *stability* associated with them, which determines whether or not the system will stay at the equilibrium for infinitesimal perturbations. In short, an *unstable* equilibrium will generally not be observed in the lab or real life (upside down pendulum for example), while the stable equilibria can be observed.

Nonlinear local dynamic analysis investigates the dynamics around these equilibrium points, (Thomsen 2003), often by Taylor-expanding the nonlinear term to a certain order.

This is similar to linear analysis in the sense that the nonlinearity is approximated by polynomials, however the degree of the polynomials is larger leading to a larger range of validity and an increase in complexity of the analysis.

Frequency/Energy dependence

The equation governing small-but-finite oscillations of the pendulum in Figure 2.6b is:

$$\ddot{\varphi} + \omega_0^2 \varphi - \gamma \varphi^3 = 0, \quad \gamma = \frac{\omega_0^2}{6} \quad (2.8)$$

as obtained by a Taylor expansion of the sine term, accurate for $|\varphi| \lesssim \pi/3$. Note that, even though the nonlinearity arises from a kinematic source, the nonlinear terms presents itself as a nonlinear stiffness term. The equation can be solved approximately using various methods that will not be described here, however the interested reader can consult Thomsen (2003) for a simple introduction to a wide range of approximate solution methods. The approximate solution is:

$$\varphi(t) \approx a_0 \cos(\tilde{\omega}t + \beta_0) - \frac{1}{192} a_0^3 \cos(3(\tilde{\omega}t + \beta_0)), \quad \tilde{\omega} = \left(1 - \frac{1}{16} a_0^2\right) \omega_0 \quad (2.9)$$

where the concept of multiple harmonic generation is evident from the second term. The vibration frequency, $\tilde{\omega}$, depends on the amplitude of vibration a_0 , whereby the energy (or amplitude) invariance of the natural frequency has been lost. This reduction in natural frequency with increasing vibration amplitude is commonly called a softening nonlinearity. This can be understood by recalling that the nonlinearity was a stiffness nonlinearity, with a negative sign, hence as the amplitude increases, the effective stiffness, and thus frequency, decreases. This simple interpretation of the nonlinearity is not always possible, however the label softening/hardening nonlinearity is commonly used when the natural frequency decreases/increases with amplitude. The present example of a softening nonlinearity for the pendulum can be observed by going to the local playground, sitting on a swing and noting that the optimal frequency of excitation decreases with swing amplitude.

Multiple stable solutions

This effect is closely related to the frequency/energy dependence. For the unloaded pendulum it is seen that the natural frequency changes with amplitude, such that the initial conditions (a_0, β_0) changes the frequency of the response and not just the amplitude level and phase. When adding loading to the mix, the resulting vibration amplitude depends on the transient as illustrated by the frequency/amplitude curve in Figure 2.7, obtained from adding harmonic forcing at frequency Ω to Eq. (2.8).

The *backbone curve* is obtained from the undamped, unloaded case, i.e., it is the frequency/amplitude relation from Eq. (2.9). A “linear backbone curve” would be a vertical line at $\Omega/\omega_0 = 1$, which the frequency response would peak at, and be symmetrical around. The nonlinear frequency response in Figure 2.7 is bend to the left which, means that for certain frequency ranges, several solutions are present for the same frequency, which does not occur

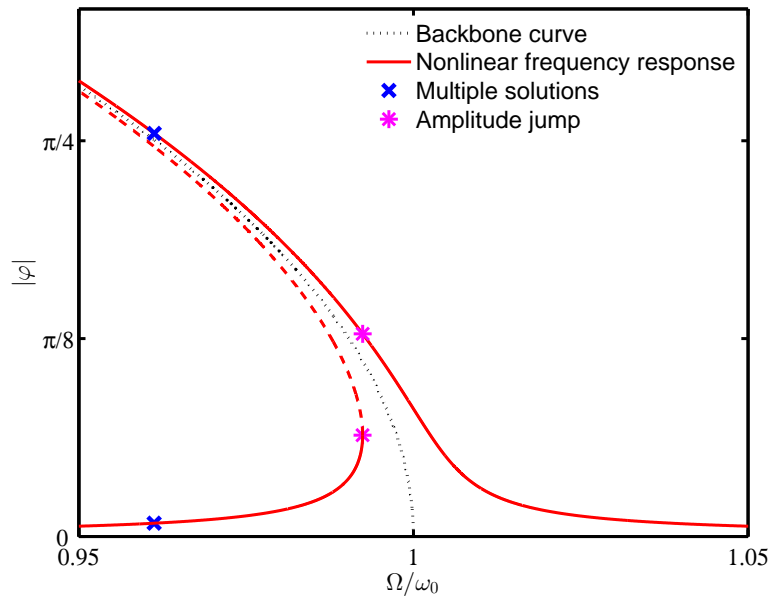


Figure 2.7: Nonlinear frequency amplitude curve.

for the linear counterpart. The dashed part of the frequency response curve indicates unstable solutions, i.e., solutions that will generally not be observed. The blue crosses illustrate a frequency where the amplitude can either be very small or approximately $\pi/4$ depending on the transient of the response. Similarly the magenta asterisks illustrate a point where a slight increase in frequency (coming from below) would cause a jump in the amplitude level due to the loss of stability of the solution branch. A direct consequence of this frequency/energy dependence is that the frequency responses obtained for structures exhibiting some form of nonlinearity will be energy-dependent, which complicates system identification significantly. Furthermore, the fact that the resonance frequencies of the structure change with loading amplitude can be rather inconvenient for designers, since it might not be sufficient to ensure that loading frequencies are away from linear resonance frequencies. It does however introduce an additional design parameter, whereby the softening/hardening behaviour can be tailored as considered for plane frame structures in Dou & Jensen (2016).

Higher harmonics and internal resonance

As seen in the approximate solution to the nonlinear pendulum equation in Eq. (2.9), additional harmonics are generated by nonlinearity. The amount of higher harmonic generation, both in terms of the amplitude and number of additional harmonics depend on the strength of the nonlinearity. One phenomenon related to higher harmonic generation is called *internal resonance*, which is the case where the higher harmonic excites a natural frequency of the system. This obviously requires at least two modes of the system, such that there are in fact two resonance frequencies to have an integer ratio leading to internal resonance. The nonlinear modal interaction occurring at internal resonance means that a large amount of energy is being transferred between modes. If a higher mode has been dismissed for dy-

dynamic analysis due to the loading frequencies being much smaller than its natural frequency, and this mode is suddenly activated by internal resonance, the result could be catastrophic breakdown. A great and illustrative, real-life example of a structure exhibiting internal resonance is the SmallSat spacecraft structure considered in Noël, Renson & Kerschen (2014), where 2:1 internal resonance between the 3rd and 7th nonlinear normal mode is experimentally demonstrated.

The large energy transfer at internal resonance could lead to problems for the structure, but another approach is to utilize the internal resonance to intentionally transfer the maximal amount of energy from the target mode to a higher mode. This could be utilized for high-frequency energy dissipation, which in real time could reduce vibration amplitude faster than at the lower frequency. The investigation in [P1] examines the potential of maximizing higher harmonic generation in a nonlinear, periodic material.

Is that all?

The short and exact answer is no. Additional effects include bifurcations - points in the parameter/design space where a small change in a parameter (the bifurcation parameter) will cause a dramatic, qualitative change in the response. In fact the amplitude jump points in Figure 2.7 are bifurcation points, where a small frequency change leads to a dramatic and discontinuous change in vibration amplitude. Another effect is chaotic motion - unpredictable, deterministic motion without any discernible stochastic components - which can arise, e.g., as a consequence of a sequence of bifurcations.

The above presented effects of nonlinearity do not begin to cover the vastness of the subject, but will suffice for the purpose of this thesis.

Chapter 3

Nonlinear periodic materials

Periodic materials and nonlinear dynamics as presented in Chapter 2 are combined in the present chapter, where the investigations contained in [P1] will be presented. The chapter will briefly describe the mathematical solution approach, leaving most of the technical details in the paper. The thorough investigation in the paper has been condensed to the most relevant and interesting results and conclusions, whereby additional background data can be obtained by consulting the paper.

The presence of nonlinearity shifts the natural frequency with amplitude, which also means that the propagation frequency of waves will shift with wave amplitude. Hence, the band structure of a material becomes amplitude dependent, altering the dispersion branches in various ways, depending on the nonlinearity. Changing the band structure means that the band gap phenomenon is affected by nonlinearity, providing additional tuning parameters for the gaps on top of the linear impedance control. If the nonlinear parameters and/or wave amplitude can be controlled, the band gaps might be specifically tuned for certain wave amplitudes and/or directions, see e.g. Daraio, Nesterenko, Herbold & Jin (2006) and Narisetti, Ruzzene & Leamy (2011).

In addition to band gap tunability, modal interaction and higher harmonic generation are interesting phenomena to investigate in relation to wave-control. Both phenomena are somewhat related to transporting energy between modes and frequencies, whereby vibrations in a target mode might be minimized by transferring the wave-energy to another mode. This mode might be beneficial to trap or dissipate the energy in terms of applied dampers of inherent attenuation.

3.1 A simple material model

In [P1] we present a simple one-dimensional model of a nonlinear phononic material - a periodic material with nonlinear characteristics. The model, illustrated in Figure 3.1, consists of masses and springs, thus it represents a simple discretization of a one-dimensional structural element, such as a rod (as the example from Chapter 2), cable or beam. In fact, a homogeneous version of the system in Figure 3.1 has been experimentally realized by steel beads on a wire with finite displacements by Manktelow, Leamy & Ruzzene (2014*a*).

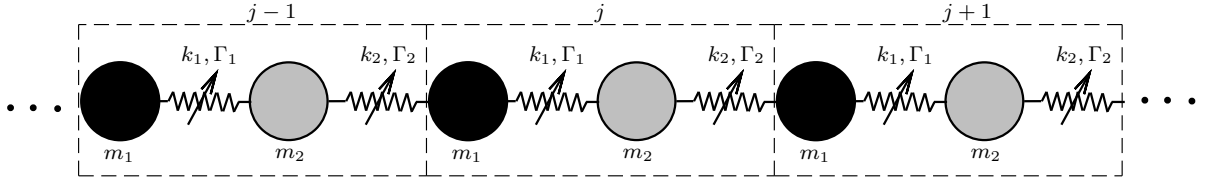


Figure 3.1: Infinite, nonlinear, inhomogeneous mass-spring chain.

The dots at both ends indicate that the unit cell repeats itself infinitely - we are considering material dynamics. The unit cell has the mass parameters m_1 and m_2 and the stiffness parameters k_1, Γ_1 and k_2, Γ_2 where Γ_i represents nonlinear stiffness of cubic order.

3.1.1 Nonlinear dispersion shifts

The periodicity of the system inspires us to consider the governing equations of motion for a single unit cell:

$$\mathbf{M}\ddot{\mathbf{u}}_j + \mathbf{K}\mathbf{u}_j + \mathbf{f}_j^L(u_{j-1,2}, u_{j+1,1}) + \mathbf{f}_j^{NL}(\mathbf{u}_j, u_{j-1,2}, u_{j+1,1}) = \mathbf{0}, \quad \mathbf{u}_j = \begin{bmatrix} u_{j,1}(t) \\ u_{j,2}(t) \end{bmatrix}, \quad (3.1)$$

where $u_{j,n}(t)$ is the displacement of mass n in unit cell j . The linear and nonlinear force vectors \mathbf{f}_j^L and \mathbf{f}_j^{NL} depend on the motion of the neighbouring cells. As described in Chapter 2 on periodic systems, the Floquet-Bloch theorem can be used to relate the motion (solution) at neighbouring cells to the considered unit cell. The theorem however, was originally developed for linear systems, hence applying it directly to nonlinear systems might prove problematic. This is overcome in [P1] by using an asymptotic approach, the method of multiple (time) scales, to solve the governing equations for unit cell j . Only the main idea behind the solution approach is presented here, specific details can be found in [P1], while general information on the method of multiple scales can be found in, e.g., Nayfeh (1981) and Thomsen (2003).

The approach is based on an assumption of the nonlinear elastic forces only perturbing the linear part of the system slightly. Introducing the perturbation parameter ε as:

$$\mathbf{f}_j^{NL}(\mathbf{u}_j, u_{j-1,2}, u_{j+1,1}) = \varepsilon \tilde{\mathbf{f}}_j^{NL}(\mathbf{u}_j, u_{j-1,2}, u_{j+1,1}), \quad (3.2)$$

indicates the smallness of the nonlinear forces in terms of $\varepsilon \ll 1$, such that $|\mathbf{f}_j^{NL}| = O(\varepsilon)$. Next, we introduce a two new time scales, T_i , and make an asymptotic expansion of the solution $\mathbf{u}_j(t)$:

$$\mathbf{u}_j(t) = \mathbf{u}_j^{(0)}(T_0, T_1) + \varepsilon \tilde{\mathbf{u}}_j^{(1)}(T_0, T_1) + O(\varepsilon^2), \quad \left| \mathbf{u}_j^{(1)} \right| = \left| \varepsilon \tilde{\mathbf{u}}_j^{(1)} \right| \ll \left| \mathbf{u}_j^{(0)} \right|, \quad T_i = \varepsilon^i t, \quad (3.3)$$

i.e., the nonlinear correction term $\mathbf{u}_j^{(1)}$ perturbs the linear part, $\mathbf{u}_j^{(0)}$. The new, independent time-scales T_0 and T_1 represent the motion at the fast (regular) time scale, T_0 , and a slower time scale, T_1 , capturing the amplitude and phase modulations from nonlinearity. The variable

shift contained in Eqs. (3.3) transforms the nonlinear equations of motion in Eq. (3.1) into a cascading set of linear equations of increasing approximation order, ε^i . Each set of equations has the same homogeneous part, and the equations at higher approximation orders have loading terms containing the solutions of the lower order equations whereby the sets of equations are to be solved successively.

Considering wave-propagation in the infinite medium in Figure 3.1, the order ε^0 equations provide the linear dispersion relation, while the order ε^1 equations provide the nonlinear frequency corrections and higher harmonic generation. The linearity of the equations at each scale allows for the use of the Floquet-Bloch theorem by which the normalized, linear dispersion relation is obtained as:

$$\bar{\omega}_k = \sqrt{\frac{1}{2} \left(1 + \beta \pm \sqrt{(1 - \beta)^2 + 4(c_1^4 + c_2^4 + 2c_1^2 c_2^2 \cos \mu)} \right)}, \quad \bar{\omega}_k = \frac{\omega_k}{\omega_n}, \quad (3.4)$$

where the minus-sign corresponds to the lower branch, commonly referred to as the acoustical branch, and the plus-sign corresponds to the upper, optical branch. The dispersion relation is expressed in terms of a characteristic frequency, ω_n , the mass ratio, β and the normalized stiffness, c_i , defined by:

$$\omega_n = \sqrt{\frac{k_1 + k_2}{m_1}}, \quad \beta = \frac{m_1}{m_2}, \quad c_i = \sqrt{\frac{k_i}{\omega_n^2 \sqrt{m_1 m_2}}}. \quad (3.5)$$

The dispersion relation expresses the linear propagation frequency ω_k as a function of the wavenumber μ . Figure 3.2 illustrates the normalized, linear dispersion relation within two full periods of the normalized wavenumber $\bar{\mu} = \mu/\pi$, with the Irreducible Brillouin Zone (IBZ) marked by the magenta dash-dot rectangle. As mentioned in Chapter 2, this is the range of wavenumbers commonly considered when calculating the band structure of a periodic material.

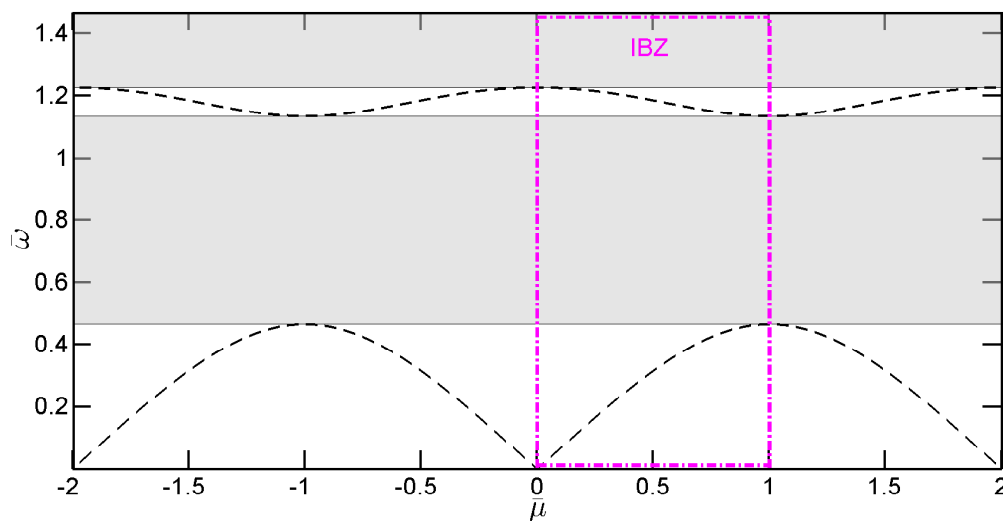


Figure 3.2: Linear dispersion relation. $m_1 = 1$, $m_2 = 2$, $k_1 = 1$, $k_2 = 5$.

The two dispersion branches represent the two wave-modes of the system, and the linear,

homogeneous solution, $\mathbf{u}_j^{(0)}$, is a sum of these travelling wave-modes:

$$\mathbf{u}_j^{(0)}(T_0, T_1) = a_1(T_1)\mathbf{v}_1 e^{i(\mu j + \omega_1 T_0)} + a_2(T_1)\mathbf{v}_2 e^{i(\mu j + \omega_2 T_0)} + c.c. \quad (3.6)$$

where \mathbf{v}_k is the (complex-valued) eigenvector of mode k and *c.c.* denotes complex conjugate. The slow-time variation is contained in the complex, modal amplitude function $a_k(T_1)$, which is determined at the order ε^1 -approximation. It is determined by requiring *non-secular* behaviour of the order ε^1 -equations. This means that the solution to the equations cannot grow unbounded in time, since this would violate the uniformity of the asymptotic expansion, $|\varepsilon \tilde{\mathbf{u}}_j^{(1)}(T_0, T_1)| \ll |\mathbf{u}_j^{(0)}(T_0, T_1)|$. Put in simpler terms, since the homogeneous parts of the order ε^0 and ε^1 equations are the same, loading terms proportional to the eigenvalues of the order ε^0 solution will excite an eigenmode of the order ε^1 equations. This will cause the solution to grow unbounded in time which cannot be allowed, for obvious physical and mathematical reasons.

This constraint is used to formulate the *solvability condition*, a set of differential equations in slow time, T_1 , that determines the unknown amplitude function $a_k(T_1)$ such that the uniformity of expansion is kept. The complex amplitude functions are expressed on polar form $a_k(T_1) = \frac{\alpha_k}{2} e^{i\varphi_k}$ where both $\alpha_k = \alpha_k(T_1)$ and $\varphi_k = \varphi_k(T_1)$ are real-valued functions. For the two-mass unit cell, disregarding certain singular points in the wavenumber/frequency spectrum, the solvability condition is the four differential equations:

$$\omega_1 \alpha_1' = 0, \quad (3.7a)$$

$$\omega_1 \alpha_1 \varphi_1' = \frac{3}{8} \eta_1 \alpha_1^3 + \frac{3}{4} \xi_{12} \alpha_1 \alpha_2^2, \quad (3.7b)$$

$$\omega_2 \alpha_2' = 0, \quad (3.7c)$$

$$\omega_2 \alpha_2 \varphi_2' = \frac{3}{8} \eta_2 \alpha_2^3 + \frac{3}{4} \xi_{21} \alpha_2 \alpha_1^2, \quad (3.7d)$$

where prime denotes differentiation with respect to T_1 while η_k and ξ_{ki} are real valued constants related to the nonlinear coefficients (and other system parameters). The singular points that are disregarded are related to the higher harmonic exciting an eigenmode of the system, and are often termed *internal resonance*, as mentioned in Section 2.2.2. These points will be discussed further in Section 3.1.2.

The solvability condition reveals that the amplitudes $\alpha_k = \alpha_{k0}$ are constant in slow time, while the phases φ_k are linear. Furthermore, the phases are affected by the presence of both modes, which translates into the propagation frequency being affected by the presence of both modes. Obtaining the amplitude and phase modulations from the solvability condition provides the full, order ε^0 -solution:

$$\mathbf{u}_j^{(0)}(T_0, T_1) = \frac{\alpha_{10}}{2} \mathbf{v}_1 e^{i(\mu j + \tilde{\omega}_1 T_0 + \varphi_{10})} + \frac{\alpha_{20}}{2} \mathbf{v}_2 e^{i(\mu j + \tilde{\omega}_2 T_0 + \varphi_{20})} + c.c., \quad (3.8)$$

where the corrected propagation frequencies are determined by:

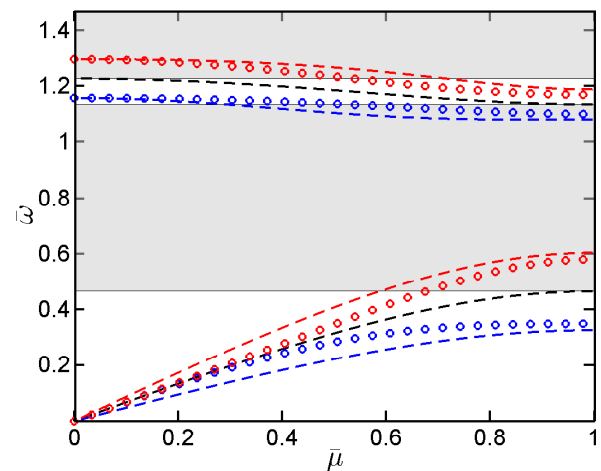
$$\tilde{\omega}_k = \omega_k + \varepsilon \left(\frac{3}{8} \frac{\eta_k}{\omega_k} \alpha_{10}^2 + \frac{3}{4} \frac{\xi_{ki}}{\omega_k} \alpha_{20}^2 \right) = \omega_k + \varepsilon (\Delta\omega_k + \Delta\omega_{ki}), \quad k, i = 1, 2. \quad (3.9)$$

The constants of integration, α_{k0} and φ_{k0} , are determined by the initial conditions. Figure 3.3 illustrates the effect of modal interaction for the same example chain as in Figure 3.2, with the nonlinear stiffness parameters and wave amplitudes given in Table 3.1. The dashed lines represent the case including modal interaction, while the circles represent the nonlinear dispersion relation with no modal interaction.

Figure 3.3: Nonlinear Dispersion. Dashed lines: Including modal interaction. Circles: Excluding modal interaction. Red: $\Gamma_1 = \Gamma_2 = 0.05$. Blue: $\Gamma_1 = \Gamma_2 = -0.05$.

Table 3.1: Nonlinear parameters.

Γ_1	Γ_2	α_{10}	α_{20}
± 0.05	± 0.05	2	2



For the chosen parameters, the presence of both waves is seen to alter the band structure, predominantly near the middle of the Irreducible Brillouin Zone. The increased dispersion correction quantifies the effect of the increased energy level in the chain, due to the presence of multiple modes rather than just one. The present example is meant to illustrate the effect of modal interaction, while the effect of inhomogeneous nonlinear stiffness is left unexplored. It is noted that this is an additional possibility of designing the material, provided that the nonlinear coefficients can be controlled. It has not been the focus of [P1] however, and thus, not a focus of the present thesis.

3.1.2 Generation of higher harmonics

The full approximate solution contains the linear part, $\mathbf{u}_j^{(0)}$, and the nonlinear correction, $\mathbf{u}_j^{(1)}$. The latter part contains the higher harmonic generation, which is a primary focus of the investigation in [P1]. Solving the order ε^1 -equations provides the nonlinear correction, whereby the full approximate solution for an acoustic wave travelling through the chain is:

$$\mathbf{u}_j \approx \frac{\alpha_{10}}{2} \mathbf{v}_1 e^{i(\mu j + \tilde{\omega}_1 t)} + \gamma \frac{\alpha_{10}^3}{8} \mathbf{y} e^{i(3(\mu j + \tilde{\omega}_1 t))} + c.c. \quad (3.10)$$

where the original time variable, t , has been reintroduced. The coefficient γ depends on virtually all the system parameters. Considering the band structure of the system in Figure 3.3 the higher harmonic frequency can fall into either pass- or stop-bands, as well as fall almost directly on a linear dispersion curve in the long-wave limit $\bar{\mu} \rightarrow 0$.

In [P1] we quantify the higher harmonic generation by $|A_3/A_1| = |\mathbf{u}_j^{(1)}|/|\mathbf{u}_j^{(0)}|$ and investigate four distinct points on the acoustic dispersion branch for higher harmonic generation. The four points are investigated for the same linearized, kinetic input energy $E_0 = \frac{1}{2}\tilde{m}_1(\alpha_{10}\omega_1)^2$ where \tilde{m}_1 is the modal mass of the first mode, to produce comparable results over multiple frequencies. The general result is that larger nonlinearity (in terms of the nonlinear stiffness coefficient) produces a larger level of higher harmonic generation. Furthermore, when the higher harmonic falls within a stop band, a comparably lower level of higher harmonic generation is observed. These two observations were somewhat expected, hence, the focus will be on some of the more interesting results. These are obtained for larger input energy, $E_0 = 1$, in the long-wave limit and for the case where the higher harmonic falls within the second pass band, more specifically for the normalized wavenumbers $\bar{\mu} = 0.1$ and $\bar{\mu} = 0.66$.

Figure 3.4 illustrates the higher harmonic generation as function of the nonlinear stiffness ratio Γ_1/Γ_2 for four base levels of $\Gamma_2 = 0.001, 0.005, 0.01$ and 0.05 .

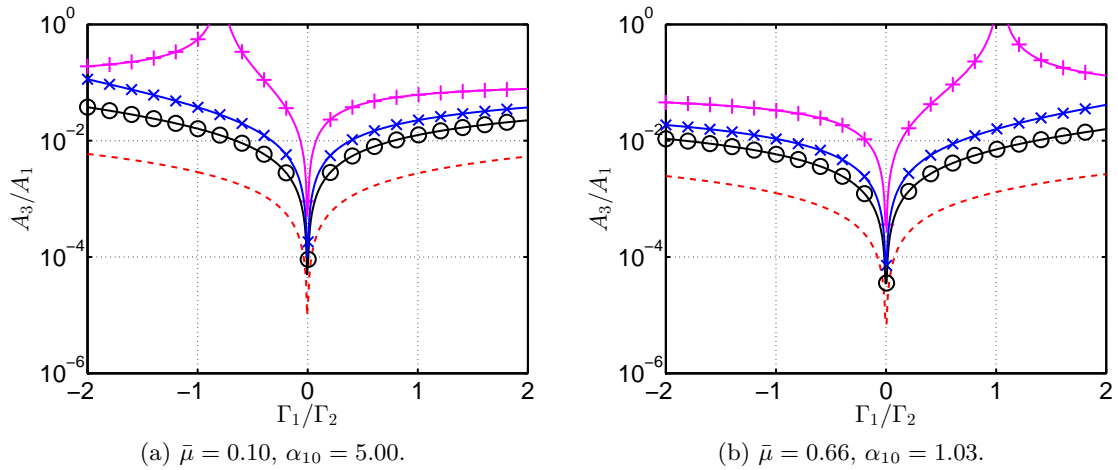


Figure 3.4: Higher harmonic generation, $E_0 = 1$. Red dashed: $\Gamma_2 = 0.001$. Black circled: $\Gamma_2 = 0.005$. Blue crossed: $\Gamma_2 = 0.01$. Magenta plus-signs: $\Gamma_2 = 0.05$.

The resonance-like behaviour for the largest nonlinearity is what immediately catches the eye. This behaviour represents points of deficiency of the mathematical solution, since the perturbation assumption is clearly violated as $|A_3/A_1|$ approaches 1 (and beyond). This deficiency has its origin in an assumption made for the solvability condition, which is that the higher harmonic terms do not excite an eigenmode of the system. Figure 3.5 shows the dispersion relations for the two identified critical parameter combinations, with the fundamental and higher harmonic indicated by a blue cross and plus-sign respectively.

The linear propagation frequency at $3\bar{\mu}$ is indicated by a blue circle, illustrating that the higher harmonic falls exactly on the linear dispersion curve, thus violating the assumption. If a mathematically robust solution model is desired, these critical points must be considered

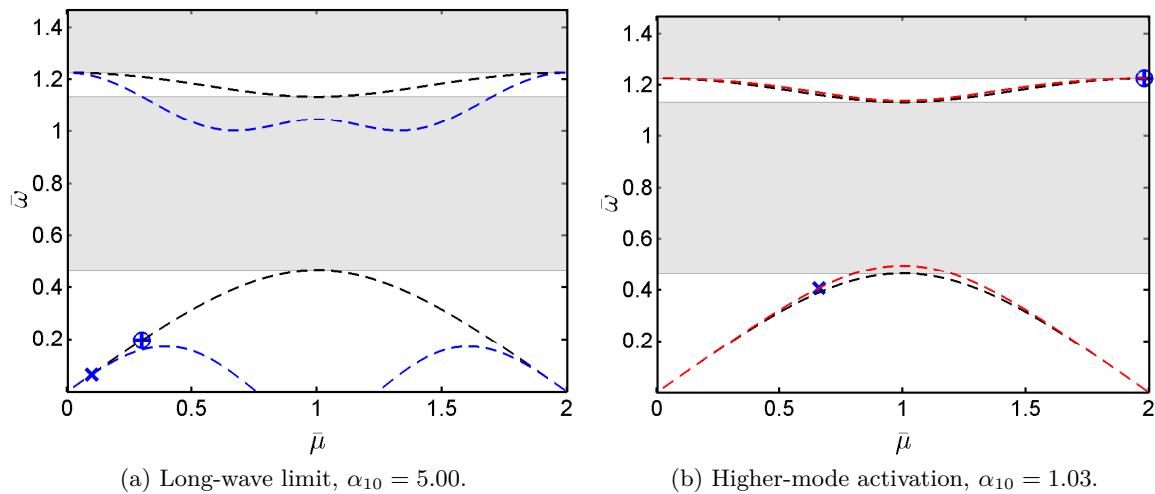


Figure 3.5: Band structures at critical parameter combinations. Black dashed line: Linear dispersion. Blue dashed line: Nonlinear, softening dispersion. Red dashed: Nonlinear hardening dispersion. Blue cross: Fundamental harmonic. Blue plus-sign: Higher harmonic. Blue circle: Linear propagation frequency at $3\bar{\mu}$.

individually when formulating the solvability condition, similar to what is done for a single-mass model in Manktelow et al. (2011). They consider interaction between two separate and co-existing waves rather than modal (self-)interaction as investigated here. The results of the reference however, indicates only modest effects on the dispersion as well as small amplitude modulations in the presence of internal resonance. Hence, the specific consideration of the mathematical internal resonance point does not seem to present a great potential for energy transfer between waves for the homogeneous chain in the reference. It turns out that the implications of this lack of robustness are not too severe, since the general accuracy of the analytical model deteriorates before internal resonance issues arise which, in the absence of a physical experiment, will be demonstrated by numerical simulations.

The numerical simulations are carried out by loading a finite chain, consisting of $N_{cell} = 878$ unit cells, at its right end by a harmonic force. The response is then processed by both spatial and temporal Fourier transforms to obtain the wavenumber and frequency content of the response. To kill any transients in the response, the first part of the chain, corresponding to five wavelengths, $5\lambda(\Omega)$, of a linear acoustic wave propagating at the loading frequency, Ω , is lightly damped. The damping is then exponentially decreased over the distance of five additional wavelengths. The harmonic loading is ramped up from zero to avoid the formation of shocks in the chain. The numerical model for simulation is illustrated in Figure 3.6, while the expressions for the load and exponentially decreasing damping is seen in Eq. (3.11). Additional details can be found in [P1].

$$F(t) = F_0 \left(1 - e^{-\zeta_F t}\right) \sin \Omega t, \quad c(n) = c_0 \left(1 - e^{-\zeta_c n}\right). \quad (3.11)$$

The spatial transform is carried out on a limited domain of the chain, where the wave is considered to have reached steady state, while the temporal transform is carried out for the

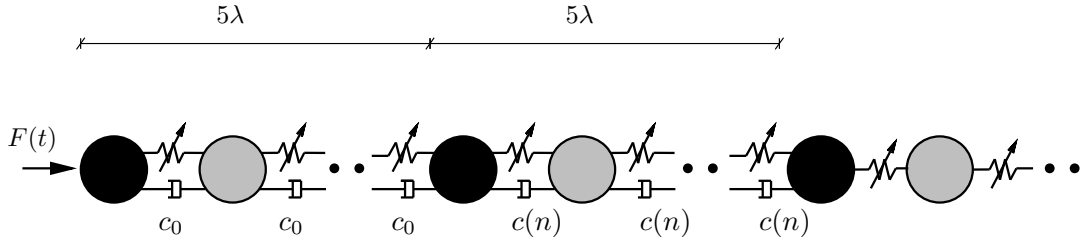


Figure 3.6: Finite, damped chain for numerical simulations.

second half of the simulation time for a mass in the middle of the considered spatial domain. The simulation time is chosen as the travel time from one end of the chain to the other for a linear wave propagating at the loading frequency to avoid reflections from the boundary in the signals. Having obtained the fundamental wavenumber and amplitude from the numerical simulations, these are provided to the analytical model to compare the analytical predictions to numerical results. Figure 3.7 compares the higher harmonic generation predicted by the analytical model (red plus-signs) to the numerical simulations (blue crosses) in a log-log scale as functions of the linearized input energy E_0 . The model and simulation parameters are summarized in Table 3.2

Table 3.2: Model parameters for numerical simulations.

N_{cell}	m_1	m_2	k_1	k_2	Γ_1	Γ_2	c_0	ζ_c	ζ_F
878	1	2	1	5	0.05	0.05	0.06	$-\frac{\ln(0.01)}{5\lambda}$	$-\frac{\ln(0.1)}{8\frac{2\pi}{\Omega}}$

The black, dashed curves approximate the continuous development of the higher harmonic generation when the wavenumber provided to the analytical model is obtained from the linear dispersion branch at the frequency of the harmonic load.

The higher harmonic generation is illustrated for four distinct points on the dispersion curve, representing different regimes of the higher harmonic. The analytical model appears to produce reliable results for low energies for the first three wavenumbers, as expected by the asymptotic approach, however the numerical results are seen to be consistently below the analytical for $\bar{\mu} = 0.66$. Furthermore, it appears that the $\bar{\mu} = 0.10$ predictions are more inaccurate than the $\bar{\mu} = 0.20$ predictions, for comparable energy levels. In spite of the increased inaccuracy in the long-wave limit, the trend predicted from the analytical model is still evident, increasing the higher harmonic generation with input energy, and the largest energy transfer obtained in the long-wave limit, $\bar{\mu} = 0.10$.

Considering Figure 3.7d, the analytical, continuous prediction is noted to curve upwards as we approach the $E_0 = 1$, which is exactly the case of mathematical deficiency of the analytical model seen in Figures 3.4b and 3.5b. To illustrate that this is primarily a point of academic interest in terms of the results from the analytical model, Figure 3.8 shows the frequency spectra for the final point in Figure 3.7d and a point with even higher forcing applied.

The frequency spectrum for $F_0 = 2$ (corresponding to the final point in Figure 3.7d) illustrates that the energy is distributed over several distinct frequencies, which could con-

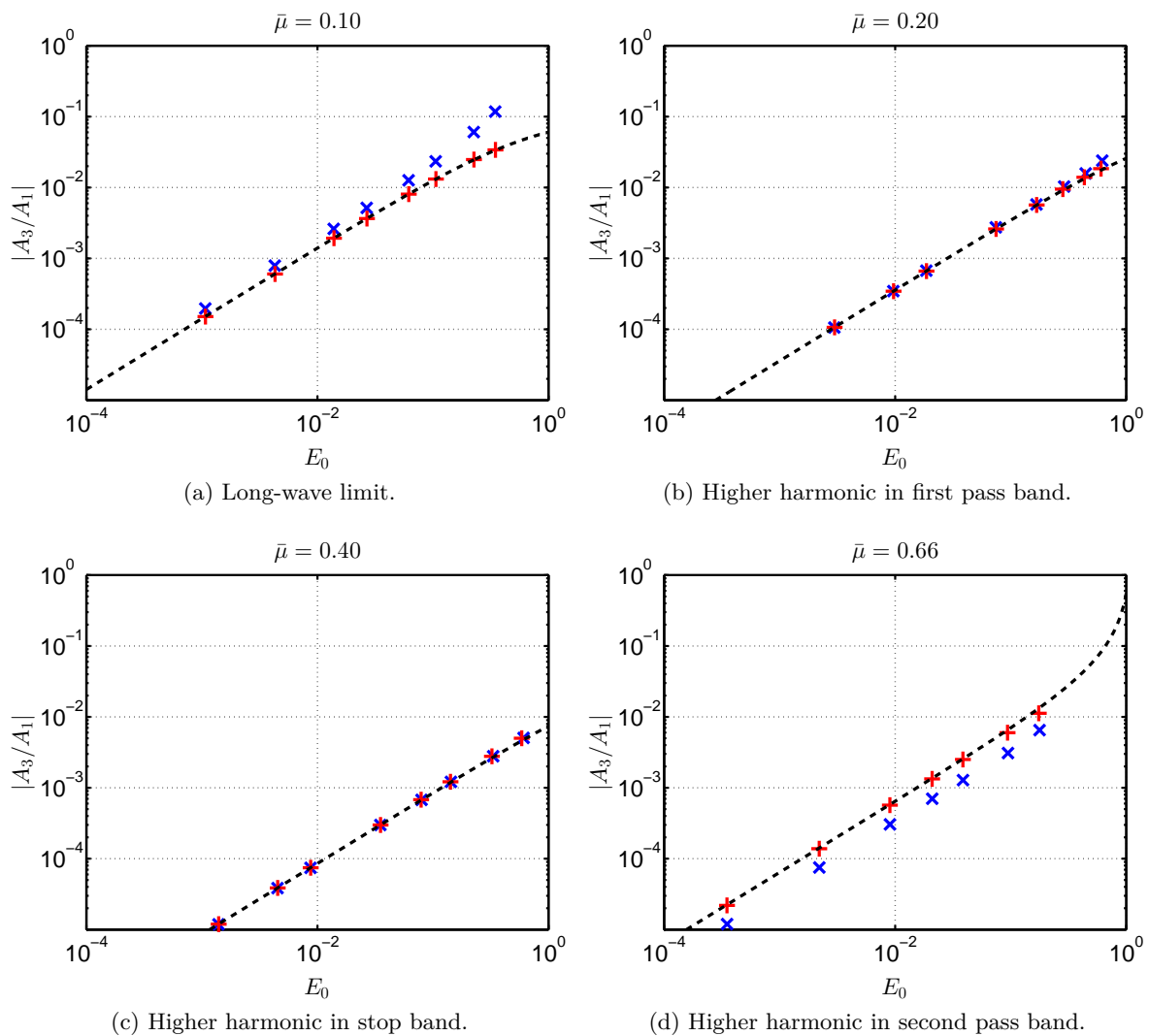


Figure 3.7: Higher harmonic generation. Red plus-signs: Analytical predictions. Blue crosses: Numerical simulations. Dashed black line: Approximate, analytical development.

tribute to the lack of accuracy compared to the analytical prediction which assumes only two frequency components. Furthermore, the continuous-looking frequency spectrum for $F_0 = 3$ reveals that for this wave-amplitude (and above), the energy is no longer contained to specific frequency components but is distributed over ranges of frequencies. The ranges are related to the fundamental and third harmonic, but the presence of distinct frequency components is clearly lost when going from $F_0 = 2$ to $F_0 = 3$, spreading the energy over a wider range of the dispersion spectrum.

A final comment is made on the position of the higher harmonic peaks in Figure 3.8. Two peaks in the higher harmonic range are identified by two different markers. The red plus-sign identifies the higher harmonic $3\Omega/\omega_n$, while the magenta asterisk identifies the limit point on the dispersion branch very close to the higher harmonic. The dispersion curve has zero slope at this particular point, i.e., the group velocity $c_g = \partial\omega/\partial\mu = 0$, whereby this

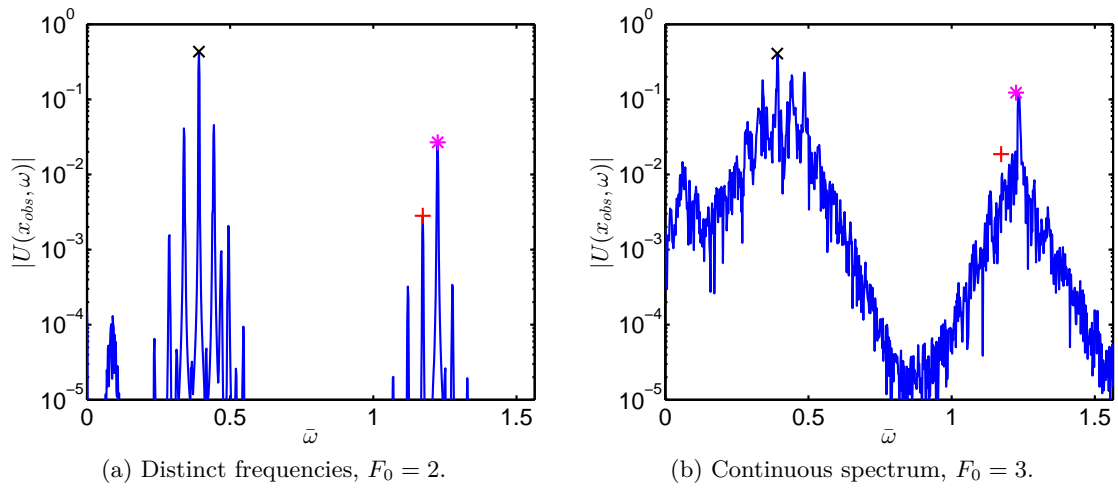


Figure 3.8: Temporal Fourier transforms for large input forcing. Black cross: Loading frequency. Red plus-sign: Higher harmonic. Magenta asterisk: Pass band limit

point represents a standing wave-mode. This implies a minimal required amount of energy associated with motion at this point, whereby the higher harmonic energy tends to favour this point. This phenomenon is not captured directly by the wave-analysis provided by the analytical model, which essentially predicted a larger higher harmonic generation based on a wrong assumption of energy distribution in the chain. Hence, for higher harmonic predictions, in particular near internal resonance points and standing wave-modes, the analytical results from the wave-based material analysis does not necessarily apply directly to a corresponding finite system. If a large energy transfer between modes, based on internal resonance, is desired it seems that analysis of the specific finite system is necessary, in particular if a systematic optimization framework is to be developed.

Chapter 4

Inertial amplification

The present chapter presents a novel application of the concept of inertial amplification, as described in [P2]. The chapter elaborates a bit on the historical perspective of the concept, after which the effects of the phenomenon are presented, leaving all mathematical derivations in the paper and the appendices. The paper contains a detailed parameter study, of which only the most important analyses are included here. The present chapter further contains an extension of the analysis in the paper, determining the band-gap limits by a modal approach in Section 4.4, where the determination of antiresonance frequencies from [P2] is also generalized.

4.1 A brief historical account

The idealized mechanical elements, the spring and the dashpot, illustrated in Figure 4.1, provide forces proportional to the relative displacement and velocity between the points of attachment.



Figure 4.1: Ideal mechanical elements.

Given the displacement or velocity at the two terminals, the elastic spring and viscous damper forces are given by:

$$f_s = k(x_2 - x_1), \quad (4.1a)$$

$$f_d = c(\dot{x}_2 - \dot{x}_1), \quad (4.1b)$$

where the constants of proportionality k and c are the spring stiffness and the dashpot viscosity respectively. The inertial force corresponding to an accelerating mass on the other hand is proportional to the absolute acceleration of the mass. This is a direct consequence of Newton's

second law in an inertial frame of reference, and as such not a problem. The mass, however, cannot be seen as a direct equivalent to the spring or dashpot which, inspired by an electrical-mechanical analogy, lead to the development of the *inertor*, (Smith 2002). The inertor is the ideal inertial equivalent of the spring and dashpot, providing a force proportional to the relative acceleration between two points of attachment. The schematic representation of the inertor is seen in Figure 4.2, and the force, f_i , is given in Eq. (4.2) where the constant of proportionality b is called the inertance.



Figure 4.2: Inertor schematic.

The inertor has been realized experimentally, and an important point is that the inertance can be much larger than the actual mass of the element, (Smith 2002, Papageorgiou & Smith 2005, Papageorgiou, Houghton & Smith 2009). This means that a relatively large effect can be derived from a comparably small mass. The device has been used in vehicle suspension systems in particular in the Formula One industry, where its impressive performance caused the 2007 Formula One spy scandal, (Chen et al. 2009), as mentioned in Chapter 2.

While the inertor development, apparently first motivated by an electrical analogy, was indeed novel and of great importance in terms of practical mechanical filter design, the idea of utilizing inertial forces between two points in a structure for mechanical filtering purposes is not as novel. It reaches back (at least) to the patent taken out by Flannelly in 1967 on the “*Dynamic antiresonant vibration isolator*”, (Flannelly 1967). Flannelly used a levered mass to create the inertial forces that provided *antiresonance* frequencies, frequencies where the transfer function is zero. Figure 4.3 shows a reproduced schematic of the system patented by Flannelly, where a main mass is isolated from ground motion by the levered mass m_a .

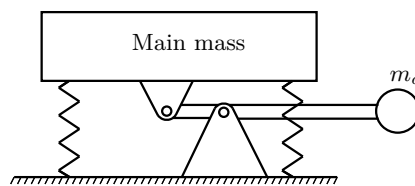


Figure 4.3: Schematic of Dynamic Antiresonant Vibration Isolator. Reproduced from Flannelly (1967).

The inertial force from the mass is enhanced or *amplified* by the lever and at the antiresonance frequencies, the elastic forces in the suspension springs are cancelled by the enhanced inertial forces from m_a .

The use of mass and levers to generate antiresonance frequencies was somewhat revived by Yilmaz & Kikuchi (2006), where various mechanical low-pass filters were analyzed. In particular two types of dynamic antiresonant vibration isolators were analyzed in an almost

periodic setting by considering an array of isolators between the ground and the mass to be isolated. This was followed by a series of papers analyzing how inertial amplification can be incorporated in a periodic framework, (Yilmaz, Hulbert & Kikuchi 2007, Yilmaz & Hulbert 2010, Taniker & Yilmaz 2013, Acar & Yilmaz 2013), illustrating a significant design potential in terms of wide and deep, low-frequency band gaps, compared to what has previously been obtained by classical local resonance. The inertial amplification effect is demonstrated both analytically, numerically and experimentally and recently, shape optimization was used to obtain even wider gaps in a periodic lattice utilizing inertial amplification, (Yuksel & Yilmaz 2015).

4.2 Inertial amplification of continuous structures

Until now, the inertial amplification effect has been implemented primarily by having the mechanism responsible for the effect as a backbone component of the structure. In [P2] we attempt to introduce the effect directly into continuous structures, by applying a light-weight mechanism on the *surface* of a continuous structure. Applying the mechanism on the surface means that it does not contribute to, or interfere with, the main structural functionality of the host structure. The distant future visions of this concept is the development of a type of surface coating that generates low-frequency, wide and deep band gaps, and can be applied to existing structures without having to be included in the early design phase. Figure 4.4 illustrates the first step of the vision, where the mechanisms are still clearly distinguishable.

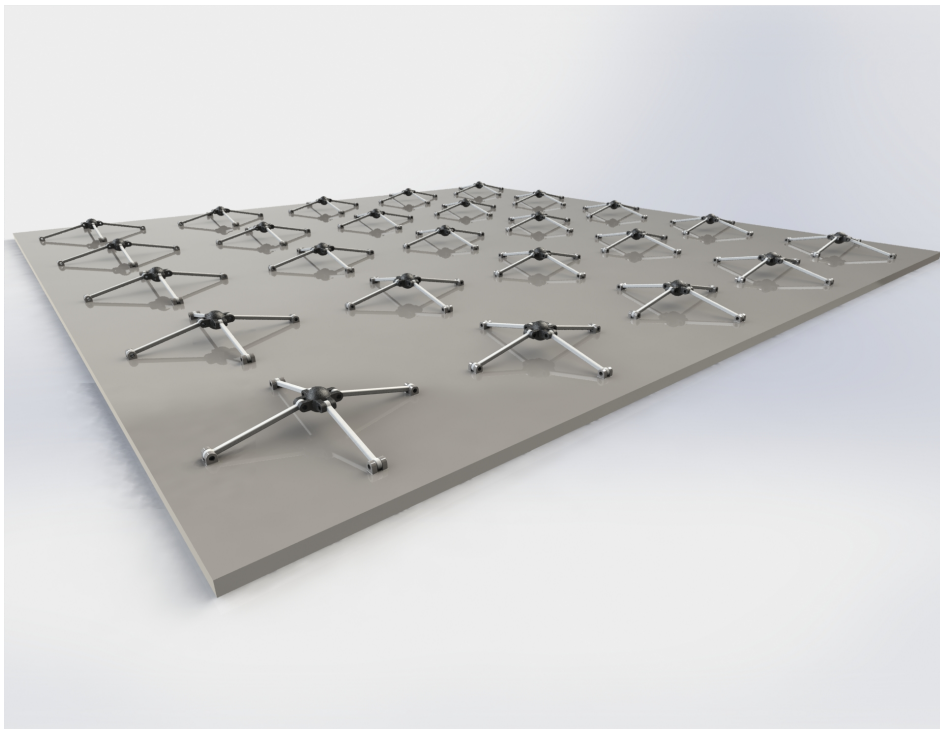


Figure 4.4: Two-dimensional vision of proposed concept. Courtesy of Dimitri Krattiger at University of Colorado Boulder.

Note that this is merely a rendering of an idea, no actual analysis has been carried out on the plate in Figure 4.4. To investigate the general phenomenon in as simple a setting as possible, the complexity of the model in Figure 4.4 is reduced. We decrease dimensionality by considering longitudinal motion in a rod, see Figure 4.5a, and reduce the complexity of the inclined rods and bearings by the simplified hybrid, continuous-discrete model in Figure 4.5b.

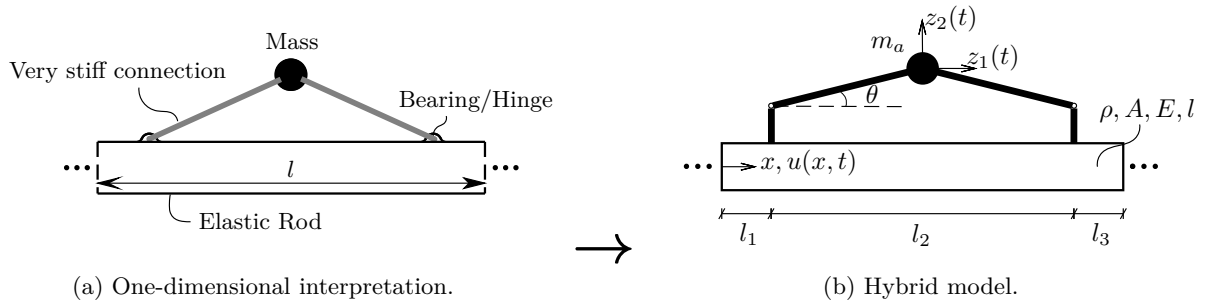


Figure 4.5: Model reduction.

The rod is linear elastic and homogeneous with Young's modulus E , mass density ρ , cross-section area A and length l . The longitudinal motion in the rod is denoted $u(x, t)$, where x is the longitudinal spatial coordinate and t is time. The horizontal and vertical motion of the amplification mass are denoted $z_1(t)$ and $z_2(t)$ respectively, while the amplification mass is denoted m_a and the amplification angle is denoted θ . Heavy lines indicate rigid connections while the corners are moment-free hinges.

4.3 Band structure

The hybrid model in Figure 4.5b is considered as the unit cell of an infinite periodic medium. The band structure of the periodic material is determined using a transfer-matrix approach, which is based on relating the state variables of the host medium - the linear elastic rod - at each end of the unit cell by a transfer matrix. This is combined with the Floquet-Bloch theorem, forming a frequency-dependent eigenvalue problem. The eigenvalue problem is solved for a range of real-valued frequencies ω , providing the wavenumber $\kappa(\omega)$, whereby the band structure is obtained. The mathematical details of the transfer matrix approach for the present system is covered in [P2], in particular how to include the effect of the mechanism is given some attention. For a general presentation of the transfer matrix approach for determining the band structure of elastic systems the reader is referred to Hussein et al. (2006) which provides a very transparent presentation of the topic in relation to a layered rod. The method however, is readily generalizable to flexural waves as well as seen in Liu & Hussein (2012) where wave propagation in periodic structures of both Bernoulli-Euler and Timoshenko beams is considered.

Using the transfer matrix approach, the resulting band structure in the $\kappa(\omega)$ -formulation contains both real and imaginary parts of the wavenumber. A purely real wavenumber corresponds to a propagating wave, while a purely imaginary wavenumber corresponds to a

spatially attenuated wave, hence the wavenumber is purely imaginary within band gaps. The presence of damping complicates the purely real/imaginary picture slightly, since the energy dissipation by the damping means that the $\kappa(\omega)$ -formulation yields imaginary parts of the wavenumber over the full real-valued frequency range, (Mukherjee & Lee 1975). We will keep things simple, hence all analyses are carried out for undamped systems, which means that wave attenuation occurs in the band gaps alone. As an example we consider an aluminum rod with the parameters given in Table 4.1 as the host medium.

Table 4.1: Parameters of the host rod.

E [GPa]	ρ [kg/m ³]	$b \times h$ [m] \times [m]	l [m]	ω_b [rad/s]	m_b [kg]	k_b [N/m]
69.8	2700	0.025×0.025	0.55	$\frac{\pi}{l} \sqrt{\frac{E}{\rho}}$	$\rho A l$	$\frac{EA}{l}$

The table also provides the normalization parameters ω_b , m_b and k_b - the first natural frequency of a fixed-fixed rod of length l , the equivalent mass and equivalent stiffness. Figure 4.6a shows the resulting band structure for a reference system with the mechanism being full-length, i.e. $l_1 = l_3 = 0$ and the amplification parameters $m_a = m_b/10$ and $\theta = \pi/18$. The figure includes both the real and imaginary part of the normalized wavenumber, $\text{Re}[\kappa l]$ and $\text{Im}[\kappa l]$. They represent propagating and evanescent waves respectively. The figure also illustrates the band structure for a homogeneous aluminum rod without the mechanism (blue dotted curve). The band structure is shown in the normalized frequency range $\bar{\omega} = \omega/\omega_b$. Furthermore, Figure 4.6b shows the band structure for the reference system rotated 90 degrees along with the transmissibility for a finite system of $n = 5$ unit cells.

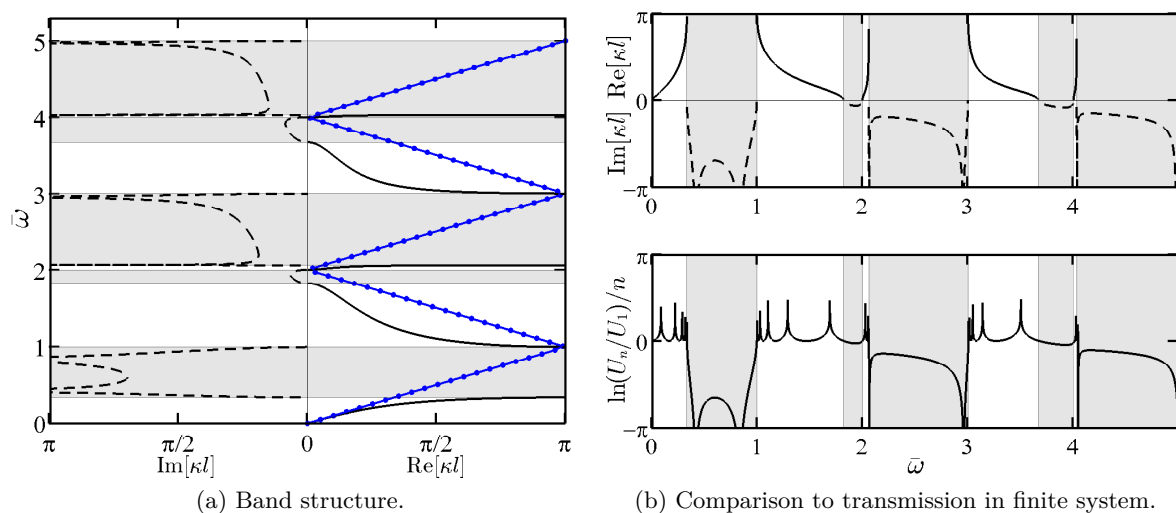


Figure 4.6: Band structure and comparison to transmission in a finite system.

The transmissibility is defined as the natural logarithm of the ratio between output and input displacement (U_n and U_1) divided by the number of unit cells (n), obtained by applying

harmonic forcing at the input end of the hybrid system. This allows for easy comparison with the unit cell based results in the band structure.

Figure 4.6a illustrates how the application of the presented mechanism opens up several gaps in the otherwise continuous band structure of the homogeneous rod. It is noted that the dotted blue curve for the homogeneous rod has been “folded” in order to present the results in the Irreducible Brillouin Zone, however as mentioned in Chapter 2, for each branch, the physical wavenumber spans higher Brillouin zones. The first band gap is commonly of particular interest since the objective in industrial applications often is to create large *low-frequency* band gaps. For the present example the first gap has a normalized central frequency $\bar{\omega}_1^c$ and gap width $\Delta\bar{\omega}_1$ of:

$$\bar{\omega}_1^c = 66.9\%, \quad \Delta\bar{\omega}_1 = \frac{\bar{\omega}_1^u - \bar{\omega}_1^l}{\bar{\omega}_1^c} = 99.1\%, \quad (4.3)$$

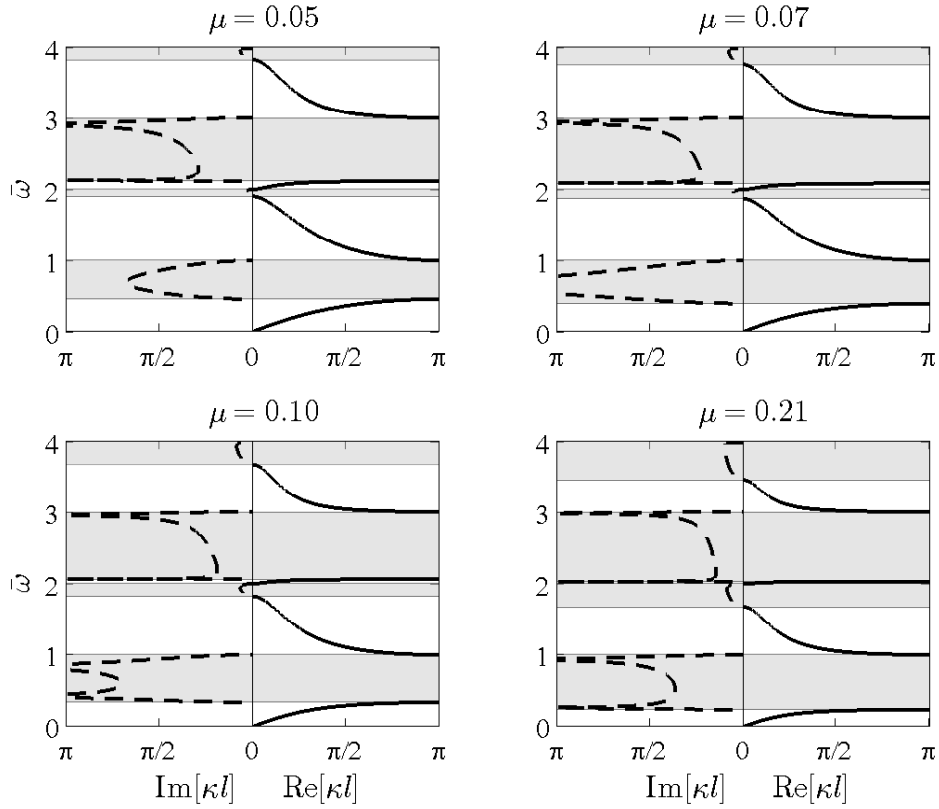
which, compared to what can be obtained for the similar system utilizing local resonance, is rather wide, as will be described in Section 4.3.2. Figure 4.6b illustrates how the results from the infinite analysis transfers to the finite setting, by comparing the transmission in a five-cell finite structure to the band structure. Aside from illustrating the gap behaviour in the finite system, the comparison between the imaginary part of the wavenumber, or *attenuation constant*, and the transmission profile illustrates that the former represents spatial decay per unit cell. The peaks of the attenuation constant occurs at the antiresonances of the system, where the transmission is theoretically zero. These frequencies are obviously of great design interest, since they govern the overall “depth” of the gap, i.e., they govern the attenuation strength of the system. The possibility of having multiple antiresonances in a gap is very appealing since it keeps the general level of attenuation higher.

4.3.1 Attenuation profiles

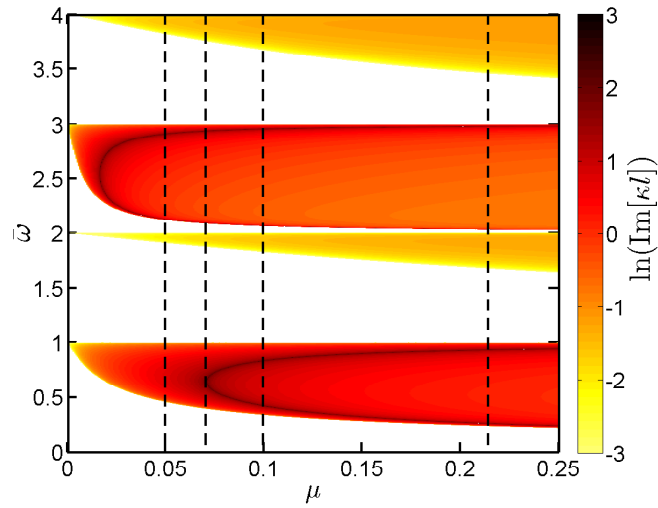
Since the attenuation constant is such a crucial quantity for band gap design and behaviour, and thereby wave and vibration attenuation, we mapped its dependency on various system parameters in [P2]. The investigation in the paper is rather thorough, thus only the most interesting and relevant results and analyses will be presented here.

Figure 4.7 illustrates how the band structures and attenuation develop with added mass ratio $\mu = m_a/m_b$. The attenuation profile is here defined as the natural logarithm of the normalized attenuation constant, $\ln(\text{Im}[\kappa l])$, whereby the strength of attenuation is largest for the deep red colors in Figure 4.7b.

The four illustrated band structures in Figure 4.7a are for the four vertical dashed lines in the attenuation profile in Figure 4.7b. The illustrated band structures show that when the mass ratio is too low, $\mu = 0.05$, the enhanced inertia is not sufficient to generate true antiresonance frequencies in the low-frequency range. Hence, the first gap is of Bragg-type, being a result of destructive interference between reflected and propagating waves. As the mass ratio is increased, a single antiresonance is generated at $\mu = 0.07$, which then branches into two distinct antiresonance frequencies that separate with increased mass ratio. This continuous development can be seen from the deep red lines in the attenuation profile, appearing at the antiresonance frequencies. As the distance between the antiresonances in the first



(a) Band structures.



(b) Attenuation profile.

Figure 4.7: Band structures and attenuation profile for full-length mechanism.

gap increases, the depth of the gap is noted to decrease, indicating a trade-off between gap width and -depth, i.e., a trade-off between the frequency range of attenuation and strength of attenuation.

Introducing the additional design parameter, the mechanism length l_2 , increases the design

space accordingly. Figure 4.8 illustrates the attenuation profile for varying length ratio $\bar{l} = l_2/l$, i.e., the ratio of mechanism length to full unit-cell length. The attenuation profile is shown for two values of mass ratio, $\mu = 0.05$ and $\mu = 0.1$.

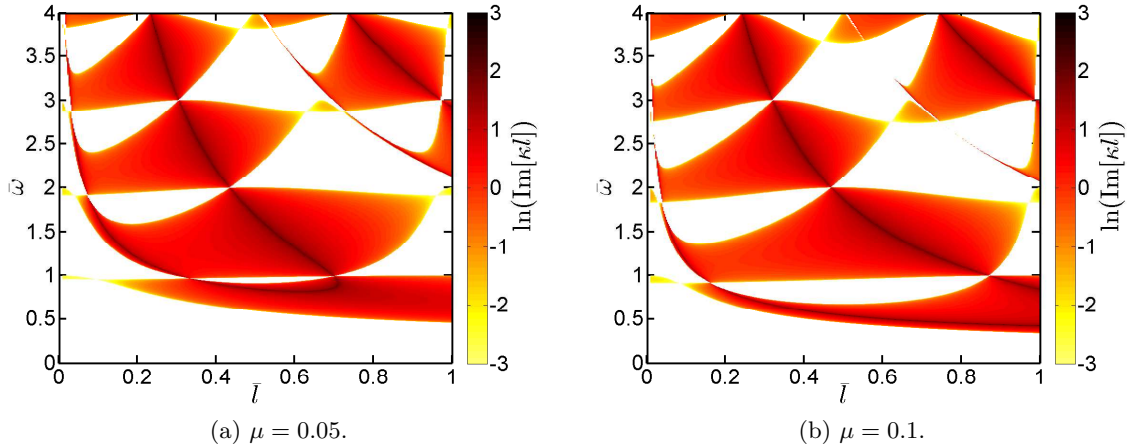
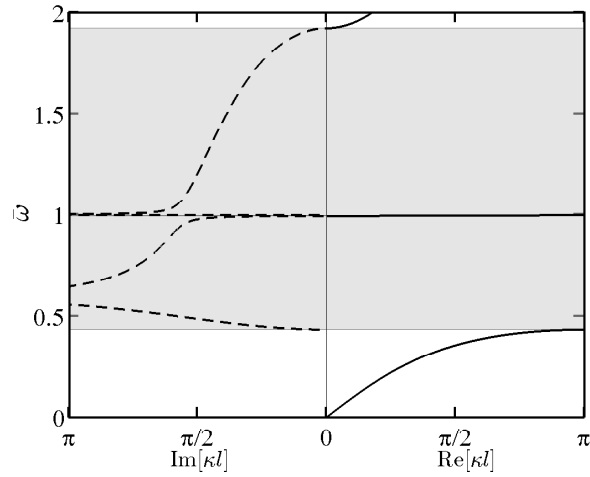
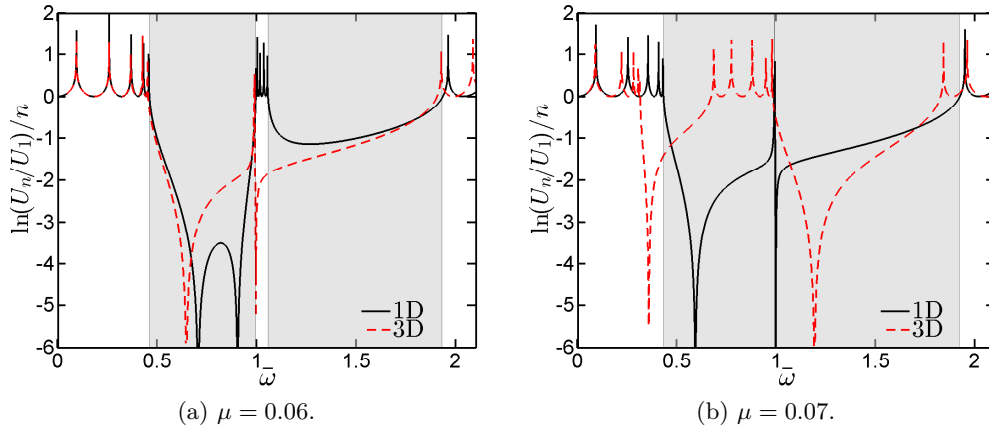


Figure 4.8: Attenuation profiles for varying length ratio $\bar{l} = l_2/l$.

For the lower mass ratio, the enhanced inertial forces are not sufficient to generate antiresonances for the full-length mechanism, however a single antiresonance is generated at approximately $\bar{l} = 0.7$ which then branches into two distinct branches, similar to what happened with increased mass in Figure 4.7b, albeit for decreasing \bar{l} . Additionally, the antiresonance branches are seen to “jump gaps”, as the length ratio is decreased. This is attributed to the fact that the enhanced inertia depends on the difference in acceleration between two points, whereby the higher modes activate the mechanism more as the distance between attachment points is decreased. At the points of antiresonance transition, two neighbouring gaps are seen to almost collapse, hence it is tempting to design for such a point in order to obtain a total gap width as the sum of two neighbouring gaps. Figure 4.9 illustrates the band structure at a coalescence point for $\bar{l} = 0.8$ and $\mu = 0.07$.

The two gaps can be seen to almost collapse, separated by a standing wave-mode illustrated by the horizontal line in the real part of the wavenumber/frequency spectrum. Hence, gap-coalescence in reality means *almost*-gap-coalescence, and furthermore, these points are just that - points. The phenomenon is rather singular, as illustrated by the transmissibility plots in Figure 4.10. The transmissibilities are calculated using the same one-dimensional model as used in Figure 4.6b, as well as a three-dimensional implementation in the commercial FE-software ABAQUS.

Figure 4.10a illustrates gap coalescence for the 3D beam model in ABAQUS, obtained for the mass ratio $\mu = 0.06$, while Figure 4.10b illustrates gap coalescence in the analytical model, obtained for $\mu = 0.07$. Hence, even though the coalescence phenomenon exists, it is rather sensitive to modelling inaccuracies since the one-dimensional and three-dimensional models predict coalescence for different mass ratios. Thus, practical realization of a design providing gap coalescence would require a physically exact model as well as zero production tolerances. Hence, the gap-coalescence effect is probably not the greatest practical contribution from the

Figure 4.9: Band-gap coalescence. $\bar{l} = 0.8$, $\mu = 0.07$.Figure 4.10: Singularity of coalescence. $\bar{l} = 0.8$. Gray areas are band gap regions predicted by the analytical material model.

application of inertial amplification mechanisms to continuous structures.

4.3.2 Performance compared to other methods

As mentioned in Chapter 2, band gaps are usually generated by two phenomena - Bragg scattering or local resonance - while the utilization of inertial amplification is still somewhat unexploited. The application of inertial amplification mechanisms is best comparable to the application of local resonators in several aspects. Both methods generate antiresonance frequencies, and have the design freedom of placing these antiresonances wherever, given complete freedom in the design variables. Bragg scattering on the other hand does not generate antiresonance frequencies and the position of gaps are directly governed by the periodicity of the system. Figure 4.11 compares the proposed inertial amplification concept to the classical approach using local resonance.

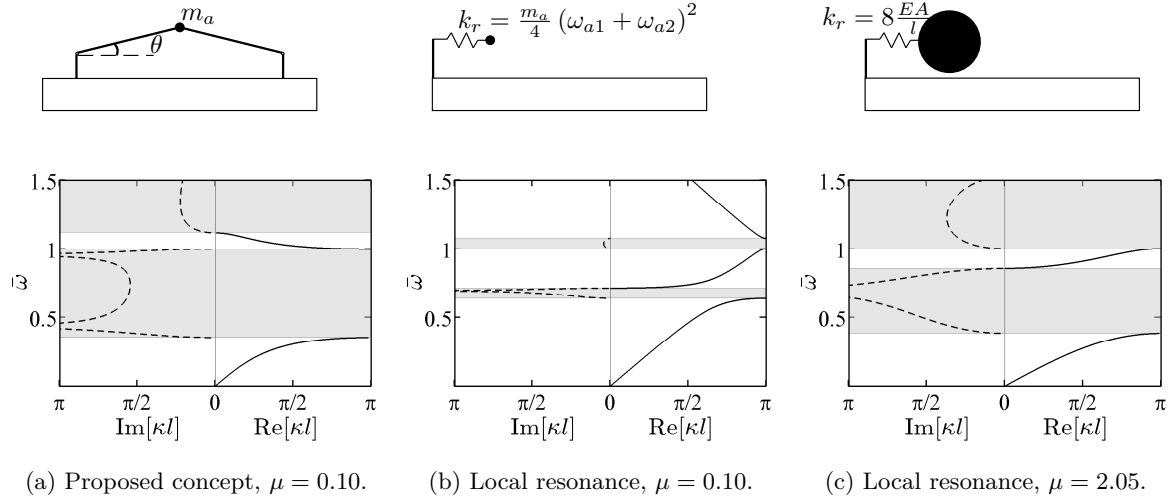
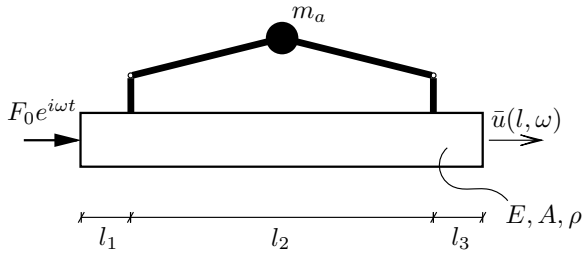


Figure 4.11: Comparison to classical local resonance.

The addition of the local resonator requires a choice of stiffness tuning. Figure 4.11b shows the band structure for the tuning that provides the same central frequency of the band gap for the local resonance and inertial amplification mechanism respectively. The mass increase is the same in the two cases, illustrating the potential of the inertial amplification mechanism compared to the classical local resonator case. In order to drive this point home, Figure 4.11c illustrates the band structure for the classical local resonance case, where the parameters have been chosen to generate a gap of comparable width to the inertial amplification case. As indicated by the sketch, the mass needs to be approximately twenty times heavier than what is needed for the inertial amplification case. Furthermore the resonator needs to have a normalized stiffness of $\bar{k}_r = k_r/k_b = 8$. These mass and stiffness values are not feasible for practical applications, and furthermore the notion of a “main structure” with applied local resonators is no longer meaningful.

4.4 Band gap limits and antiresonances

For practical gap design and optimization purposes, the position and width of the gap are very relevant parameters. Considering the attenuation profiles in, e.g., Figure 4.8, each point represents the solution of an eigenvalue problem, which means that covering a large design space using the transfer matrix method might not be feasible. Hence, it would be preferable with direct expressions for gap limits and antiresonance frequencies, which fortunately can be derived relatively easy. The determination of antiresonances is described in [P2] for the simple case of full-length mechanism, $\bar{l} = 1$. We used a receptance approach, determining the antiresonances as those frequencies of zero displacement at one end when applying harmonic loading at the other end, see Figure 4.12. Equation (4.4) provides the displacement as function of input frequency, hence the antiresonances satisfy $H_{0l}(\omega) = 0$.



$$\bar{u}(l, \omega) = H_{0l}(\omega)F_0. \quad (4.4)$$

Figure 4.12: Loaded unit cell.

The receptance function, $H_{0l}(\omega)$, for the full-length mechanism is derived in [P2], and the expression is relatively simple. The receptance function for the general case can be found in a similar way, however its expression becomes quite a bit more cumbersome, since it requires the inversion of a six-by-six matrix rather than a two-by-two for the simple case. It turns out however, that the *numerator* of $H_{0l}(\omega)$ does not change much when considering the general case, which means that the equation for the antiresonances is almost identical,

$$EA\kappa_b - \omega^2 \frac{m_a}{4} (\cot^2 \theta - 1) \sin \kappa_b l_2 = 0, \quad (4.5)$$

where it can be seen that the only difference is that the length parameter in the sine function has changed from l to l_2 . The equation for predicting antiresonance frequencies can be solved numerically for any desired number of frequencies. A simple Newton-Raphson scheme is used for the antiresonance predictions in [P2], the same scheme will be used for the examples in the present section.

The gap limits are the second set of parameters that we would like to be able to predict without determining the full band structure. This can be done by determining the natural frequencies for a single unit cell with its boundaries either free-free or fixed-fixed, provided that the unit cell is symmetric, as described in Mead (1975). Determining the natural frequencies of the two systems in Figure 4.13 manually is somewhat cumbersome, and the obtained equations require numerical solution techniques.

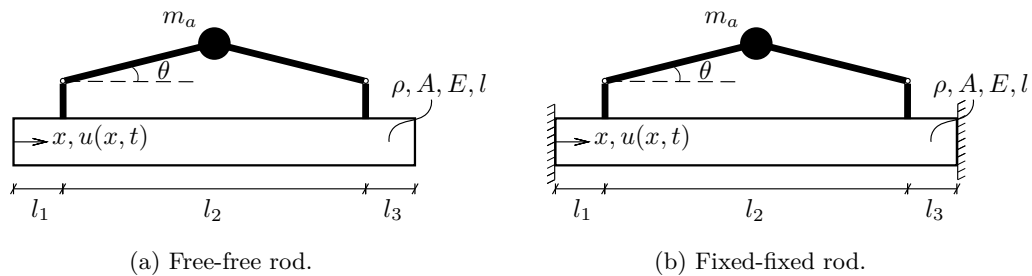


Figure 4.13: Single unit cell with applied boundary conditions.

As an alternative approach, we propose to utilize a direct, modal expansion, where the solution to the governing equation for a single unit cell is expanded in the undamped mode shapes for the homogeneous rod. The classical, simple modal decoupling is prevented by the

applied mechanism, hence the mode shape expansion leads to a discretization of the continuous equation of motion as,

$$\mathbf{M}\ddot{\boldsymbol{\xi}}(t) + \mathbf{K}\boldsymbol{\xi}(t) = \mathbf{0}, \quad (4.6)$$

where $\boldsymbol{\xi}(t) = [\xi_1(t) \xi_2(t) \cdots \xi_N(t)]^T$ is a vector of modal coordinates, \mathbf{K} is the stiffness matrix and \mathbf{M} is the mass matrix, that includes the contribution from the inertial amplification mechanism, and is densely populated in general. The mass and stiffness matrices are $N \times N$, where N is the number of modes retained. The modal mass and stiffness matrices are derived in Appendix A.

The natural frequencies obtained from the modal discretization predicts the limits of the band gaps of the infinite array of unit cells. The number of modes needed for a reasonably accurate result depend on the specific system, in particular the internal attachment length l_2 is extremely important for the convergence of the eigenvalues of the system of equations in Eq. (4.6). Figure 4.14 illustrates how the gap predictions (dashed lines) follow the gap limits of the attenuation profile for varying relative internal length $\bar{l} = l_2/l$ when using $N = 100$ modes. Similarly, the antiresonances (black crosses) follow the peak attenuation lines nicely, providing a simpler set of parameters for optimization and design purposes.

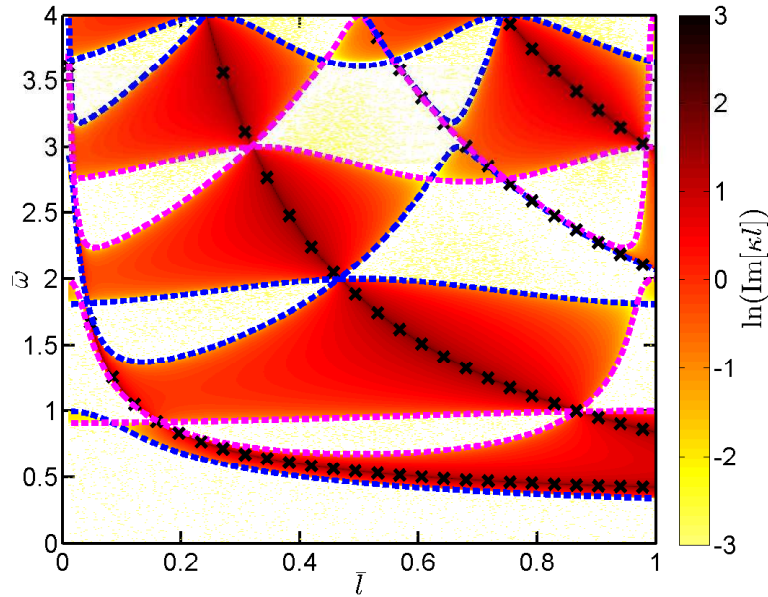


Figure 4.14: Attenuation profile with predicted gap limits and antiresonances. $\mu = 0.1$. Blue: Free-free. Magenta: Fixed-fixed. Black: Antiresonances.

4.4.1 Low-frequency gap design

The main motivation for developing the inertial amplification system for continuous structures was to obtain low-frequency band gaps, hence this chapter will conclude with a simple demonstration of how the gap-limit and antiresonance predictions can be used to optimize the first band gap. The optimization procedure will be rather manual, but even so, the opti-

mization criteria and constraints must be chosen carefully to obtain meaningful results. For example, when considering Figure 4.14, we see that the first gap is limited by the natural frequencies of the free-free cell from below and of the fixed-fixed cell from above, except for a small interval near $\bar{l} = 0$. Hence, if the upper limit of the gap, ω_1^u in Eq. (4.3) is assumed to be the fixed-fixed frequency, certain ranges of parameters will lead to erroneous results. Similarly, maximizing the distance between the first two antiresonance frequencies will not necessarily provide a wide first gap, since the second antiresonance might be in a higher gap, or the antiresonances might first occur for higher modes as illustrated in Figure 4.8a where no antiresonances are present in the first gap for $\bar{l} \gtrsim 0.7$. Hence, we must clarify exactly what we mean by “optimal”, and how this is formulated in a robust manner. For this example, it will be utilized that two antiresonances in a gap means large attenuation over the full gap range, as well as a rather wide gap. Hence, the optimization problem is to maximize the normalized distance between the first two antiresonances, subject to the constraints $c_1 - c_3$:

$$\begin{aligned}
& \text{Maximize} && \Delta\omega_a(\bar{l}, \mu) = \frac{|\omega_{a2} - \omega_{a1}|}{\frac{1}{2}(\omega_{a2} + \omega_{a1})} \\
& 0 < \bar{l} < 1 \\
& 0 < \mu < 0.8 \\
& \text{Subject to} && c_1 : \omega_{1a} > \omega_1^l \\
& && c_2 : \omega_{2a} < \omega_1^u \\
& && c_3 : \omega_1^u > \omega_1^l,
\end{aligned} \tag{4.7}$$

where the design variables are the internal length ratio \bar{l} and the added mass ratio μ . The constraints c_1 and c_2 ensure two antiresonances in the gap, while the constraint c_3 ensures that the correct gap limit predictions are used for upper and lower gap limit respectively. The absolute value of the difference between the two antiresonance frequencies ensures that the objective is invariant with the order of the antiresonance frequencies. The optimization problem in Eq. (4.7) is not implemented in an actual optimization framework, but the objective function $\Delta\omega_a$ is calculated for the chosen range of the design variables. Figure 4.15 illustrates the contour of the normalized antiresonance distance, where the constraints have been enforced by only calculating the objective when they are fulfilled and setting it to zero everywhere else.

The contour illustrates a rather narrow domain where the constraints are fulfilled. Within that region, the largest gap is obtained by the trivial optimization solution of maximizing both design variables. In the low-mass range however, we see that the constraints are fulfilled for lower values of the internal length ratio, whereby a double-peak first gap can only be obtained for $\bar{l} = 0.8$ if $\mu = 0.06$. The band structures corresponding to the two black crosses in Figure 4.15 are shown in Figure 4.16, where the range of the attenuation constant has been doubled.

The band structure in Figure 4.16a illustrates that the actual gap width can be larger than predicted by the distance between antiresonances, which actually also provides a larger overall gap depth. The actual gap width for the parameter combination $(\bar{l}, \mu) = (0.80, 0.06)$ is:

$$\Delta\bar{\omega}_1 = \frac{\bar{\omega}_1^u - \bar{\omega}_1^l}{\frac{1}{2}(\bar{\omega}_1^u + \bar{\omega}_1^l)} = 2 \frac{1.00 - 0.46}{(1.00 + 0.46)} = 73.0\%, \tag{4.8}$$

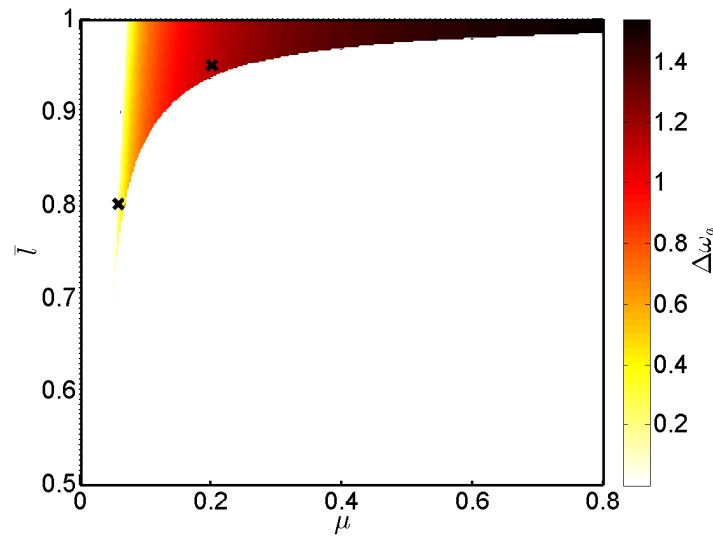


Figure 4.15: First-gap design.

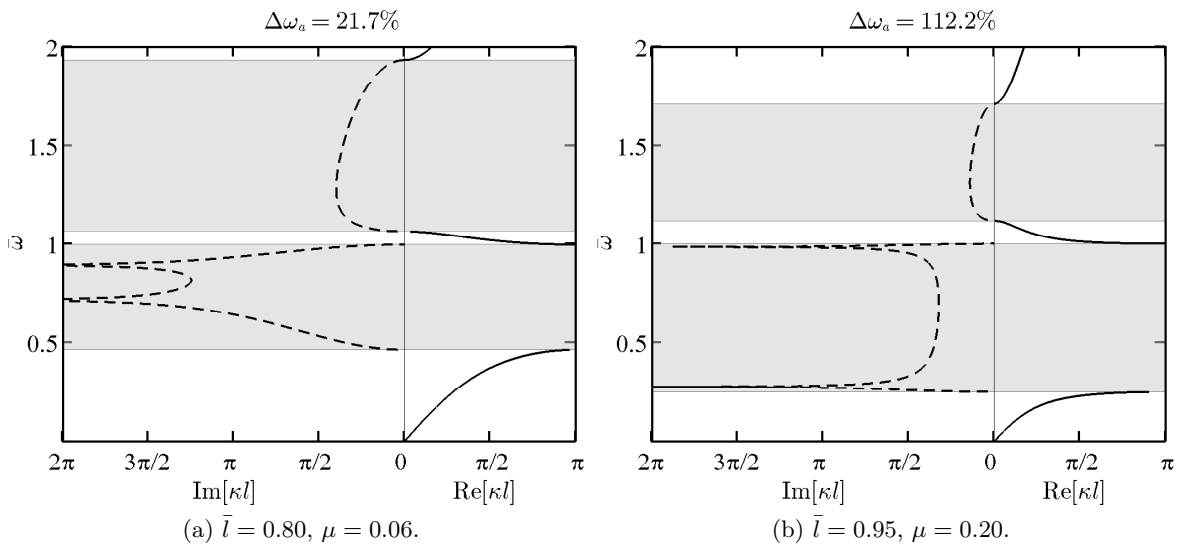


Figure 4.16: Illustrative band structures.

which, depending on how much the increased attenuation constant weighs in your objective, might actually be a better design than the $(\bar{l}, \mu) = (0.95, 0.20)$ -case illustrated in Figure 4.16b. Hence, design based on the manual optimization illustrated by the surface in Figure 4.15 should still be evaluated post-optimization.

As the modelling complexity increases, so does the number of design variables and in turn the complexity of the optimization problem. For starters, it is no longer possible to visualize the optimization domain by a surface as in Figure 4.15 when the design variables increases above two, and manual optimization by trial-and-error begins to become very cumbersome. Hence, an automated, systematic and robust optimization framework becomes prudent as the modelling accuracy increases. The shape optimization carried out in Yuksel & Yilmaz (2015)

is an example of this, changing the shape of an original design to improve performance. The next step seems to be applying topology optimization to allow for more freedom in the design than is provided by shape optimization.

Chapter 5

Inertial amplification extensions

The inertial amplification model described in Chapter 4 and [P2] is a basic model meant to illustrate various effects of the concept. The present chapter considers a number of extensions of the simple hybrid rod-mechanism model to investigate the general applicability of inertial amplification. The nature of the chapter is slightly more detailed than the previous chapters, however very elaborate arithmetic and algebra have been confined to appendices for the interested. The chapter presents original material that scratches the surface of the next step in the research on inertial amplification of continuous structures. Section 5.1 explores the real-life applicability of the concept, first by considering realistic material parameters of the model from Chapter 4 and then presenting experimental results of a similar mechanism designed for transverse vibrations. Section 5.2 considers nonlinear kinematics of the mechanism to investigate the validity range of the linearization utilized in [P2].

5.1 Is it real?

When working with reduced models as the hybrid rod-mechanism model in [P2], it is always a concern whether or not the model reduction is too severe, i.e., if the model captures the physics properly. This can be tested by general numerical models or experiments. This section will present a bit of both, first illustrating that relaxing the “rigid and massless” constraint of the connecting links does not drown the inertial amplification effect, but rather puts some constraints on the relative frequency range. Secondly, Section 5.1.2 presents experimental results from applying the mechanism to a beam and investigating its effect on transverse vibrations. The work presented in Section 5.1.2 has been carried out by Mr. Mateusz Barys under the supervision of Professor Jakob Søndergaard Jensen and myself as part of his M.Sc.-project. Hence, all credit goes to Mr. Barys, the results have been included to illustrate that the work in [P2] indeed has practical applications.

5.1.1 Flexible connecting beams

The model using three-dimensional beam elements created in ABAQUS for numerical validation of the transmissibilities in [P2] is now used to verify that the inertial amplification effect can occur for more realistic systems as well. Using flexible elements, the inertial ampli-

fication effect occurs primarily when the antiresonance frequency by inertial amplification is much lower than the local resonance frequency of the mechanism, as also described in Yilmaz & Hulbert (2010). For the five-cell system depicted in Figure 5.1 this means that special attention should be paid to the inclined connecting beams.

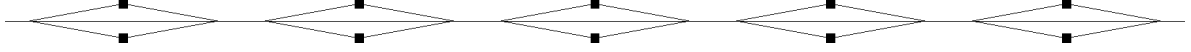


Figure 5.1: Beam model in ABAQUS.

The mechanisms are distributed symmetrically above and below the host beam to avoid bending phenomena, since we are investigating longitudinal wave motion in the host beam.

Design considerations

Going from the ideal to realistic material parameters, it is of interest to have a material with as high a stiffness-to-density ratio as possible. A good candidate seems to be carbon-fiber reinforced polymers, having a stiffness as large as for steel and a considerably lower density. Furthermore, the cross-section should be designed to maximize the first beam-bending frequency of the inclined beams, placing most of the material at the outer edges of the cross-section. For practical purposes, a circular or rectangular box section seems to be appropriate. Finally, the axial stiffness of the inclined beams should be large enough to ensure that the axial strain is confined mostly to the host beam, if the ideal and flexible models are to produce comparable results.

The above design considerations have led to the rectangular, hollow-tube cross-section design for the inclined beams illustrated in Figure 5.2, with the geometric and material parameters given in Table 5.1. The main beam is a solid, square aluminum beam with cross-section dimensions and material parameters given in Table 5.1 as well.

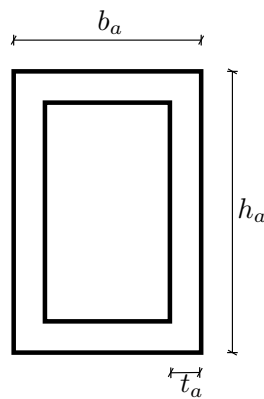


Table 5.1: Geometric and material properties.

Inclined beam					
h_a	b_a	t_a	θ	E_a	ρ_a
[m]	[m]	[m]	[rad]	[GPa]	[kg/m ³]
0.065	0.05	0.01	$\pi/18$	230	1550
Main beam					
h	b	l	l_2/l	E	ρ
[m]	[m]	[m]	[-]	[GPa]	[kg/m ³]
0.06	0.06	0.55	0.8	69.8	2700

Figure 5.2: Cross-section of inclined beams.

The fact that the inclined beams are no longer modelled as massless affects the total mass of the mechanism. This effect should be taken into account when comparing the analytical model with rigid and massless connecting links to the physically realistic model. This has been done by assuming that the inclined connecting beams move the top mass by rigid body

motion, and that their center of gravity is located at the mid-span of the beams. The effective mass contribution of the inclined beams can be estimated by an energy equivalence to the case with rigid, massless connections and all the mass at the top. The effective mass contribution is half the total mass of the inclined beams, m_{ic} . The total mass of the inclined beams per unit cell is $m_{ic} = 4\rho_a A_a l_a$ where l_a is the length of one inclined beam. The amplification mass provided to the analytical model is then:

$$\tilde{m}_a = m_a + \frac{1}{2}m_{ic}, \quad (5.1)$$

and more importantly the actual added mass ratio $\tilde{\mu}$ is:

$$\tilde{\mu} = \frac{m_a}{\rho A l} + \frac{m_{ic}}{\rho A l}, \quad (5.2)$$

hence, with realistic parameters, the mass ratio for a particular design increases. If a particular mass ratio is desired, the process should be inverted, determining the needed m_a from the required mass ratio $\tilde{\mu}$ and the mass of the actual connecting beams to be used. For this analysis, using an applied top mass ratio of $\mu = 0.05$, the actual mass ratio is:

$$\tilde{\mu} = 0.05 + 0.71 = 0.76, \quad (5.3)$$

hence, the inclined beams increase the added mass ratio significantly, and for a specific design, it enforces a constraint on the minimum added mass. Figure 5.3 shows the comparison between the one-dimensional model using massless, rigid connection links and the three-dimensional beam model using flexible connecting beams. The gray shading represents the band gaps for the corresponding material using the effective mass \tilde{m}_a at the top point.

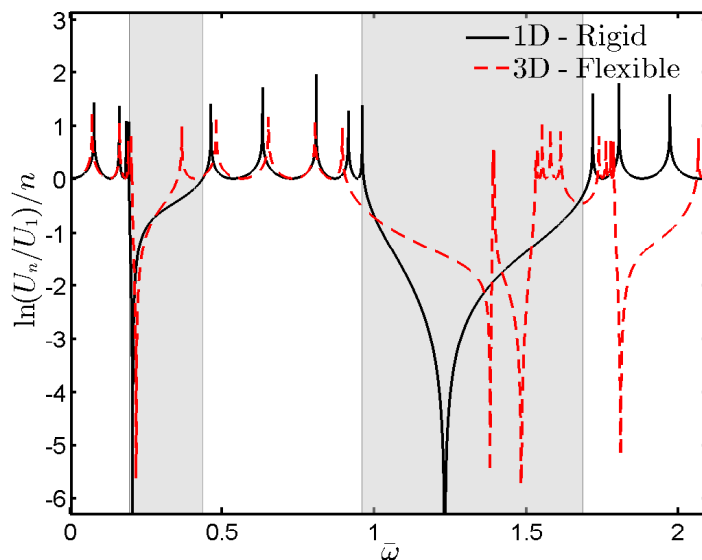


Figure 5.3: Inertial amplification for flexible structure.

The models are seen to agree below and at the first antiresonance, but as the frequency increases the model diverge as expected from the antiresonant tuning of the one-dimensional

model. The figure verifies the existence of inertial amplification-generated antiresonance frequencies even for realistic systems. Figure 5.4 illustrates the deformation at the antiresonance frequency extracted from ABAQUS.

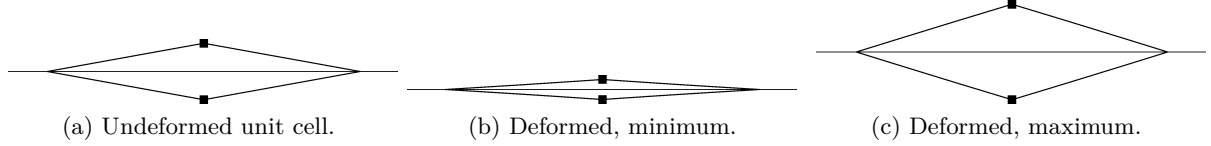


Figure 5.4: Illustration of deformation at antiresonance, $\bar{\omega} = 0.37$.

The motion is indeed seen to resemble rigid body motion of the connecting beams, which has been verified by comparing the normal stress level in the inclined beams and main beam, finding it to be orders of magnitudes smaller in the inclined beams.

The flexible beam model illustrates that the inertial amplification mechanism can indeed be used to generate band gaps for longitudinal waves in several frequency ranges. The fact that the first few natural frequencies of beams are commonly lower than those of rods (see Figure 2.2) complicates the design somewhat, as illustrated by the need for a rather large cross-section of the inclined beams as seen in Figure 5.2 and Table 5.1. If the mechanism is used to generate band gaps in a frequency range relevant for transverse vibrations of the host beam, the natural frequencies of the inclined beams could more easily be forced to be much larger than the target frequency range. This point has led to the development of the results in the next section, which also takes the real-life investigations a step further by presenting experimental results for a single unit cell of a beam with the mechanism applied.

5.1.2 Experimental transverse vibrations

The mechanism presented in [P2] was developed to generate band gaps for longitudinal wave attenuation, and thus, to mitigate longitudinal vibrations. A natural extension is the application to transverse waves/vibrations, which has been the topic of an M.Sc.-project carried out by Mr. Mateusz Barys and supervised by Professor Jakob Søndergaard Jensen and myself during the fall 2015/spring 2016. This section contains some experimental results from the project, meant to illustrate that the inertial amplification mechanism developed in [P2] can work for transverse vibrations as well.

The working principle of the mechanism is to generate longitudinal forces, proportional to the relative longitudinal acceleration between the points of attachment. This principle can work if the mechanism is applied to the surface of, e.g., a beam in flexural vibrations as illustrated by the deformed beam/mechanism system in Figure 5.5.

The horizontal motion at the points of attachment, $u_1 = u(x_1, -h/2, t)$ and $u_2 = u(x_2, -h/2, t)$ are related to the cross-section inclinations ψ_1 and ψ_2 through the trigonometric relations:

$$\sin \psi_1 = \frac{u_1}{h/2}, \quad \sin \psi_2 = \frac{u_2}{h/2}, \quad (5.4)$$

which can be simplified, depending on your approximation choices. For example, Bernoulli-Euler beam theory, assuming small cross-section angles, yields $\sin \psi_i = \psi_i = w'(x_i, t)$. For

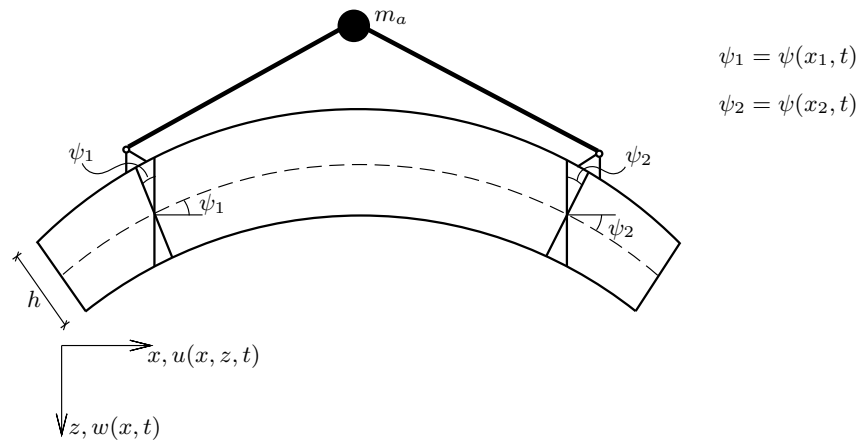


Figure 5.5: Deformed beam with applied mechanism.

the present purpose, Figure 5.5 serves to illustrate that the mechanism can work for bending vibrations as well, due to the longitudinal strain of the outer fibres of the cross-section of a beam in bending, whereby the beam height and mechanism support height become additional important design quantities.

The experimental setup is based on the design illustrated in Figure 5.6. The main beam

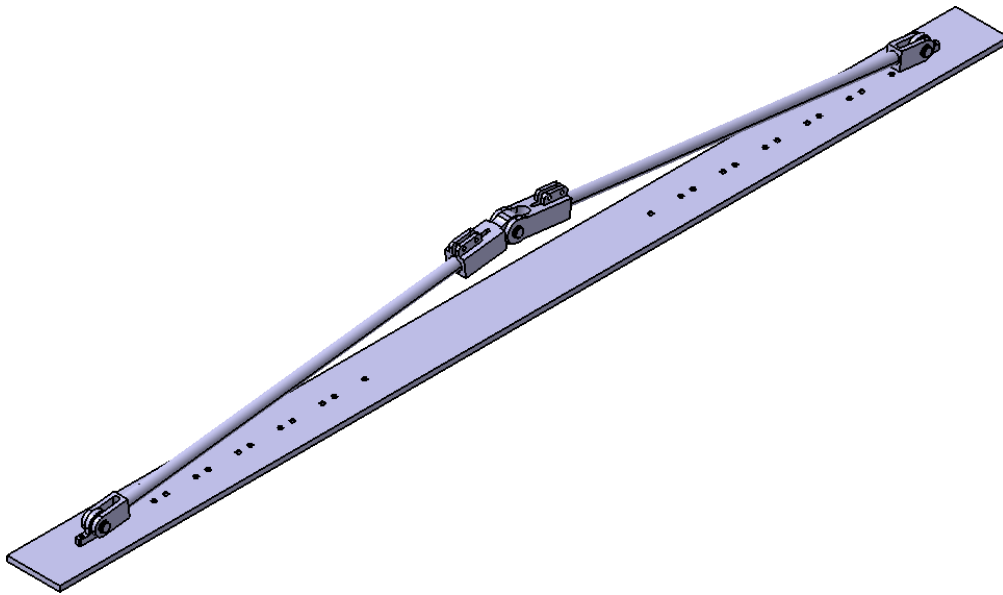


Figure 5.6: Model for the experiments. Courtesy of Mateusz Barys.

is a steel beam, while the inclined beams are circular carbon reinforced polymer tubes. The tubes are attached to the main beam by attaching the bearing in Figure 5.7a to the beam, and the hinge in Figure 5.7b to one end of a tube and connecting the two by a steel pin. The tubes are connected at the top point by the hinge in Figure 5.7c and the bearing in Figure 5.7d, one attached to each tube, joining them by an additional steel pin.

The material and geometrical properties of the main beam and inclined carbon tubes are

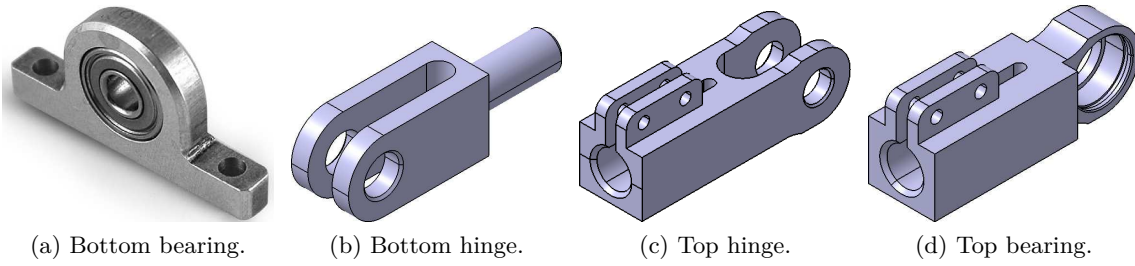


Figure 5.7: Assembly bearings. Courtesy of Mateusz Barys.

given in Table 5.2.

Table 5.2: Material parameters and dimensions of beam parts.

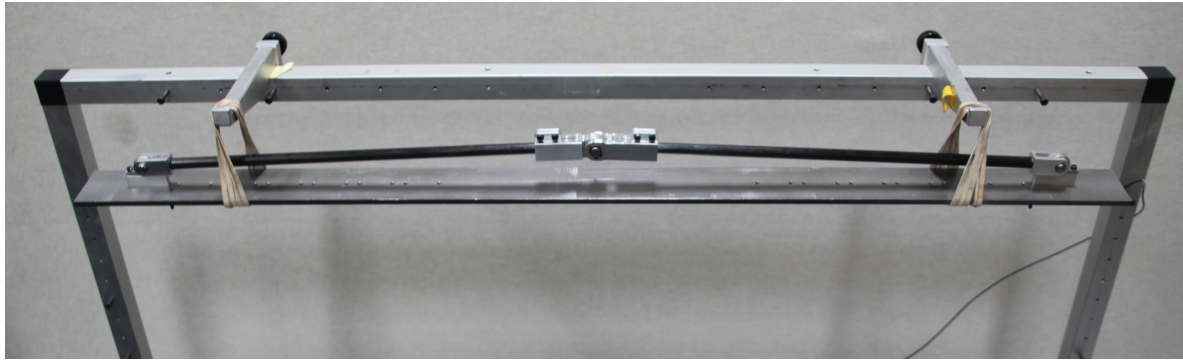
Main beam				
Young's modulus	Density	Length	Width	Height
E [GPa]	ρ [kg/m ³]	l [mm]	b [mm]	h [mm]
210	7880	900	50	5
Carbon tubes				
Young's modulus	Density	Outer radius	Inner radius	
E [GPa]	ρ [kg/m ³]	d_o [mm]	d_i [mm]	
230	1550	5	4	

The lengths of the carbon tubes have been excluded, since this depends on the internal mechanism length, which can be varied in the experiments.

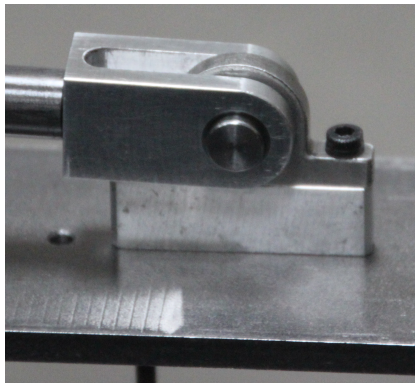
The physical realization of the model in Figure 5.6 is shown in Figure 5.8, with zooms on the attachment and top bearings in Figures 5.8b and 5.8c. The whole system is suspended in rubber bands to simulate free-free boundary conditions and an accelerometer is attached at the right end of the beam to measure the transmission when applying an impact force at the left end by a hammer.

All hardware used for the experiments were Brüel & Kjær equipment. The impact hammer, model 8206, was attached to the data acquisition board, model 3160-A-4/2, through a charge converter, model 2646. The accelerometer, model 4397, was attached to the same data acquisition board, which fed the measurements to the B&K software PULSE, that handled all post-processing of the data.

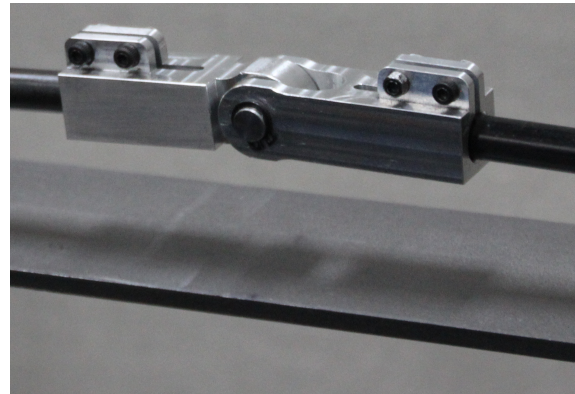
The experimental setup is shown schematically in Figure 5.9, with relevant dimensions indicated. The only dimension not previously given is the bearing support height h_b , allowing for a larger internal moment arm between the attachment point and the beam centerline. For the experiments, two support heights were available, $h_b = 12$ mm and $h_b = 23$ mm. The experimental design allowed for varying additional parameters, the full list is given next to Figure 5.9.



(a) Full view.



(b) Attachment zoom.



(c) Top connection zoom

Figure 5.8: Experimental setup

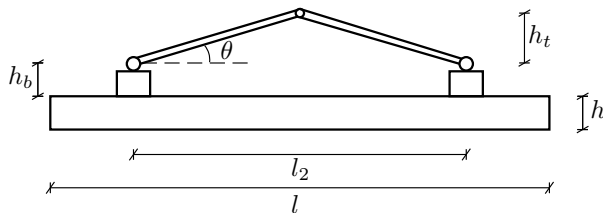


Figure 5.9: Experiment sketch.

Modifiable parameters:

- The internal mechanism length l_2 (also affects added mass).
- The amplification angle θ .
- The height of the bearing support h_b (also affects added mass).

Due to physical limitations, it was not possible to vary each parameter while keeping all other parameters constant, i.e., modifying the internal length affects the amplification angle, while also making the mass contribution lower due to decreased length of the inclined tubes. For completeness, the total added mass range for the two configurations of bearing support height are given in Table 5.3, including the added mass ratio range, $\tilde{\mu}$.

These relations between the design parameters means that it can be difficult to uniquely identify if the change in performance when, e.g., decreasing the internal length, is from the length or mass decrease, however for the present purpose of presenting an experimental demonstration of the effect of the designed mechanism, the setup is sufficient. The results will be illustrated by experimentally obtained frequency response functions (FRFs) of the output

Table 5.3: Added mass from mechanism

	Attachment mass	Top mass	Carbon tubes	Total	Mass ratio
$h_b = 12$ mm	50.0 g	70.6 g	9.4 - 32.5 g	130.0 - 153.1 g	7.3 - 8.6 %
$h_b = 23$ mm	59.6 g	70.6 g	9.4 - 32.5 g	139.6 - 162.7 g	7.9 - 9.2 %

acceleration amplitude, \ddot{A}_{end} , normalized by the input force amplitude, F_{in} .

Figure 5.10 illustrates FRFs for two specific sets of parameters. For comparison, the figure also includes the experimental results of the homogeneous beam.

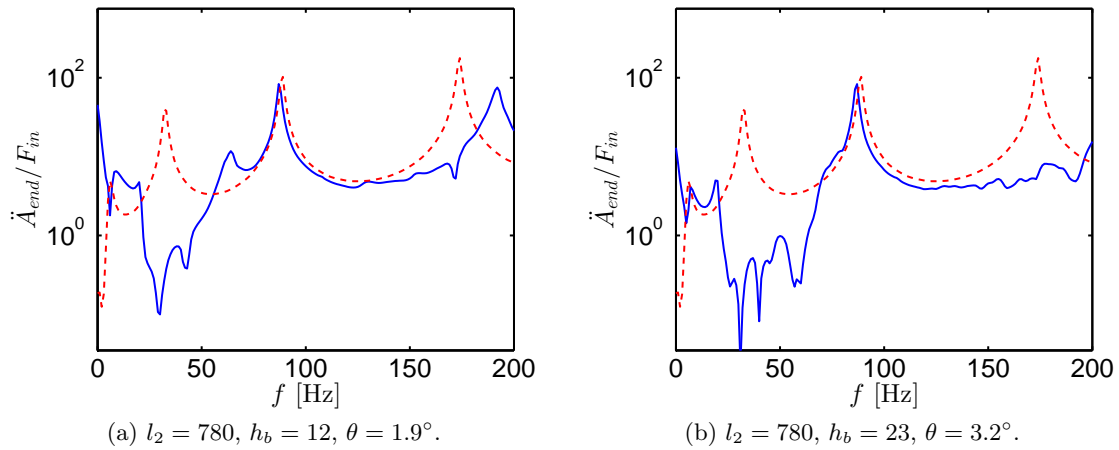


Figure 5.10: Experimental FRFs for homogeneous (red dashed) and hybrid system (blue solid).

The FRFs for the hybrid system clearly illustrate an effect of attaching the mechanism to the beam. Furthermore, for the chosen set of parameters, a relatively wide band of vibration attenuation is observed around the first resonance frequency of the homogeneous beam, in particular for the second case with the larger base height and amplification angle. It was expected that an increase in bearing support height would improve the effect of the mechanism, however the simultaneous increase in amplification angle was expected to decrease the effect. For these particular parameter combinations, the net effect is seen to be positive.

Internal distance variation

As previously mentioned, the physical design does not allow for complete freedom in modifying the design parameters independently of each other, however, as long as this constraint of reality is kept in mind, some qualitative effects can still be observed. The experimental setup allows for seven different configurations of the internal length parameter, l_2 , as long as the attachment is to be symmetrically applied. When decreasing this distance, keeping the base height h_b and the mechanism height h_t constant, the amplification angle changes as well. It is expected that the decrease in l_2 and increase in θ both negatively impacts the performance of the mechanism. To illustrate the effect of decreasing the internal length, Figure 5.11 illustrates the experimentally obtained FRFs for two different l_2 -values, where the height h_t

is kept constant, thus varying θ in Figure 5.11a, while the amplification angle is kept as close as possible for the two experiments in Figure 5.11b.

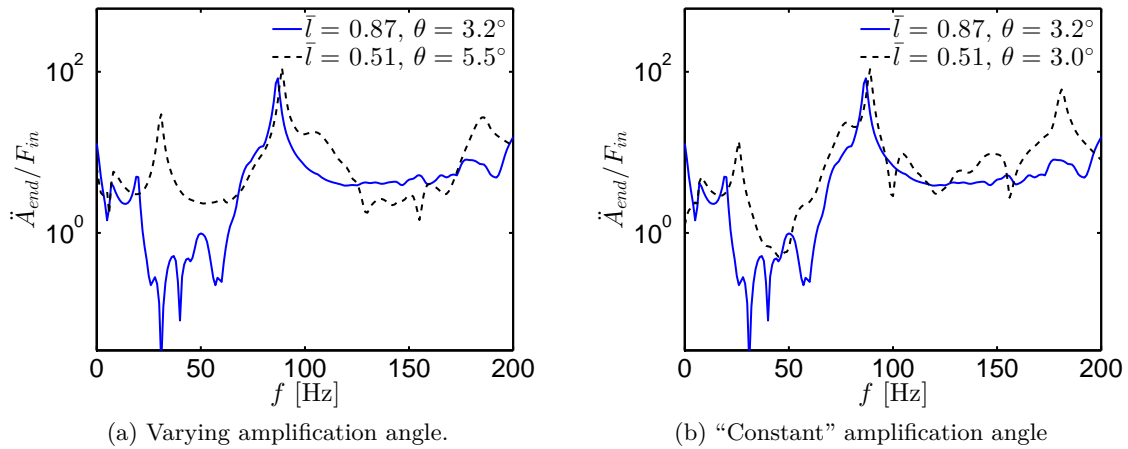


Figure 5.11: Experimental FRFs varying internal distance. $h_b = 23$ mm.

In both cases, the performance in terms of low-frequency filtering properties, is seen to decrease. The filtering properties of the case where the amplification angle is *not* held constant however (Figure 5.11a), is seen to deteriorate more than the case where it is held constant (Figure 5.11b). To retain as large a degree of comparability between the experimental data as possible, the case where the amplification angle is attempted to be held constant is chosen to illustrate the effect of decreasing the internal length. Figure 5.12 shows a zoom of the experimentally obtained FRFs for decreasing the internal length as well as the reference FRF for the homogeneous beam.

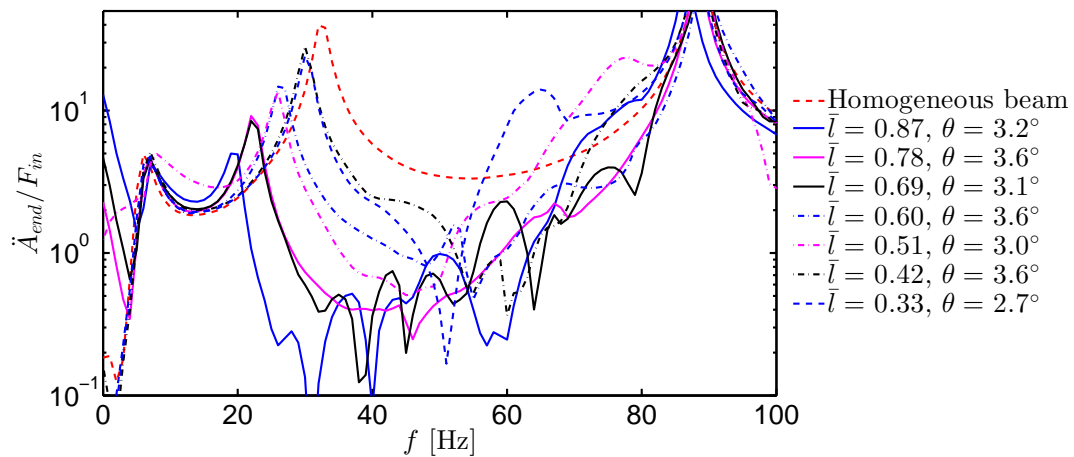


Figure 5.12: Effect of internal length variation.

The figure illustrates, similar to Figure 5.11, that decreasing the internal length decreases the filtering properties of the hybrid system. The FRFs are furthermore noted to approach that of the homogeneous beam as the internal length ratio (and thus also the added mass ratio) is decreased.

5.2 Nonlinear kinematics

The inertial amplification mechanism described in Chapter 4 and [P2] is directly constructed to generate a large vertical displacement $z_2(t)$ due to the geometric layout. By geometric considerations, the horizontal displacement $z_1(t)$ is obtained as the mean of the displacement at the two attachment points, while the vertical displacement is governed by the quadratic equation:

$$z_2(t)^2 + l_2 \tan \theta z_2(t) + \frac{l_2^2}{4} \left(\left(\frac{y_2(t) - y_1(t)}{l_2} \right)^2 - 2 \frac{y_2(t) - y_1(t)}{l_2} \right) = 0, \quad y_i(t) = u(x_i, t), \quad (5.5)$$

where x_1 and x_2 are the attachment coordinates and $l_2 = x_2 - x_1$ is the internal distance of the mechanism. For simplicity the quadratic equation governing the vertical displacement of the amplification mass is linearized in [P2]. The consequences of this linearization is investigated in this section by considering the full nonlinear kinematic expressions, given as:

$$z_1(t) = \frac{1}{2} (y_1(t) + y_2(t)), \quad y_i = u(x_i, t), \quad (5.6a)$$

$$z_2(t) = \frac{1}{2} l_2 \tan \theta \left(-1 + \sqrt{1 - \cot^2 \theta (y_d^2 - 2y_d)} \right), \quad y_d = \frac{y_2 - y_1}{l_2}, \quad (5.6b)$$

where only the physically meaningful root of Eq. (5.5) has been retained. Numerical simulation results for a single unit cell exposed to harmonic loading will be presented, focusing on multiple harmonic generation when applying harmonic loading within the gap. The main concern is whether nonlinearity impairs the performance of the mechanism such that a loading frequency within the gap generates harmonics within or outside of the gap, impeding the filter properties of the mechanism.

5.2.1 Governing equations

Consider the discretized hybrid rod-mechanism system in Figure 5.13, divided into $N - 1$ finite elements with the mechanism attached at the nodes n_1 and n_2 .

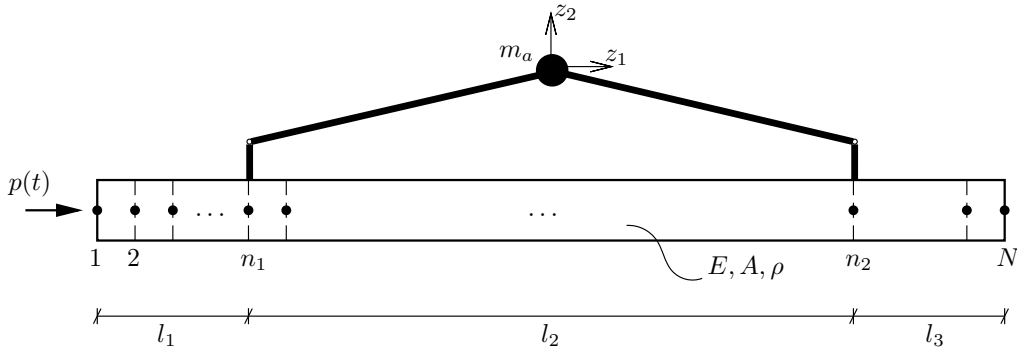


Figure 5.13: Discretized hybrid rod-mechanism system.

The displacement vector $\mathbf{u}(t) = [u_1(t) \ u_2(t) \ \cdots \ u_N(t)]^T$ contains the nodal displacements, while the load vector $\mathbf{p}_{ext}(t) = [p(t) \ 0 \ \cdots \ 0]^T$ contains the external forces.

The governing equations for the system in Figure 5.13 are derived in Appendix B. The resulting equations are:

$$\mathbf{M}^*(\mathbf{u})\ddot{\mathbf{u}} + \mathbf{C}\dot{\mathbf{u}} + \mathbf{K}\mathbf{u} + \mathbf{p}_I(\mathbf{u}, \dot{\mathbf{u}}) = \mathbf{p}_{ext}, \quad (5.7)$$

where $\mathbf{M}^*(\mathbf{u})$ is the state-dependent mass matrix and $\mathbf{p}_I(\mathbf{u}, \dot{\mathbf{u}})$ is the nonlinear internal force vector arising from the applied mechanism. The damping matrix, \mathbf{C} , is an added viscous damping matrix ensuring that each linear mode of the hybrid system has a damping ratio of $\zeta_k = 0.005$, included to kill transients in the response. The governing equations are numerically integrated in MATLAB after being recast to first order form. Introducing the state vector $\mathbf{y} = [\mathbf{u}^T \ \dot{\mathbf{u}}^T]^T$, the governing equations can be written as

$$\widetilde{\mathbf{M}}(\mathbf{y})\dot{\mathbf{y}} = \mathbf{A}\mathbf{y} + \widetilde{\mathbf{p}}_{ext} + \widetilde{\mathbf{p}}_I(\mathbf{y}), \quad (5.8)$$

where the augmented system matrices and force vectors are given as

$$\begin{aligned} \widetilde{\mathbf{M}}(\mathbf{y}) &= \begin{bmatrix} \mathbf{I} & \mathbf{0} \\ \mathbf{0} & \mathbf{M}^*(\mathbf{y}) \end{bmatrix}, \quad \mathbf{A} = \begin{bmatrix} \mathbf{0} & \mathbf{I} \\ -\mathbf{K} & -\mathbf{C} \end{bmatrix}, \\ \widetilde{\mathbf{p}}_{ext} &= \begin{bmatrix} \mathbf{0} \\ \mathbf{p}_{ext} \end{bmatrix}, \quad \widetilde{\mathbf{p}}_I(\mathbf{y}) = \begin{bmatrix} \mathbf{0} \\ -\mathbf{p}_I(\mathbf{y}) \end{bmatrix}. \end{aligned} \quad (5.9)$$

5.2.2 Numerical experimental setup

The discretized system in Figure 5.13 is used for a series of numerical experiments, integrating the governing equations in the state space format in Eq. (5.8) for various loading amplitudes and frequencies. The physical parameters for the experiments are given in Table 5.4.

Table 5.4: Physical parameters for the numerical experiments.

E	ρ	A	l_1	l_2	l_3	$m_a/(\rho Al)$	θ
[GPa]	[kg/m ³]	[m ²]	[m]	[m]	[m]	[-]	[rad]
69.8	2700	$6.25 \cdot 10^{-4}$	$2.75 \cdot 10^{-2}$	$49.50 \cdot 10^{-2}$	$2.75 \cdot 10^{-2}$	0.10	$\pi/18$

Each domain of the host rod is divided into a number of elements, denoted \mathcal{N}_1^e , \mathcal{N}_2^e and \mathcal{N}_3^e respectively. The mechanism is applied at the nodes n_1 and n_2 whereby the mass matrix contributions enter at these positions and the nonlinear force vector has non-zero contributions at these positions alone. To avoid shock formations from the load application, the load is ramped from zero to its full value according to

$$p(t) = p_0 \left(1 - e^{-\zeta t}\right) \sin \Omega t. \quad (5.10)$$

The ramping exponent is determined such that the ramping factor $(1 - e^{-\zeta t})$ is equal to 0.99 after 5 loading periods. The integration time for each experiment is chosen as 5500

loading periods, to ensure that transients have passed. The numerical parameters related to the simulations are summarized in Table 5.5. The time-step is not included since the ODE45-solver in MATLAB adjusts this according to the prescribed relative tolerance, ϵ .

Table 5.5: Numerical parameters for the experiments.

\mathcal{N}_1^e	\mathcal{N}_2^e	\mathcal{N}_3^e	ζ_l	ζ_k	T_{sim}	ϵ
3	30	3	$-\frac{\ln(0.01)\Omega}{10\pi}$	0.005	$5500\frac{2\pi}{\Omega}$	10^{-10}

The acceleration signals are obtained by numerically differentiating the velocity signals.

5.2.3 Simulation results

The numerical experiments are carried out for three different loading frequencies, Ω_1 , Ω_2 and Ω_3 given in Table 5.6, where ω_{ai} denotes the i^{th} antiresonance frequency.

Table 5.6: Loading frequencies.

Ω_1	Ω_2	Ω_3
ω_{a1}	$\frac{1}{2}(\omega_{a1} + \omega_{a2})$	ω_{a2}

The three loading frequencies are all positioned within the first band gap of the corresponding infinite, linear hybrid material. They are chosen to investigate the sensitivity of a linear filter design, placing the loading frequency within the band gap.

Figure 5.14 illustrates the spectral content of the acceleration signal at the end of the hybrid system for the three different loading frequencies, at the normalized forcing level $p_0/(EA) = 3.5 \cdot 10^{-4}$. The spectral content is obtained by a Fourier transform of the temporal acceleration signal exposed to a scaled Hann-window, preserving amplitude information between the time and frequency domain. The figure also includes the frequency response functions for the corresponding homogeneous rod and linearized hybrid system for comparison.

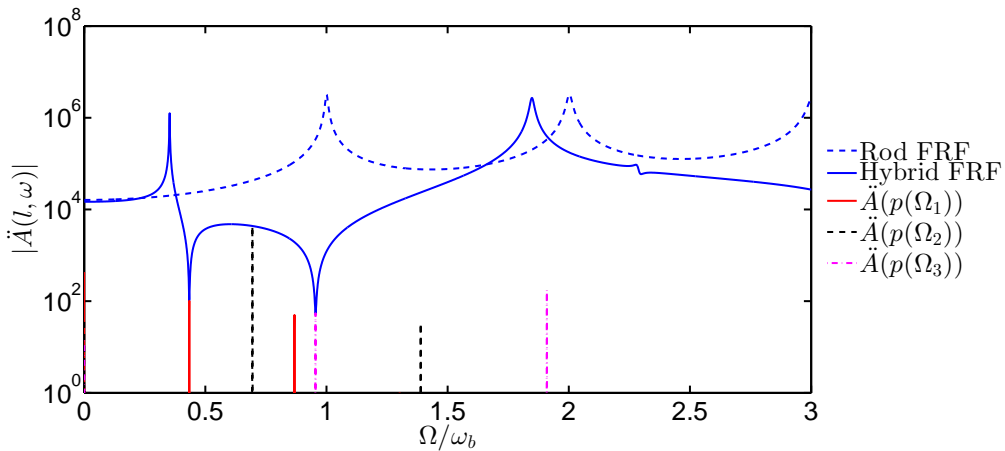


Figure 5.14: Frequency content for $p_0/(EA) = 3.5 \cdot 10^{-4}$.

The amplitudes of the fundamental harmonics agree well with the linear predictions for the illustrated load amplitude. For each loading frequency, a higher harmonic component is detected at 2Ω , consistent with the quadratic approximation of the nonlinearity obtained when Taylor-expanding the displacement z_2 to second order. Additional higher harmonic components are detected outside of the illustrated amplitude interval. The magnitude of the higher harmonic generation is seen to differ between the loading frequencies. In particular, it appears that when the higher harmonic frequency falls outside of the band gap, its amplitude actually surpasses the fundamental amplitude. Conversely, the higher harmonics falling within the band gap, as observed for the first two loading frequencies, appears to have lower amplitudes than the fundamental. This trend could indicate that a design ensuring that the loading frequency was within the band gap should also ensure that the second harmonic was within the gap, to preserve the performance of the inertial amplification mechanism. This is further illustrated in Figure 5.15, where the normalized acceleration amplitude of the fundamental and higher harmonic is illustrated as a function of normalized load amplitude for the three loading frequencies in a log-log scale.

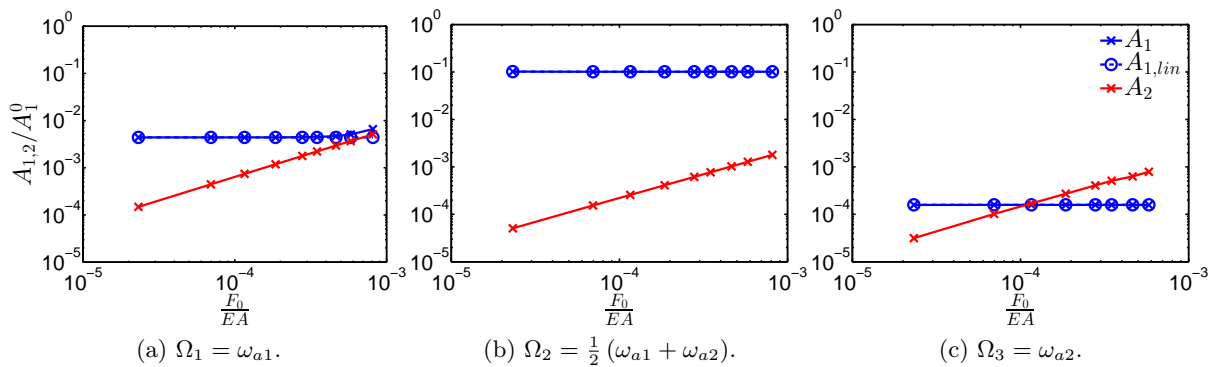


Figure 5.15: Acceleration amplitudes. Blue crosses: Fundamental harmonic amplitudes from simulations. Blue circles: Linear amplitude predictions. Red crosses: Second harmonic amplitudes from simulations.

All acceleration amplitudes have been normalized by the acceleration amplitude, A_1^0 , for the corresponding homogeneous rod at the applied load amplitude and frequency. The higher harmonic amplitude is seen to increase with load amplitude, increasing beyond the fundamental harmonic amplitude when loading is sufficient. This occurs for both Ω_1 and Ω_3 , however the threshold is significantly lower for Ω_3 , as expected from the illustrated FRFs in Figure 5.14. Furthermore, for the investigated load range, the fundamental amplitude is very well predicted by the linearized model. The level of the higher harmonic acceleration amplitude is seen to stay below approximately one percent of the acceleration amplitude of the corresponding homogeneous system for the investigated loading range. Hence, even though the higher harmonic amplitude increases beyond the fundamental amplitude for Ω_3 , the mechanism still attenuates vibrations compared to *not* using it.

The broad-band effect found for the linearized hybrid system in [P2] appears to be intact when including the nonlinearity introduced by the geometric layout of the inertial ampli-

cation mechanism, in particular if the second harmonic is kept within the band gap. The investigation has been focused towards the potential hazard of higher harmonic generation, rather than the issue of frequency/amplitude dependence. The blue curves for the fundamental harmonic in Figure 5.15 however, illustrate that the fundamental amplitudes from the nonlinear simulations follow the linear predictions nicely, indicating that this effect is not very pronounced from the nonlinearity introduced by the mechanism. The investigation for the tuned mass damper in Viguié & Kerschen (2009) shows that the frequency tuning suffers from nonlinearity of the *host-structure*, an effect which has not been investigated here. It is noted however, that the broad-band effect of the presented mechanism could indicate that it is less sensitive to frequency/amplitude effects, warranting additional investigations.

Chapter 6

Concluding remarks

The dynamic characteristics of advanced linear and nonlinear periodic material systems are analyzed to explore the potential for creating novel materials with improved properties. The improved material properties pursued in this thesis are energy conversion between wave-modes due to nonlinear modal interaction, [P1], and broadband wave/vibration attenuation induced by applying a mechanism, designed for amplifying the inertial forces in the system, on the surface of the material, [P2]. The applied “surface treatment” is investigated further in Chapter 5, where some of the idealizing assumptions of the original model, such as rigid connections and linearized kinematics, are relaxed. Section 5.1.2 further presents experimental results for a beam with the mechanism applied, illustrating that the design from [P2] works for attenuating flexural vibrations as well. The experimental results are part of an M.Sc.-project carried out by Mr. Mateusz Barys, supervised by Professor Jakob Søndergaard Jensen and myself. Hence, all credit for the results goes to Mr. Barys, they are included in the present thesis to underline the fact that the mechanism designed in [P2] has practical applications in terms of broadband vibration suppression.

6.1 Modal interaction and energy conversion in nonlinear, periodic materials

The wave characteristics of the nonlinear periodic material in [P1] is shown to be affected by nonlinear self-interaction, increasing the dispersion shift in the band structure when multiple modes are present, due to the increased energy from the additional modes. The importance of this effect is expected to increase with increased modelling accuracy, since the number of supported wave-modes of the material increases. For a continuous material, an infinite number of modes can interact, whereby the distribution of energy between modes affects the band structure of the material. Depending on the nonlinear coupling between modes and the controllability of wave-amplitudes, this might be utilized to tailor the band structure by exciting specific modes.

Furthermore, the generation of higher harmonics from an acoustic wave travelling through the material is investigated, analytically and numerically, revealing a limited potential for energy conversion through the generation of additional harmonics. As the wave-amplitude

increases, the analytical, asymptotic model breaks down and numerical simulations demonstrate that the notion of discrete frequency components deteriorate as the energy from both the fundamental and higher harmonic waves is distributed over a wider frequency spectrum. Hence, the possibility of designing the material to maximize the higher harmonic generation appears to be limited.

6.2 Low-frequency and broadband wave attenuation by inertial amplification

The mechanism designed in [P2] is applied as a surface treatment to a homogeneous rod, which opens up a number of gaps in the band structure, in particular a wide and deep gap can be generated in the low-frequency range. It is demonstrated that a comparably large effect, in terms of gap width and -depth, can be obtained from a low added mass due to its amplification through levers. Since the gap depth is directly proportional to the attenuation strength and thus, the damping efficiency of the system, the hybrid material is a solid choice for broadband sound and vibration isolation purposes. This is further supported by the numerical and experimental results of Chapter 5, demonstrating that:

1. The idealization of [P2] are not so severe that the inertial amplification effect cannot occur in realistic systems.
2. The inherent nonlinearity arising from the geometric layout of the mechanism does not invalidate the general efficacy of the design.
3. The mechanism, originally made for longitudinal wave attenuation, works for attenuating flexural vibrations as well.

Hence, utilizing inertial amplification for creating novel materials with strong wave-attenuation characteristics, or directly designing inerter-based systems for damping of flexible structures, appears to have great future potential.

6.3 Future work

Chapter 5 describes a number of extensions to the inertial amplification model from [P2], all aimed towards a practical realization of the system. A natural next step in the research is, in the author's opinion, to look more thoroughly into the experimental investigation of the inertial amplification concept. The results presented in Section 5.1.2 (and the underlying master project) is an adequate starting point from which to begin the research. The experimental investigation should be combined with an accurate mathematical model, whereby the system characteristics can be predicted analytically and possibly optimized for improved performance by, e.g., topology optimization. Along the lines of optimization, it might be of interest to explore different designs for generating the amplified inertia than the one presented in [P2]. Furthermore, an accurate, robust and preferably relatively simple mathematical description

of the mechanism for transverse vibrations will greatly alleviate its introduction in industrial applications, which could benefit immensely from the broadband vibration suppression exhibited by the system.

References

- Acar, G. & Yilmaz, C. (2013), ‘Experimental and numerical evidence for the existence of wide and deep phononic gaps induced by inertial amplification in two-dimensional solid structures’, *Journal of Sound and Vibration* **332**(24), 6389–6404.
- Bloch, F. (1929), ‘Über die quantenmechanik der elektronen in kristalgittern’, *Zeitschrift Für Physik* **52**, 555–600.
- Brillouin, L. (1953), *Wave Propagation in Periodic Structures*, Dover Publications.
- Cabaret, J., Tournat, V. & Béquin, P. (2012), ‘Amplitude-dependent phononic processes in a diatomic granular chain in the weakly nonlinear regime’, *Physical Review E* **86**(4), 041305.
- Chen, M. Z. Q., Papageorgiou, C., Scheibe, F., Wang, F. C. & Smith, M. (2009), ‘The missing mechanical circuit element’, *IEEE Circuits and Systems Magazine* **9**, 10–26.
- Daraio, C., Nesterenko, V. F., Herbold, E. B. & Jin, S. (2006), ‘Tunability of solitary wave properties in one-dimensional strongly nonlinear phononic crystals’, *Physical Review E - Statistical, Nonlinear, and Soft Matter Physics* **73**(2), 1–10.
- Dou, S. & Jensen, J. S. (2015), ‘Optimization of nonlinear structural resonance using the incremental harmonic balance method’, *Journal of Sound and Vibration* **334**, 239–254.
- Dou, S. & Jensen, J. S. (2016), ‘Optimization of hardening/softening behavior of plane frame structures using nonlinear normal modes’, *Computers & Structures* **164**, 63–74.
- Elachi, C. (1976), ‘Waves in active and passive periodic structures: a review’, *Proceedings of the IEEE* **64**, 1666–1698.
- Flannelly, G. W. (1967), ‘Dynamic antiresonant vibration isolator’. US Patent 3,322,379.
- Floquet, G. (1883), ‘Sur les Équations Différentielles Linéaires a. Coefficients Périodiques’, *Annales de l’École Normale Supérieure* **12**, 47–88.
- Frahm, H. (1911), ‘Device for damping vibration of bodies’. U.S. Patent 989,958.
- Ganesh, R. & Gonella, S. (2015), ‘From Modal Mixing to Tunable Functional Switches in Nonlinear Phononic Crystals’, *Physical Review Letters* **114**(5), 1–5.

- Hladky-Hennion, A. C., Allan, G. & De Billy, M. (2005), ‘Localized modes in a one-dimensional diatomic chain of coupled spheres’, *Journal of Applied Physics* **98**(5).
- Hu, Y., Chen, M. Z., Shu, Z. & Huang, L. (2015), ‘Analysis and optimisation for inerter-based isolators via fixed-point theory and algebraic solution’, *Journal of Sound and Vibration* pp. 1–20.
- Hussein, M. I., Hulbert, G. M. & Scott, R. a. (2006), ‘Dispersive elastodynamics of 1D banded materials and structures: analysis’, *Journal of Sound and Vibration* **289**(4-5), 779–806.
- Hussein, M. I., Leamy, M. J. & Ruzzene, M. (2014), ‘Dynamics of Phononic Materials and Structures: Historical Origins, Recent Progress, and Future Outlook’, *Applied Mechanics Reviews* **66**(4), 040802.
- Inman, D. J. (2009), *Engineering Vibrations*, third edn, Pearson Education, Inc. International Edition.
- Krenk, S. & Høgsberg, J. (2016), ‘Tuned resonant mass or inerter-based absorbers : unified calibration with quasi-dynamic flexibility and inertia correction’.
- Liu, L. & Hussein, M. I. (2012), ‘Wave Motion in Periodic Flexural Beams and Characterization of the Transition Between Bragg Scattering and Local Resonance’, *Journal of Applied Mechanics* **79**(1), 011003.
- Liu, Z., Zhang, X., Mao, Y., Zhu, Y. Y., Yang, Z., Chan, C. T. & Sheng, P. (2000), ‘Locally resonant sonic materials’, *Science* **289**, 1734–1736.
- Manktelow, K. L., Leamy, M. J. & Ruzzene, M. (2011), ‘Multiple scales analysis of wave-wave interactions in a cubically nonlinear monoatomic chain’, *Nonlinear Dynamics* **63**(1-2), 193–203.
- Manktelow, K. L., Leamy, M. J. & Ruzzene, M. (2014a), ‘Analysis and experimental estimation of nonlinear dispersion in a periodic string’, *Journal of Vibration and Acoustics* **136**(June), 031016.
- Manktelow, K. L., Leamy, M. J. & Ruzzene, M. (2014b), ‘Weakly nonlinear wave interactions in multi-degree of freedom periodic structures’, *Wave Motion* .
- Mead, D. (1975), ‘Wave propagation and natural modes in periodic systems: I. Mono-coupled systems’, *Journal of Sound and Vibration* **40**(1), 1–18.
- Mead, D. (1996), ‘Wave propagation in continuous periodic structures: Research contributions from southampton, 1964-1995’, *Journal of Sound and Vibration* **190**(3), 495–524.
- Mukherjee, S. & Lee, E. H. (1975), ‘Dispersion Relations and Mode Shapes for Waves in Laminated Viscoelastic Composites by Finite Difference Methods’, *Computers & Structures* **5**, 279–285.

- Narisetti, R. K., Ruzzene, M. & Leamy, M. J. (2011), ‘A perturbation approach for analyzing dispersion and group velocities in two-dimensional nonlinear periodic lattices’, *Transactions of the ASME, Journal of Vibration and Acoustics* **133**, 1–12.
- Nayfeh, A. H. (1981), *Introduction to Perturbation Techniques*, John Wiley and Sons.
- Noël, J. P., Renson, L. & Kerschen, G. (2014), ‘Complex dynamics of a nonlinear aerospace structure: Experimental identification and modal interactions’, *Journal of Sound and Vibration* **333**(12), 2588–2607.
- Papageorgiou, C., Houghton, N. E. & Smith, M. C. (2009), ‘Experimental Testing and Analysis of Inerter Devices’, *Journal of Dynamic Systems, Measurement, and Control* **131**(January 2009), 011001.
- Papageorgiou, C. & Smith, M. C. (2005), ‘Laboratory experimental testing of inerters’, *Proceedings of the 44th IEEE Conference on Decision and Control, and the European Control Conference, CDC-ECC '05 2005*, 3351–3356.
- Qalandar, K. R., Strachan, B. S., Gibson, B., Sharma, M., Ma, A., Shaw, S. W. & Turner, K. L. (2014), ‘Frequency division using a micromechanical resonance cascade’, *Applied Physics Letters* **105**(24).
- Raghavan, L. & Phani, a. S. (2013), ‘Local resonance bandgaps in periodic media: theory and experiment.’, *The Journal of the Acoustical Society of America* **134**(3), 1950–9.
- Sánchez-Morcillo, V. J., Pérez-Arjona, I., Romero-García, V., Tournat, V. & Gusev, V. E. (2013), ‘Second-harmonic generation for dispersive elastic waves in a discrete granular chain’, *Physical Review E - Statistical, Nonlinear, and Soft Matter Physics* **88**(4), 1–8.
- Smith, M. C. (2002), ‘Synthesis of mechanical networks: The inerter’, *IEEE Transactions on Automatic Control* **47**(10), 1648–1662.
- Taniker, S. & Yilmaz, C. (2013), ‘Phononic gaps induced by inertial amplification in BCC and FCC lattices’, *Physics Letters, Section A: General, Atomic and Solid State Physics* **377**, 1930–1936.
- Thomsen, J. J. (2003), *Vibrations and Stability: Advanced theory, Analysis and tools*, Springer.
- Viguié, R. & Kerschen, G. (2009), ‘Nonlinear vibration absorber coupled to a nonlinear primary system: A tuning methodology’, *Journal of Sound and Vibration* **326**(3-5), 780–793.
- Yilmaz, C. & Hulbert, G. M. (2010), ‘Theory of phononic gaps induced by inertial amplification in finite structures’, *Physics Letters, Section A: General, Atomic and Solid State Physics* **374**(34), 3576–3584.
- Yilmaz, C., Hulbert, G. M. & Kikuchi, N. (2007), ‘Phononic band gaps induced by inertial amplification in periodic media’, *Physical Review B - Condensed Matter and Materials Physics* **76**(April).

- Yilmaz, C. & Kikuchi, N. (2006), ‘Analysis and design of passive low-pass filter-type vibration isolators considering stiffness and mass limitations’, *Journal of Sound and Vibration* **293**, 171–195.
- Yousefzadeh, B. & Phani, A. S. (2015), ‘Energy transmission in finite dissipative nonlinear periodic structures from excitation within a stop band’, *Journal of Sound and Vibration* **354**, 180–195.
- Yuksel, O. & Yilmaz, C. (2015), ‘Shape optimization of phononic band gap structures incorporating inertial amplification mechanisms’, *Journal of Sound and Vibration* **355**, 232–245.

Appendix A

Modal expansion

This appendix presents the derivation of the modal matrices used for determining the band-gap limits of the inertial amplification system in Section 4.4. Consider the linearized equations of motion for the longitudinal displacement of the rod/mechanism system:

$$c_0^2 u''(x, t) = \ddot{u}(x, t) + \frac{\mu}{4} \left[(\ddot{u}(x_1, t) + \ddot{u}(x_2, t)) (\delta(x - x_1) + \delta(x - x_2)) + \cot^2 \theta (\ddot{u}(x_2, t) - \ddot{u}(x_1, t)) (\delta(x - x_2) - \delta(x - x_1)) \right], \quad (\text{A.1})$$

where $c_0 = \sqrt{E/\rho}$ is the longitudinal wave speed, $\mu = m_a/(\rho Al)$ is the added mass ratio, x_1 and x_2 are the attachment points, θ is the amplification angle and $\delta(x - x_i)$ is the Dirac's delta function. The solution is expressed as:

$$u(x, t) = \sum_{k=1}^N \varphi_k(x) \xi_k(t), \quad (\text{A.2})$$

where $\varphi_k(x)$ is the undamped, homogeneous mode shapes of the rod, while $\xi_k(t)$ is the modal coordinates containing the temporal variation of mode k and N is the number of modes retained. Inserting the modal expansion in Eq. (A.1) yields:

$$c_0^2 \sum_{k=1}^N \varphi_k''(x) \xi_k(t) = \sum_{k=1}^N \varphi_k(x) \ddot{\xi}_k(t) + \frac{\mu}{4} \left[\sum_{k=1}^N (\varphi_k(x_1) + \varphi_k(x_2)) \ddot{\xi}_k(t) (\delta(x - x_1) + \delta(x - x_2)) + \cot^2 \theta \sum_{k=1}^N (\varphi_k(x_2) - \varphi_k(x_1)) \ddot{\xi}_k(t) (\delta(x - x_2) - \delta(x - x_1)) \right], \quad (\text{A.3})$$

which is multiplied by the mode shapes φ_n and integrated over the length of the rod:

$$\begin{aligned}
c_0^2 \sum_{k=1}^N \int_0^l \varphi_n \varphi_k''(x) dx \xi_k(t) &= \sum_{k=1}^N \int_0^l \varphi_n(x) \varphi_k(x) dx \ddot{\xi}_k(t) \\
&+ \frac{\mu}{4} \left[\sum_{k=1}^N \int_0^l \varphi_n(x) (\varphi_k(x_1) + \varphi_k(x_2)) (\delta(x - x_1) + \delta(x - x_2)) dx \ddot{\xi}_k(t) \right. \\
&\left. + \cot^2 \theta \sum_{k=1}^N \int_0^l \varphi_n(x) (\varphi_k(x_2) - \varphi_k(x_1)) (\delta(x - x_2) - \delta(x - x_1)) dx \ddot{\xi}_k(t) \right]. \tag{A.4}
\end{aligned}$$

Next, it is utilized that, for the mode shapes of an undamped homogeneous, free-free or fixed-fixed rod, the following relations hold:

$$\varphi_k''(x) = -\beta_k^2 \varphi_k(x), \quad \int_0^l \varphi_n(x) \varphi_k(x) dx = \begin{cases} \frac{l}{2} & \text{for } k = n \\ 0 & \text{for } k \neq n \end{cases} \tag{A.5}$$

whereby Eq. (A.4) reduce to:

$$\begin{aligned}
(\beta_n c_0)^2 \xi_n + \ddot{\xi}_n + \frac{\mu}{2l} \left[(\varphi_n(x_1) + \varphi_n(x_2)) \sum_{k=1}^N (\varphi_k(x_1) + \varphi_k(x_2)) \ddot{\xi}_k \right. \\
\left. + \cot^2 \theta (\varphi_n(x_2) - \varphi_n(x_1)) \sum_{k=1}^N (\varphi_k(x_2) - \varphi_k(x_1)) \ddot{\xi}_k \right] = 0. \tag{A.6}
\end{aligned}$$

Hence, the modal equation for mode n is coupled to all other modes through the inertial amplification terms in Eq. (A.6). The modal equations can be written in matrix form by introducing the modal coordinate vector $\boldsymbol{\xi}(t) = [\xi_1(t) \ \xi_2(t) \ \cdots \ \xi_N(t)]^T$:

$$\mathbf{M} \ddot{\boldsymbol{\xi}}(t) + \mathbf{K} \boldsymbol{\xi}(t) = \mathbf{0}, \quad \mathbf{M} = \mathbf{I} + \mathbf{M}_{IA}^s + \cot^2 \theta \mathbf{M}_{IA}^d. \tag{A.7}$$

The mass matrix is a sum of the identity matrix and two matrices related to the inertial amplification mechanism contributions. These matrices are most conveniently expressed by introducing some shorthand notation for the sum and difference terms in the bracket terms in Eq. (A.6):

$$\Phi_j = \varphi_j(x_1) + \varphi_j(x_2), \quad \Psi_j = \varphi_j(x_2) - \varphi_j(x_1), \tag{A.8}$$

whereby the matrices \mathbf{M}_{IA}^s and \mathbf{M}_{IA}^d can be expressed as:

$$\mathbf{M}_{IA}^s = \frac{\mu}{2l} \begin{bmatrix} \Phi_1^2 & \Phi_1\Phi_2 & \Phi_1\Phi_3 & \cdots & \Phi_1\Phi_N \\ \Phi_2\Phi_1 & \Phi_2^2 & \Phi_2\Phi_3 & \cdots & \Phi_2\Phi_N \\ \Phi_3\Phi_1 & \Phi_3\Phi_2 & \Phi_3^2 & \cdots & \Phi_3\Phi_N \\ \vdots & & & \ddots & \\ \Phi_N\Phi_1 & & & & \Phi_N^2 \end{bmatrix} \quad (\text{A.9a})$$

$$\mathbf{M}_{IA}^d = \frac{\mu}{2l} \begin{bmatrix} \Psi_1^2 & \Psi_1\Psi_2 & \Psi_1\Psi_3 & \cdots & \Psi_1\Psi_N \\ \Psi_2\Psi_1 & \Psi_2^2 & \Psi_2\Psi_3 & \cdots & \Psi_2\Psi_N \\ \Psi_3\Psi_1 & \Psi_3\Psi_2 & \Psi_3^2 & \cdots & \Psi_3\Psi_N \\ \vdots & & & \ddots & \\ \Psi_N\Psi_1 & & & & \Psi_N^2 \end{bmatrix}. \quad (\text{A.9b})$$

This concludes the derivation of the discretized modal equations used for gap limit predictions in Section 4.4.

Appendix B

Numerical model for nonlinear inertial amplification

This appendix presents the derivation of the discretized, nonlinear equations of motion for the hybrid system considered in Section 5.2. The nonlinearity arises from the kinematics of the applied mechanism, while the host rod is modelled as a linear elastic rod. The derivation is based on Lagrange's equations, thus it is conceptually fairly basic. The nonlinear kinematic relations however, causes the equations to become rather involved, hence the derivation is presented to alleviate reproducibility, i.e., the interested readers can consult this appendix rather than going through the motion themselves.

B.1 Nonlinear kinematics

The linearized kinematics used in [P2] and presented in Chapter 4 is based on linearization of the exact displacements, $z_1(t)$ and $z_2(t)$, given as:

$$z_1(t) = \frac{1}{2} (y_1(t) + y_2(t)) , \quad y_i = u(x_i, t), \quad (\text{B.1a})$$

$$z_2(t) = \frac{1}{2} l_2 \tan \theta \left(-1 + \sqrt{1 - \cot^2 \theta (y_d^2 - 2y_d)} \right) , \quad y_d = \frac{y_2 - y_1}{l_2}, \quad (\text{B.1b})$$

where x_1 and x_2 are the attachment points of the mechanism on the rod and l_2 is the internal distance between the points, $l_1 = x_2 - x_1$. Only the vertical displacement, $z_2(t)$, is nonlinear. The expression in Eq. B.1b is obtained by solving a quadratic equation in $z_2(t)$, which can be found in the appendix of [P2], and considering only the physically meaningful root. The horizontal and vertical velocities, \dot{z}_1 and \dot{z}_2 , are:

$$\dot{z}_1 = \frac{1}{2} (\dot{y}_1(t) + \dot{y}_2(t)) , \quad (\text{B.2a})$$

$$\dot{z}_2 = \frac{1}{2} \cot \theta (\dot{y}_2 - \dot{y}_1) \frac{1 - y_d}{\sqrt{1 - \cot^2 \theta (y_d^2 - 2y_d)}}. \quad (\text{B.2b})$$

B.2 Nonlinear constraint forces

The effect of the mechanism on the rod is included via the constraint forces at the attachment points. This approach is particular convenient when the host rod is discretized, since the constraint forces are added directly at the degrees of freedom of attachment. Consider the isolated mechanism in Figure B.1.

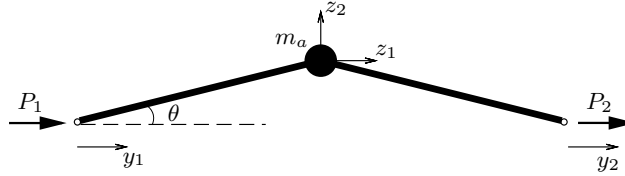


Figure B.1: Mechanism with constraint forces.

The constraint forces, denoted P_1 and P_2 , are determined using Lagrange's equations,

$$\frac{d}{dt} \left(\frac{\partial L}{\partial \dot{y}_i} \right) - \frac{\partial L}{\partial y_i} = \frac{\partial W}{\partial y_i}, \quad (\text{B.3})$$

where $L = T - V$ is the Lagrangian representing the excess of kinetic energy T over potential energy V and $W = P_1 y_1 + P_2 y_2$ is the external work through the generalized displacements. The ideal mechanism has no potential energy associated with motion in terms of y_1 and y_2 . Thus, the Lagrangian consists of kinetic energy alone:

$$L = T = \frac{1}{2} m_a (\dot{z}_1^2 + \dot{z}_2^2) = \frac{1}{2} m_a \left(\frac{1}{4} (\dot{y}_1 + \dot{y}_2)^2 + \frac{1}{4} \cot^2 \theta (\dot{y}_2 - \dot{y}_1)^2 \frac{(1 - y_d)^2}{1 - \cot^2 \theta (y_d^2 - 2y_d)} \right). \quad (\text{B.4})$$

For typographical reasons, two auxiliary functions, h_1 and h_2 are introduced:

$$h_1 = 1 - y_d, \quad (\text{B.5a})$$

$$h_2 = 1 - \cot^2 \theta (y_d^2 - 2y_d). \quad (\text{B.5b})$$

Inserting in Lagrange's equation, Eq. (B.3), for the coordinate y_1 yields:

$$\frac{d}{dt} \left[\frac{m_a}{2} \left(\frac{1}{2} (\dot{y}_1 + \dot{y}_2) + \frac{\cot^2 \theta}{2} (\dot{y}_1 - \dot{y}_2) \frac{h_1^2}{h_2} \right) \right] - \frac{m_a \cot^2 \theta}{4} (\dot{y}_1 - \dot{y}_2)^2 \frac{h_1}{h_2} \left(1 + \cot^2 \theta \frac{h_1^2}{h_2} \right) = P_1, \quad (\text{B.6})$$

in which one should keep in mind that the auxiliary functions, h_1 and h_2 are implicit functions of time as well. Carrying out the differentiation wrt. time for the square brackets yields

$$P_1 = \frac{m_a}{4} \left\{ \ddot{y}_1 + \ddot{y}_2 + \cot^2 \theta \left[(\ddot{y}_1 - \ddot{y}_2) \frac{h_1^2}{h_2} + \frac{2}{l_2} (\dot{y}_1 - \dot{y}_2)^2 \frac{h_1}{h_2} \left(1 + \cot^2 \theta \frac{h_1^2}{h_2} \right) \right] - \frac{m_a \cot^2 \theta}{4 l_2} (\dot{y}_1 - \dot{y}_2)^2 \frac{h_1}{h_2} \left(1 + \cot^2 \theta \frac{h_1^2}{h_2} \right) \right\} \Rightarrow \quad (\text{B.7})$$

$$P_1 = \frac{m_a}{4} \left\{ \ddot{y}_1 + \ddot{y}_2 + \cot^2 \theta (\ddot{y}_1 - \ddot{y}_2) \frac{h_1^2}{h_2} + \frac{\cot^2 \theta}{l_2} (\dot{y}_1 - \dot{y}_2)^2 \frac{h_1}{h_2} \left(1 + \cot^2 \theta \frac{h_1^2}{h_2} \right) \right\}.$$

The same procedure for the y_2 -coordinate yields:

$$P_2 = \frac{m_a}{4} \left\{ \ddot{y}_1 + \ddot{y}_2 + \cot^2 \theta (\ddot{y}_2 - \ddot{y}_1) \frac{h_1^2}{h_2} + \frac{\cot^2 \theta}{l_2} (\dot{y}_2 - \dot{y}_1)^2 \frac{h_1}{h_2} \left(1 + \cot^2 \theta \frac{h_1^2}{h_2} \right) \right\}. \quad (\text{B.8})$$

B.2.1 Approximation

For illustrative purposes, the approximated nonlinear constraint forces for small y_d values, i.e., the case where the difference in displacement is much smaller than the internal distance $(y_2 - y_1) \ll l_2$ is presented. This is done by expanding the functional factors h_1^2/h_1 and h_1/h_2 .

$$\left. \frac{h_1^2}{h_2} \right|_{y_d=0} = 1 - \frac{2}{\sin^2 \theta} y_d + \frac{1 + 4 \cot^2 \theta}{\sin^2 \theta} y_d^2 + O(y_d^3) \approx 1 - 2\gamma_2 y_d + \gamma_3 y_d^2, \quad (\text{B.9a})$$

$$\left. \frac{h_1}{h_2} \right|_{y_d=0} = \frac{1}{\sin^2 \theta} - \frac{1 + 4 \cot^2 \theta}{\sin^2 \theta} y_d + O(y_d^2) \approx \gamma_2 + \gamma_3 y_d, \quad (\text{B.9b})$$

whereby the linearized constraint forces are:

$$P_{1,lin} = \frac{m_a}{4} \left(\ddot{y}_1 + \ddot{y}_2 + \cot^2 \theta (\ddot{y}_1 - \ddot{y}_2) \right), \quad (\text{B.10a})$$

$$P_{2,lin} = \frac{m_a}{4} \left(\ddot{y}_1 + \ddot{y}_2 + \cot^2 \theta (\ddot{y}_2 - \ddot{y}_1) \right), \quad (\text{B.10b})$$

as obtained in [P2]. The nonlinear constraint forces approximated to cubic order are:

$$P_{1,c} = \frac{m_a}{4} \left\{ \ddot{y}_1 + \ddot{y}_2 + \cot^2 \theta (\ddot{y}_1 - \ddot{y}_2) \left(1 - 2\gamma_2 y_d + \gamma_3 y_d^2 \right) + \frac{\cot^2 \theta}{l_2} (\dot{y}_1 - \dot{y}_2)^2 (\gamma_2 - \gamma_3 y_d) \right\}, \quad (\text{B.11a})$$

$$P_{2,c} = \frac{m_a}{4} \left\{ \ddot{y}_1 + \ddot{y}_2 + \cot^2 \theta (\ddot{y}_2 - \ddot{y}_1) \left(1 - 2\gamma_2 y_d + \gamma_3 y_d^2 \right) + \frac{\cot^2 \theta}{l_2} (\dot{y}_1 - \dot{y}_2)^2 (\gamma_2 - \gamma_3 y_d) \right\}, \quad (\text{B.11b})$$

illustrating that the mechanism introduce nonlinear coupling between displacement and acceleration as well as between velocity and acceleration. The full nonlinear constraint forces in Eqs. (B.7) and (B.8) will be included in a discretized model. The inertial-displacement nonlinearity will be included via a state-dependent mass matrix, while the nonlinear velocity term will be included by a nonlinear force vector on the right hand side of the governing equations.

B.3 Discretized hybrid system

Consider the schematic of the discretized rod in Figure B.2.

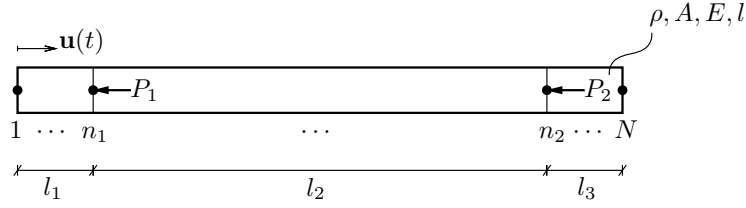


Figure B.2: Three-domain elastic rod with constraint forces.

The rod is discretized by $N - 1$ linear finite elements and the constraint forces are applied at the nodes n_1 and n_2 . The discretized equations of motion are given as:

$$\mathbf{M}\ddot{\mathbf{u}} + \mathbf{K}\mathbf{u} = \mathbf{p}_{ext} - \mathbf{w}_1 P_1 - \mathbf{w}_2 P_2, \quad (\text{B.12})$$

where the index vectors $\mathbf{w}_i = [0 \dots \overbrace{1}^{\text{element } n_i} \dots]^T$ have been introduced, applying the constraint forces at the appropriate nodes. External forcing is contained in \mathbf{p}_{ext} . Considering the constraint forces in Eqs. (B.7) and (B.8), the coordinates y_1 and y_2 can be expressed as $y_i = \mathbf{w}_i \mathbf{u}$, whereby Eq. (B.12) becomes

$$\begin{aligned} \mathbf{M}\ddot{\mathbf{u}} + \mathbf{C}\dot{\mathbf{u}} + \mathbf{K}\mathbf{u} &= \mathbf{p}_{ext} - \left(\mathbf{M}_{IA}^s + \cot^2 \theta \mathbf{M}_{IA}^d \right) \ddot{\mathbf{u}} - \mathbf{p}_{IA}(\mathbf{u}, \dot{\mathbf{u}}) \Rightarrow \\ \mathbf{M}^*(\mathbf{u})\ddot{\mathbf{u}} + \mathbf{C}\dot{\mathbf{u}} + \mathbf{K}\mathbf{u} &= \mathbf{p} - \mathbf{p}_{IA}(\mathbf{u}, \dot{\mathbf{u}}), \quad \mathbf{M}^*(\mathbf{u}) = \left(\mathbf{M} + \mathbf{M}_{IA}^s + \cot^2 \theta \mathbf{M}_{IA}^d \right), \end{aligned} \quad (\text{B.13})$$

where the state-dependent mass matrix contributions are defined as

$$\mathbf{M}_{IA}^s = \frac{m_a}{4} (\mathbf{w}_1 + \mathbf{w}_2) (\mathbf{w}_1^T + \mathbf{w}_2^T), \quad (\text{B.14a})$$

$$\mathbf{M}_{IA}^d = \frac{m_a}{4} \frac{h_1^2}{h_2} \left(\mathbf{w}_1 (\mathbf{w}_1^T - \mathbf{w}_2^T) + \mathbf{w}_2 (\mathbf{w}_2^T - \mathbf{w}_1^T) \right), \quad (\text{B.14b})$$

essentially a set of $N \times N$ matrices with contributions at the n_1, n_2 locations alone, i.e., four non-zero elements. The nonlinear force vector from the inertial amplification mechanism $\mathbf{p}_{IA}(y_d, \dot{y}_d)$ is given by

$$\mathbf{p}_{IA}(\mathbf{u}, \dot{\mathbf{u}}) = (\mathbf{w}_1 + \mathbf{w}_2) \cot^2 \theta a i_d^2 \frac{h_1}{h_2} \left(1 + \cot^2 \theta \frac{h_1^2}{h_2} \right), \quad (\text{B.15})$$

which is a vector with ones on the n_1 and n_2 positions multiplied with a scalar, nonlinear function of the displacement and velocity at these nodes.

B.3.1 State space format

The discretized, nonlinear equations of motion in Eq. (B.13) have nonlinear contributions on the right hand side proportional nonlinear functions of displacement and velocity, as well as a state-dependent mass-matrix. They will be solved by numerical integration, using the built-in ordinary differential equations solver in MATLAB. The equations will be implemented in state-space format, by introducing the state vector $\mathbf{y} = [\mathbf{u}^T \ \dot{\mathbf{u}}^T]^T$, and recasting Eq. (B.13) as:

$$\widetilde{\mathbf{M}}(\mathbf{y})\dot{\mathbf{y}} = \mathbf{A}\mathbf{y} + \widetilde{\mathbf{p}}_{ext} + \widetilde{\mathbf{p}}_{IA}(\mathbf{y}), \quad (\text{B.16})$$

where the augmented mass and system matrices along with the force vectors are given as

$$\begin{aligned} \widetilde{\mathbf{M}}(\mathbf{y}) &= \begin{bmatrix} \mathbf{I} & \mathbf{0} \\ \mathbf{0} & \mathbf{M}^*(\mathbf{y}) \end{bmatrix}, \quad \mathbf{A} = \begin{bmatrix} \mathbf{0} & \mathbf{I} \\ -\mathbf{K} & -\mathbf{C} \end{bmatrix}, \\ \widetilde{\mathbf{p}}_{ext} &= \begin{bmatrix} \mathbf{0} \\ \mathbf{p}_{ext} \end{bmatrix}, \quad \widetilde{\mathbf{p}}_{IA}(\mathbf{y}) = \begin{bmatrix} \mathbf{0} \\ -\mathbf{p}_{IA}(\mathbf{y}) \end{bmatrix}. \end{aligned} \quad (\text{B.17})$$

Publication [P1]:

Modal Interaction and Higher Harmonic Generation in a Weakly
Nonlinear, Periodic Mass-Spring Chain¹

¹The manuscript has been edited compared to the one under review due to additional proof reading of the manuscript. No fundamental changes have been introduced.

Modal interaction and higher harmonic generation in a weakly nonlinear, periodic mass-spring chain

Niels M. M. Frandsen^{a,*}, Jakob S. Jensen^b

^a*Section for Solid Mechanics, Department of Mechanical Engineering, Technical University of Denmark, Denmark*

^b*Centre for Acoustic-Mechanical Micro Systems, Department of Electrical Engineering, Technical University of Denmark, Denmark*

Abstract

Wave propagation in a nonlinear periodic material is investigated, by considering an infinite chain of two-mass unit cells with cubic stiffness nonlinearity. The chain is analyzed using the method of multiple scales, predicting the dispersion shift in the band structure due to nonlinear self-interaction. The solution further reveals modest higher harmonic generation within the limits of the solution approach, proportional to the strength of nonlinearity and energy level in the chain. The possibility for controlling the higher harmonic generation by changing the distribution of the cubic nonlinearity is investigated. The predictions based on the analytical model are verified by numerical simulations, which also explores the limits of the infinite, analytical model.

Keywords: Wave propagation, periodic materials, nonlinear materials, higher harmonic generation.

1. Introduction

The fact that periodic materials and structures can exhibit highly interesting dynamic behaviour has been known for, at least, half a century see [1], which also contains a historical description of research before the 1950's. However, the research intensity in periodic materials and structures has increased considerably within the last 25 years, [2, 3, 4].

One of the most interesting and investigated concepts within material dynamics is the *band structure* of the material, which relates the spatial and temporal characteristics of the wave through the wavenumber/frequency relation known as the dispersion relation. The band structure of a periodic material can reveal frequency ranges where waves cannot propagate, known as band gaps or stop bands. The position and width of the stop bands depend on system properties, such as periodicity, material properties and geometry, whereby it is possible to design materials or structures with large gaps in desired frequency locations, e.g. by topology optimization [5].

If the material or structure exhibits nonlinear characteristics, additional effects occur, such as intensity dependent dispersion relations, nonlinear interaction and higher harmonic generation. Investigations of the effects of nonlinearity on the band structure have been carried out in e.g. [6] where they also consider the relation to the normal forms of finite systems and the generation of additional waves due to nonlinear interaction between counter-propagating waves. The work by Narisetti and collaborators in [7, 8] investigates the band structure for one- and two-dimensional nonlinear periodic structures by a perturbation approach. Nonlinear wave-wave interaction is considered by Manktelow et. al. in [9], where they study the effect of interaction between propagating waves on the dispersion in a cubically nonlinear, homogeneous chain. They consider both the general case as well as the special case of internal resonance where there is a 3:1 ratio between wavenumbers and frequencies for the two waves. A similar study was carried out in

*Corresponding author
Email address: nimmfr@mek.dtu.dk (Niels M. M. Frandsen)

[10] for quadratic nonlinearity, investigating the concept of modal lifetime. Wave-wave interaction for general, one-, two- and three-dimensional, nonlinear periodic lattice materials is investigated in [11], a study that is closely related to the present study.

The first order response for a finite periodic chain with quadratic nonlinearity is considered in [12], and it is verified numerically and experimentally how waves might be generated within the band gap due to nonlinear interaction. Yousefzadeh and Phani consider excitation of a cubically nonlinear, finite, damped chain within a stop band in [13], and illustrate a *transmission threshold*, above which energy is transported through the chain due to the loss of stability of the periodic solutions.

The present study considers an infinite, cubically nonlinear, inhomogeneous mass-spring chain. The effects of modal interaction on dispersion is investigated, as well as the higher harmonic generation within the chain. Comparing to the wave-interaction analysis in [11], we consider the self-interaction of the presence of both wave-modes rather than the effect of injecting a control wave in the system. The main emphasis of the present study however, is the prediction of higher harmonic generation and its dependency on the nonlinear system parameters. The goal is to investigate, by analytical means, the potential for controlling the higher harmonic generation within such a chain and thereby enable the optimization of the generation of higher harmonic waves.

2. Model

An infinite chain of two-mass unit cells illustrated in Figure 1 is considered, where k_i and Γ_i are the linear and nonlinear stiffness coefficients respectively, while m_i are the masses in the chain.

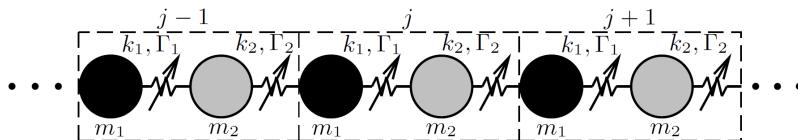


Figure 1: Infinite chain of two-mass unit cells

The governing equations for unit cell j are:

$$\mathbf{M}\ddot{\mathbf{u}}_j + \mathbf{K}\mathbf{u}_j + \mathbf{f}_j^L(u_{j-1,2}, u_{j+1,1}) + \mathbf{f}_j^{NL}(\mathbf{u}_j, u_{j-1,2}, u_{j+1,1}) = \mathbf{0}, \quad \mathbf{u}_j = \begin{bmatrix} u_{j,1}(t) \\ u_{j,2}(t) \end{bmatrix} \quad (1)$$

where $u_{j,n}(t)$ is the displacement of mass n in unit cell j . Furthermore, $\ddot{(\)} = \partial^2/\partial t^2$ and the system matrices and force vectors are given by:

$$\mathbf{M} = \begin{bmatrix} m_1 & 0 \\ 0 & m_2 \end{bmatrix}, \quad \mathbf{K} = \begin{bmatrix} k_1 + k_2 & -k_1 \\ -k_1 & k_1 + k_2 \end{bmatrix}, \quad \mathbf{f}_j^L(u_{j-1,2}, u_{j+1,1}) = -k_2 \begin{bmatrix} u_{j-1,2} \\ u_{j+1,1} \end{bmatrix} \quad (2)$$

$$\mathbf{f}_j^{NL}(\mathbf{u}_j, u_{j-1,2}, u_{j+1,1}) = \begin{bmatrix} \Gamma_1(u_{j,1} - u_{j,2})^3 + \Gamma_2(u_{j,1} - u_{j-1,2})^3 \\ \Gamma_1(u_{j,2} - u_{j,1})^3 + \Gamma_2(u_{j,2} - u_{j+1,1})^3 \end{bmatrix}.$$

The nonlinear equations of motion in Eq. (1) govern the dynamics of the periodic medium illustrated in Figure 1. In Section 3 the wave-characteristics of the infinite chain are investigated by the method of multiple scales, including higher harmonic generation. In Section 4, the higher harmonic predictions of the analytical solution are compared to numerical results. These results are obtained by numerical integration of the governing equations for a finite-length chain that is comparable to the infinite medium.

3. Multiple Scales Analysis

The governing equations for unit cell j in Eq. (1) depend on the motion of the neighbouring cells. For linear periodic systems, the motion of the neighbouring cells can be related to the motion of the considered unit cell through a phase-multiplier, by the Floquet-Bloch theorem [14]. The wave-characteristics of the nonlinear medium are investigated by approximating the nonlinear equations by a set of linear ones, using the method of multiple scales, [15].

The method of multiple scales is a perturbation approach, hence the nonlinear elastic forces are assumed to be much smaller than the linear, i.e.,

$$\mathbf{M}\ddot{\mathbf{u}}_j + \mathbf{K}\mathbf{u}_j + \mathbf{f}_j^L(u_{j-1,2}, u_{j+1,1}) + \varepsilon \tilde{\mathbf{f}}_j^{NL}(\mathbf{u}_j, u_{j-1,2}, u_{j+1,1}) = \mathbf{0} \quad (3)$$

where the parameter ε is a book-keeping parameter, indicating the smallness of the nonlinear terms, i.e, $\varepsilon \tilde{\mathbf{f}}_j^{NL} = \mathbf{f}_j^{NL} = O(\varepsilon)$. A uniformly valid expansion of the displacements in unit cell j is made:

$$\mathbf{u}_j(t) = \mathbf{u}_j^{(0)}(T_0, T_1) + \varepsilon \tilde{\mathbf{u}}_j^{(1)}(T_0, T_1) + O(\varepsilon^2), \quad T_k = \varepsilon^k t, \quad |\varepsilon \tilde{\mathbf{u}}_j^{(1)}| = |\mathbf{u}_j^{(1)}| \ll |\mathbf{u}_j^{(0)}| \quad (4)$$

where two new time-scales have been introduced. Inserting in Eq. (3) and setting terms of equal power in ε to zero yields:

$$\varepsilon^0 : \quad \mathbf{M}D_0^2 \mathbf{u}_j^{(0)} + \mathbf{K}\mathbf{u}_j^{(0)} + \mathbf{f}_j^{L,(0)} = 0 \quad (5a)$$

$$\varepsilon^1 : \quad \mathbf{M}D_0^2 \tilde{\mathbf{u}}_j^{(1)} + \mathbf{K}\tilde{\mathbf{u}}_j^{(1)} + \mathbf{f}_j^{L,(1)} = -2\mathbf{M}D_0 D_1 \mathbf{u}_j^{(0)} - \mathbf{f}_j^{NL,(0)} \quad (5b)$$

where $D_k^i = \partial^i / \partial T_k^i$, and terms of order $O(\varepsilon^2)$ and above have been disregarded. The governing, nonlinear equations are now represented by linear equations at two levels of approximation. The functional dependence of the force vectors on the displacements have been left out for brevity. The order ε^0 equations in Eq. (5a) are satisfied by a travelling wave solution:

$$\mathbf{u}_j^{(0)}(T_0, T_1) = a(T_1) \begin{bmatrix} A_1 \\ A_2 \end{bmatrix} e^{i(\mu j + \omega T_0)} + c.c. = a(T_1) \mathbf{v} e^{i(\mu j + \omega T_0)} + c.c. \quad (6)$$

where $a(T_1)$ is a complex amplitude that depends on slow time T_1 , and $c.c.$ denotes complex conjugate. The relative amplitudes of the masses are given by A_i while μ and ω are the wavenumber and propagating frequency respectively. Imposing the wave-solution in the order ε^0 equations and using the Floquet-Bloch theorem, leads to a wavenumber-dependent eigenvalue-problem in ω^2 and \mathbf{v} . Using the transformation $\mathbf{v} = \mathbf{M}^{-1/2} \mathbf{z}$ where $\mathbf{M}^{-1/2} = \text{diag}[\sqrt{m_1} \ \sqrt{m_2}]$ and pre-multiplying by $\mathbf{M}^{-1/2}$ provides the normalized eigenvalue-problem:

$$\left(\tilde{\mathbf{K}}(\mu) - \bar{\omega}^2 \mathbf{I} \right) \mathbf{z} a(T_1) = \mathbf{0}, \quad \tilde{\mathbf{K}}(\mu) = \begin{bmatrix} 1 & -(c_1 + c_2 e^{-i\mu}) \\ -(c_1 + c_2 e^{i\mu}) & \beta \end{bmatrix} \quad (7)$$

where $\bar{\omega} = \omega / \omega_n$, $\omega_n^2 = (k_1 + k_2) / m_1$, $\beta = m_1 / m_2$ and $c_i^2 = k_i / (\omega_n^2 \sqrt{m_1 m_2})$. Solving the eigenvalue problem in Eq. (7) provides the eigenvalues and -vectors:

$$\bar{\omega}_k^2 = \frac{1}{2} \left(1 + \beta \pm \sqrt{(1 - \beta)^2 + 4(c_1^4 + c_2^4 + 2c_1^2 c_2^2 \cos(\mu))} \right) \quad (8a)$$

$$\mathbf{z}_k = \begin{bmatrix} -\frac{2(c_1^2 + c_2^2 e^{-i\mu})}{\beta - 1 \pm \sqrt{(1 - \beta)^2 + 4(c_1^4 + c_2^4 + 2c_1^2 c_2^2 \cos(\mu))}} & 1 \end{bmatrix}^T, \quad k = 1, 2 \quad (8b)$$

corresponding to the linear propagation frequencies and relative amplitudes of the masses in the two modes supported by the two-mass unit cell. The lower mode ($k = 1$) is traditionally referred

to as the acoustic mode, while the upper mode ($k = 2$) is referred to as the optical mode. The full solution to the order ε^0 equations is:

$$\mathbf{u}_j^{(0)}(T_0, T_1) = \sum_{k=1}^2 a_k(T_1) \mathbf{v}_k e^{i(\mu j + \omega_k T_0)} + c.c., \quad \mathbf{v}_k = \mathbf{M}^{-1/2} \mathbf{z}_k \quad (9)$$

where $a_k(T_1)$ will be determined at the next level of approximation. Inserting the order ε^0 solution into Eq. (5b) leads to the order ε^1 equations:

$$\begin{aligned} \mathbf{M}D_0^2 \mathbf{u}_j^{(1)} + \mathbf{K} \mathbf{u}_j^{(1)} + \mathbf{f}_j^{L,1} &= \mathbf{q}_1 e^{i(\mu j + \omega_1 T_0)} + \mathbf{q}_2 e^{i(\mu j + \omega_2 T_0)} + \mathbf{q}_{12} e^{i(\mu j + (2\omega_1 - \omega_2) T_0)} \\ &+ \mathbf{q}_{21} e^{i(\mu j + (2\omega_2 - \omega_1) T_0)} + \mathbf{p}_{12} e^{i(3\mu j + (2\omega_1 + \omega_2) T_0)} \\ &+ \mathbf{p}_{21} e^{i(3\mu j + (\omega_1 + 2\omega_2) T_0)} + \mathbf{p}_1 e^{3i(\mu j + \omega_1 T_0)} + \mathbf{p}_2 e^{3i(\mu j + \omega_2 T_0)} + c.c. \end{aligned} \quad (10)$$

where the coefficient vectors depend on the complex modal amplitudes, a_1 , a_2 , and the wavenumber μ . They can be found in Appendix A. Any loading terms in Eq. (10) with functional dependence on the eigenvalues of the linear problem will lead to secular behaviour of the solution and must be eliminated. It is clear that the coefficient vectors \mathbf{q}_1 and \mathbf{q}_2 will always lead to secular behaviour. Furthermore, for specific wavenumber/frequency combinations, additional resonant terms can occur. This is the case of *internal resonance*, where the higher harmonic excites an eigen-mode of the system. This will cause the uniformity of expansion, $|\mathbf{u}_j^{(1)}| \ll |\mathbf{u}_j^{(0)}|$, to break down, and should be considered separately. Internal resonance is not a focus of the present paper, hence we will focus on the case where only \mathbf{q}_1 and \mathbf{q}_2 are resonant. They will be eliminated by choosing the complex modal amplitudes $a_k(T_1)$ appropriately, whereby the nonlinear frequency corrections are obtained.

3.1. Frequency corrections

Considering the case away from internal resonance, Eq. (10) reduces to

$$\mathbf{M}D_0^2 \mathbf{u}_j^{(1)} + \mathbf{K} \mathbf{u}_j^{(1)} + \mathbf{f}_j^{L,1} = \mathbf{q}_1 e^{i(\mu j + \omega_1 T_0)} + \mathbf{q}_2 e^{i(\mu j + \omega_2 T_0)} + OHT + c.c. \quad (11)$$

where *OHT* denotes Other Harmonic Terms. Several approaches for determining the solvability condition, eliminating secular behaviour from Eq. (10), exist. Here a straightforward modal approach is used. A modal solution to the order ε^1 equations is assumed:

$$\mathbf{u}_j^{(1)}(T_0, T_1) = \mathbf{V} \mathbf{r}(j, T_0, T_1), \quad \mathbf{V} = [\mathbf{v}_1 \ \mathbf{v}_2] = \mathbf{M}^{-1/2} \mathbf{Z}, \quad \mathbf{r}(j, T_0, T_1) = \begin{bmatrix} r_1(j, T_0, T_1) \\ r_2(j, T_0, T_1) \end{bmatrix} \quad (12)$$

where \mathbf{Z} is the modal matrix of orthogonal eigenvectors. Inserting in Eq. (10) and premultiplying by $\mathbf{Z}^H \mathbf{M}^{-1/2}$ yields

$$\mathbf{Z}^H \mathbf{Z} D_0^2 \mathbf{r} + \mathbf{Z}^H \tilde{\mathbf{K}}(\mu) \mathbf{Z} \mathbf{r} = \hat{\mathbf{q}}_1 e^{i(\mu j + \omega_1 T_0)} + \hat{\mathbf{q}}_2 e^{i(\mu j + \omega_2 T_0)} \quad (13)$$

where superscript H indicates Hermitian transpose while $\hat{\mathbf{q}}_i = \mathbf{Z}^H \mathbf{M}^{-1/2} \mathbf{q}_i$. Since the eigenvectors are orthogonal, the left hand side of Eq. (13) decouples, whereby the system of equations can be written as two separate, modal equations,

$$D_0^2 r_k + \omega_k^2 r_k = \hat{q}_{1k} e^{i(\mu j + \omega_1 T_0)} + \hat{q}_{2k} e^{i(\mu j + \omega_2 T_0)} + c.c., \quad k = 1, 2 \quad (14)$$

where the eigenvalues of the homogeneous part are $\omega_k^2 = \mathbf{z}_k^H \tilde{\mathbf{K}}(\mu) \mathbf{z}_k / \mathbf{z}_k^H \mathbf{z}_k$. The decoupled equations reveal that \hat{q}_{11} is resonant to the first mode while \hat{q}_{22} is resonant to the second mode. Thus, the solvability condition is:

$$\widehat{q}_{11} = \mathbf{z}_1^H \mathbf{M}^{-1/2} \mathbf{q}_1 = 0 \quad (15a)$$

$$\widehat{q}_{22} = \mathbf{z}_2^H \mathbf{M}^{-1/2} \mathbf{q}_2 = 0 \quad (15b)$$

which can be obtained by the adjoint eigenvector approach from [15] as well. Using the expressions for the coefficient vectors \mathbf{q}_1 and \mathbf{q}_2 from Eqs. (A.1) leads to the two complex equations:

$$-i2\omega_1 a'_1 - 3a_1^2 \bar{a}_1 \eta_1 - 6a_1 a_2 \bar{a}_2 \xi_{12} = 0 \quad (16a)$$

$$-i2\omega_2 a'_2 - 3a_2^2 \bar{a}_2 \eta_2 - 6a_2 a_1 \bar{a}_1 \xi_{21} = 0 \quad (16b)$$

where $a'_k = da_k/dT_1$ and the scalars η_k and ξ_{ki} are defined as:

$$\eta_k = \frac{\mathbf{z}_k^H \mathbf{M}^{-1/2}}{\mathbf{z}_k^H \mathbf{z}_k} \sum_{l,m,n} \mathbf{h}_{lmn} z_k^l z_k^m \bar{z}_k^n \quad \xi_{ki} = \frac{\mathbf{z}_k^H \mathbf{M}^{-1/2}}{\mathbf{z}_k^H \mathbf{z}_k} \sum_{l,m,n} \mathbf{h}_{lmn} z_k^l z_i^m \bar{z}_i^n, \quad \begin{matrix} k = 1, 2 \\ i = 1, 2 \end{matrix} \quad (17)$$

The coefficient vector \mathbf{h}_{lmn} can be found in Table A.3, and z_k^p is the p^{th} element of the normalized eigenvector of mode k . The complex modal amplitudes are now expressed on polar form, $a_k = \frac{\alpha_k}{2} e^{i\varphi_k}$, where $\alpha_k(T_1)$ and $\varphi_k(T_1)$ are real-valued functions. Separating the real and imaginary parts leads to four coupled modulation equations governing the slow-time variation of the order ε^0 solution.

$$\omega_1 \alpha'_1 = 0 \quad (18a)$$

$$\omega_1 \alpha_1 \varphi'_1 = \frac{3}{8} \eta_1 \alpha_1^3 + \frac{3}{4} \xi_{12} \alpha_1 \alpha_2^2 \quad (18b)$$

$$\omega_2 \alpha'_2 = 0 \quad (18c)$$

$$\omega_2 \alpha_2 \varphi'_2 = \frac{3}{8} \eta_2 \alpha_2^3 + \frac{3}{4} \xi_{21} \alpha_2 \alpha_1^2 \quad (18d)$$

It is noted that the scalars defined in Eq. (17) are entirely real entities. The amplitudes are seen to be constant in slow time, $\alpha_1(T_1) = \alpha_{10}$ and $\alpha_2(T_1) = \alpha_{20}$, whereby the phase equations are easily integrated.

$$\varphi_1(T_1) = \frac{3}{8} \frac{\eta_1}{\omega_1} \alpha_{10}^2 T_1 + \frac{3}{4} \frac{\xi_{12}}{\omega_1} \alpha_{20}^2 T_1 + \varphi_{10}, \quad \alpha_{10} \neq 0 \quad (19a)$$

$$\varphi_2(T_1) = \frac{3}{8} \frac{\eta_2}{\omega_2} \alpha_{20}^2 T_1 + \frac{3}{4} \frac{\xi_{21}}{\omega_2} \alpha_{10}^2 T_1 + \varphi_{20}, \quad \alpha_{20} \neq 0 \quad (19b)$$

Hence, the order ε^0 solution is

$$\mathbf{u}_j^{(0)}(t) = \frac{\alpha_{10}}{2} \mathbf{v}_1 e^{i\varphi_1} e^{i(\mu_j + \omega_1 t)} + \frac{\alpha_{20}}{2} \mathbf{v}_2 e^{i\varphi_2} e^{i(\mu_j + \omega_2 t)} + c.c. \quad (20)$$

where the original time-variable has been reintroduced. The parameters α_{k0} and φ_{k0} depend on the initial conditions. The first-order corrected frequencies $\tilde{\omega}_k$ are:

$$\tilde{\omega}_1 = \omega_1 + \varepsilon \left(\frac{3}{8} \frac{\eta_1}{\omega_1} \alpha_{10}^2 + \frac{3}{4} \frac{\xi_{12}}{\omega_1} \alpha_{20}^2 \right) = \omega_1 + \varepsilon (\Delta\omega_{11} + \Delta\omega_{12}) \quad (21a)$$

$$\tilde{\omega}_2 = \omega_2 + \varepsilon \left(\frac{3}{8} \frac{\eta_2}{\omega_2} \alpha_{20}^2 + \frac{3}{4} \frac{\xi_{21}}{\omega_2} \alpha_{10}^2 \right) = \omega_2 + \varepsilon (\Delta\omega_{21} + \Delta\omega_{22}) \quad (21b)$$

revealing that for the two-mass chain, the presence of both waves affects the propagation frequencies for both modes through the coupling terms $\Delta\omega_{12}$ and $\Delta\omega_{21}$. Figure 2 illustrates the effect of modal interaction for an example chain with the parameters given in Table 1, in the normalized range $\bar{\mu} = \mu/\pi$, $\bar{\omega} = \omega/\omega_n$, covering the irreducible Brillouin zone. The amplitudes have been

Table 1: Model parameters

m_1	m_2	k_1	k_2	Γ_1	Γ_2	β	ω_n	c_1	c_2
1	2	1	5	± 0.05	± 0.05	0.5	2.45	0.34	0.77

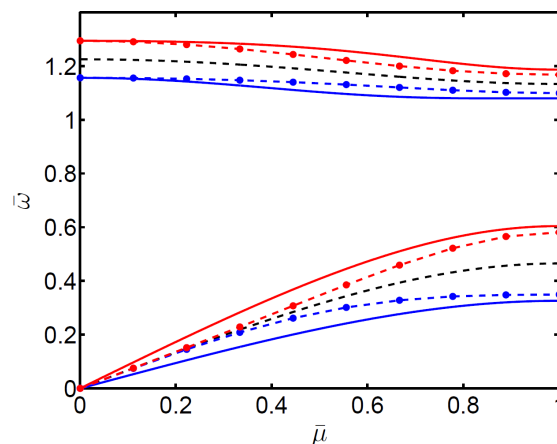


Figure 2: Band structure, $\alpha_{10} = 2$, $\alpha_{20} = 2$. Dashed lines: linear dispersion, solid lines: nonlinear corrections (softening and hardening), dash-dot lines: excluding modal interaction

chosen relatively large to exaggerate the results for easier visual inspection. The dashed black lines represent the linear dispersion, while the dash-dot lines represent the case where there is no modal interaction, obtained by imposing the waves separately. The solid lines represent the dispersion when accounting for the modal interaction, as given by Eqs. (21). The curves below the linear dispersion correspond to pure softening nonlinearity $\Gamma_1 = \Gamma_2 = -0.05$, while the curves above correspond to pure hardening nonlinearity $\Gamma_1 = \Gamma_2 = 0.05$. The figure illustrates that modal interaction between the two supported modes, does indeed alter the band structure of the nonlinear material. This was expected from the results of wave-interaction from [11], however the present model accounts for the full modal solution in a two-mass nonlinear periodic chain. It is noted that the largest effect of including modal interaction is found near the middle of the first Brillouin zone, which means that the largest frequency shift, and perhaps even the gap limits, might *not* be found on the edges of the first zone. This should be kept in mind if doing a systematic design, or simply, if considering 2D-structures, where the band structure is usually determined by spanning the edge of the first Brillouin zone.

3.2. First order response

The approximate analytical response $\mathbf{u}_j(t)$ is obtained as the sum of the homogeneous solution to the order ε^0 equations and the particular solutions to the order ε^1 equations. The homogeneous solution is already known, and determining the particular solutions means solving the equations:

$$\begin{aligned}
\mathbf{M}D_0^2\mathbf{u}_j^{(1)} + \mathbf{K}\mathbf{u}_j^{(1)} + \mathbf{f}_j^{L,1} &= \mathbf{q}_{12}e^{i(\mu j + (2\omega_1 - \omega_2)T_0)} + \mathbf{q}_{21}e^{i(\mu j + (2\omega_2 - \omega_1)T_0)} + \mathbf{p}_{12}e^{i(3\mu j + (2\omega_1 + \omega_2)T_0)} \\
&+ \mathbf{p}_{21}e^{i(3\mu j + (\omega_1 + 2\omega_2)T_0)} + \mathbf{p}_1e^{3i(\mu j + \omega_1 T_0)} + \mathbf{p}_2e^{3i(\mu j + \omega_2 T_0)} + c.c.
\end{aligned} \tag{22}$$

We will focus on higher harmonic generation from the acoustic branch when it exists alone, i.e. $\alpha_{20} = 0$. Hence, Eqs. (22) reduces to

$$\mathbf{M}D_0^2\mathbf{u}_j^{(1)} + \mathbf{K}\mathbf{u}_j^{(1)} + \mathbf{f}_j^{L,1} = -\frac{\alpha_{10}^3}{8}\mathbf{b}_3e^{3i(\mu j + \tilde{\omega}_1 t)} + c.c. \quad (23)$$

where $\mathbf{b}_3 = \sum_{l,m,n} \mathbf{g}_{lmn} z_1^l z_1^m z_1^n$ and the amplitude and phase relations from Eqs. (18) have been utilized. The vector \mathbf{g}_{lmn} can be found in Table A.4. Inserting a travelling wave solution in Eq. (23), $\mathbf{u}_{\text{part}} = \mathbf{y}e^{3i(\mu j + \tilde{\omega}_1 T_0)} + c.c.$, and applying the Floquet-Bloch theorem, leads to the algebraic system of equations:

$$(\mathbf{K}(3\mu) - (3\tilde{\omega}_1)^2\mathbf{M})\mathbf{y} = -\frac{\alpha_{10}^3}{8}\mathbf{b}_3 \quad (24)$$

which can be solved for the coefficient vector \mathbf{y} . The total, approximate response is then

$$\mathbf{u}_j(t) = \mathbf{u}_j^{(0)}(t) + \mathbf{u}_j^{(1)}(t) = \frac{1}{2}\alpha_{10}\mathbf{v}_1e^{i(\mu j + \tilde{\omega}_1 t)} - \frac{1}{8}\alpha_{10}^3(\mathbf{K}(3\mu) - (3\tilde{\omega}_1)^2\mathbf{M})^{-1}\mathbf{b}_3e^{3i(\mu j + \tilde{\omega}_1 t)} + c.c. \quad (25)$$

With the first order response determined, we will investigate higher harmonic generation from an acoustic wave at four different wavenumber/frequency points on the linear acoustic dispersion curve, given in Table 2. The four points represent four distinct regimes of the higher harmonic.

Table 2: Dispersion points

$\bar{\mu}$	0.10	0.20	0.40	0.66
$\tilde{\omega}_1(\bar{\mu})$	0.07	0.13	0.26	0.39

They are illustrated in Figure 3, where identical markers correspond to the fundamental and higher harmonic respectively and the second Brillouin-zone has been included to illustrate the higher harmonic of the last wavenumber/frequency point. For the first, long-wave limit point (blue plus-sign), the higher harmonic is very close to the linear dispersion curve. Hence, it represents a limit where the analytical model might not be valid since internal resonance could be an issue, as investigated for a mono-atomic model in [9]. The results of the mentioned reference however, indicate only modest effects of internal resonance on dispersion in the long-wave limit, but the possible self-excitation from resonant higher harmonic generation is the focus here. The second point (red cross) corresponds to the higher harmonic being away from the dispersion branch, but still within the acoustic pass-band, while the third point (magenta asterisk) has the higher harmonic within the stop-band. For the fourth point (black star), the higher harmonic falls within the optical pass-band, i.e. the higher harmonic is within the pass-band of the “non-excited” mode. It is noted that the actual loading frequency of the order ε^1 equations will be the nonlinear acoustic frequency, $\tilde{\omega}_1$, however for the purpose of identifying the four described regimes of wavenumber/frequency points, the linearized points will suffice. The higher harmonic generation will be investigated for varying nonlinear stiffness-contrast, Γ_1/Γ_2 , considering four fixed values of $\Gamma_2 = (0.001, 0.005, 0.01, 0.05)$. In order to be able to compare the results from the four wavenumber/frequency points, the four configurations are investigated for the same *input energy*, defined as the maximum kinetic energy of the linear response:

$$E_0 = |E_{\text{kin}}^{(0)}| = \left| \frac{1}{2} \dot{\mathbf{u}}_j^T \mathbf{M} \dot{\mathbf{u}}_j \right| = \frac{1}{2} \tilde{m}_1 (\alpha_{10} \omega_1)^2 \quad (26)$$

where $\tilde{m}_1 = \Re(\mathbf{z}_1^T) \Re(\mathbf{z}_1)$ is the modal mass of the acoustic mode. The higher harmonic generation is quantified in terms of the ratio between the third and first harmonic, i.e.

$$\frac{|A_3|}{|A_1|} = \frac{|\mathbf{u}_j^{(1)}|}{|\mathbf{u}_j^{(0)}|} \quad (27)$$

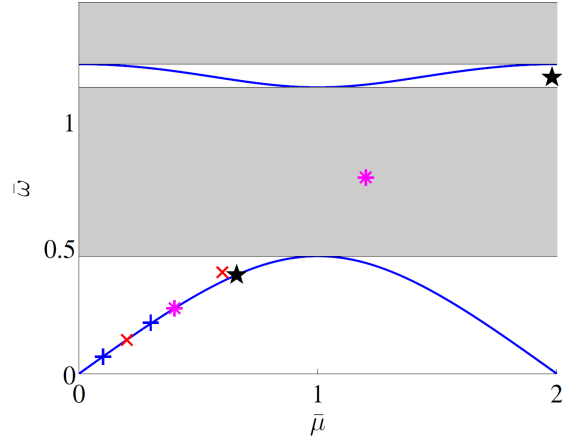


Figure 3: Investigated $\bar{\mu}$ -values. Blue plus-signs: Long-wave limit, red crosses: higher harmonic in acoustic pass band, magenta asterisks: higher harmonic in stop band, black stars: higher harmonic in optical pass band.

Figure 4 illustrates how the higher harmonic generation varies with nonlinear stiffness contrast for the four wavenumber/frequency points from Table 2 and input energy $E_0 = 0.1$.

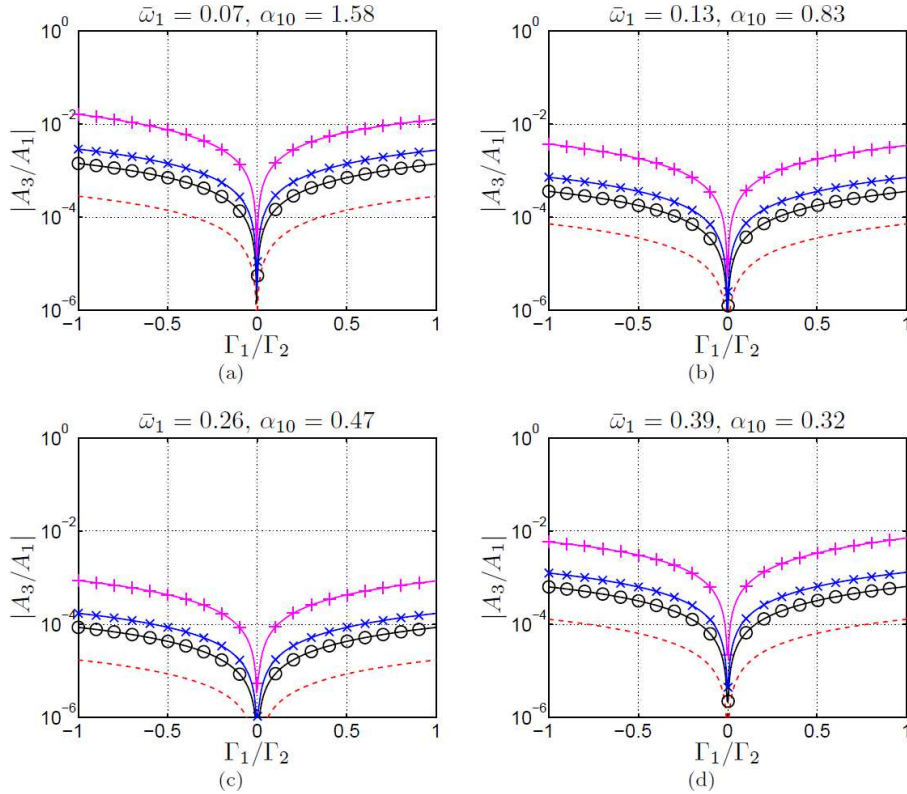


Figure 4: Effect of nonlinear stiffness ratio, $E_0 = 0.1$. Dashed red line: $\Gamma_2 = 0.001$, black circles: $\Gamma_2 = 0.005$, blue crosses: $\Gamma_2 = 0.01$, magenta plus-signs: $\Gamma_2 = 0.05$.

It is clear that larger nonlinear coefficients lead to a larger level of higher harmonic generation. The variation with nonlinear stiffness ratio is seen to be almost symmetric around zero, i.e. the higher harmonic generation appears to be fairly insensitive to whether the chain is purely hardening or periodically softening/hardening. Furthermore it can be seen that higher harmonic generation

is lowest when it falls within a stop-band, illustrated by Figure 4(c), and that it is largest when it is close to a dispersion branch, as illustrated by Figure 4(a). Finally it is noted that, not surprisingly, a much smaller amplitude produces the same level of kinetic energy as the frequency increases from $\bar{\omega}_1 = 0.07$ to $\bar{\omega}_1 = 0.39$.

The maximal higher harmonic generation illustrated in Figure 4 is approximately two orders of magnitude smaller than the input wave, $\max(A_3/A_1) \approx 0.01$, i.e. the perturbation assumption of the solution seems to be fulfilled. Figure 5 illustrates the development with nonlinear stiffness ratio for the input energy level $E_0 = 1$.

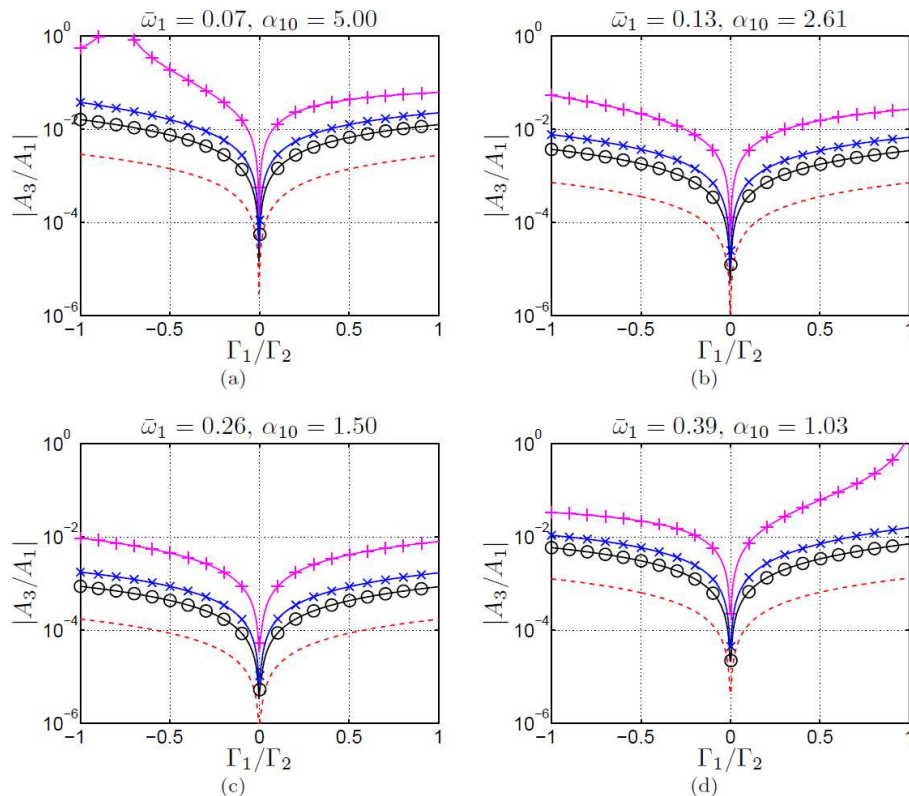


Figure 5: Effect of nonlinear stiffness ratio, $E_0 = 1$. Dashed red line: $\Gamma_2 = 0.001$, black circles: $\Gamma_2 = 0.005$, blue crosses: $\Gamma_2 = 0.01$, magenta plus-signs: $\Gamma_2 = 0.05$.

The first thing that is noted, is the appearance of resonance-like peaks for $\bar{\omega}_1 = 0.07$ and $\bar{\omega}_1 = 0.39$. These are the result of internal resonance, and will be discussed further in Section 3.2.1. Aside from these peaks, the general level of higher harmonic generation has increased by approximately one order of magnitude, same as the input energy. This direct scaling of output with input is a result of the approximate solution method, and will only be applicable for weak nonlinearities, i.e. when the nonlinear elastic forces in Eq. (1) are much smaller than the linear ones and as long as the uniformity of the expansion in Eq. (4) is kept. Hence, when the amplitude of the higher harmonic becomes comparable to that of the fundamental harmonic, the model stops producing reliable results. This limitation is illustrated further in Section 4.

3.2.1. Internal resonance

As seen in Figure 5, certain parameter combinations lead to resonance-type behaviour of the order ε^1 response. This violates the uniformity of expansion assumption, and consequently the model breaks down for these parameter combinations. However, as mentioned previously, the analysis does not account for *internal resonance*, the case where the higher harmonic excites an eigen-mode for the system. While the problem is not explicitly revealed by considering the disper-

sion alone, see Figure 2, the analysis of higher harmonic generation reveals the model breakdown. Figure 6 shows the band-diagram for the infinite chain at the two identified problematic parameter combinations.

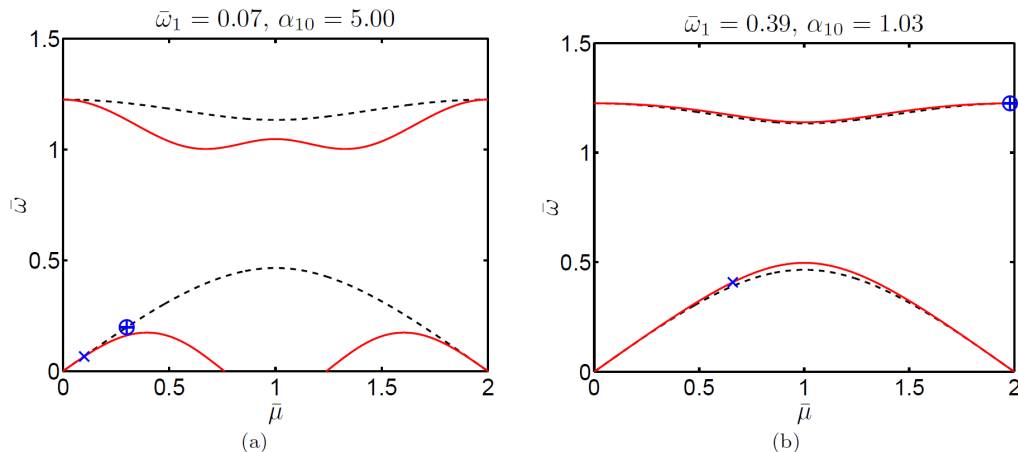


Figure 6: Internal resonance illustration, $E_0 = 1$. Dashed line: Linear dispersion, solid line: Nonlinear dispersion, blue cross: $\tilde{\omega}_1(\mu)/\omega_n$, blue plus-sign: $3\tilde{\omega}_1(\mu)/\omega_n$, blue circle: $\tilde{\omega}_{1,2}(3\mu)$

It can be seen that the higher harmonic $3\tilde{\omega}_1$ falls exactly on the linear dispersion curve, essentially exciting the system at an eigenvalue. This leads to secular behaviour that should be avoided by imposing specific solvability conditions at the particular frequency ratios leading to internal resonance. This, however, is outside the scope of this work. It is noted that, for $\bar{\omega}_1 = 0.07$ the perturbative nature of the solution approach is clearly violated, since the frequency correction is by no means “small”. This cannot be seen for the $\bar{\omega}_1 = 0.39$ case however, illustrating the potential danger of relying strictly on the analytical model, especially when only a partial range of $\bar{\mu}$ is considered. The points of singularity however, can be predicted directly from the dispersion curves so, if remembered, the limits of the analysis method can be evaluated quite directly.

4. Numerical Analysis

The approximate response obtained by the analytical model is compared to the numerically obtained response of a finite-length chain. This is done to investigate the validity of the prediction of higher harmonic generation from the analytical model.

4.1. Model

The numerical model consists of a finite number of unit cells $N_{cell} = 878$, providing 1756 DOFs. The chain is loaded at the left end by a harmonic force that ramps up from zero over the course of 8 loading periods, i.e.,

$$F(t) = F_0 (1 - e^{-\zeta_{ramp} t}) \sin(\Omega t) \quad (28)$$

where ζ_{ramp} is determined by

$$\zeta_{ramp} = -\frac{\ln(1 - 0.99)}{8 \frac{2\pi}{\Omega}} \quad (29)$$

i.e., such that the parenthesis in Eq. (28) is equal to 0.99 after 8 loading periods. In order to avoid any transients in the response, the first part of the chain is (lightly) damped. The damping is imposed by adding viscous dampers between the masses, for a number of unit cells corresponding to five wavelengths of a linear acoustic wave with frequency Ω . The viscous damping is then decreased exponentially over a distance corresponding to five more wavelengths of the acoustic

wave to avoid any effects of a discontinuous change in damping properties. The application of the load and damping to the chain is illustrated in Figure 7.

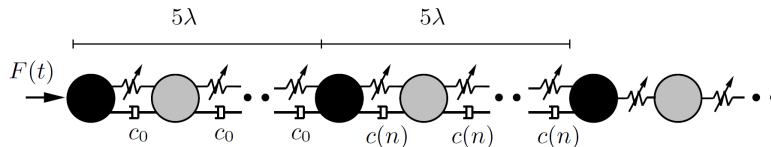


Figure 7: Chain with applied damping and load

The wavelength of the acoustic wave is $\lambda(\Omega = \omega_1)$, the constant damping coefficient is $c_0 = 0.01 \cdot \omega_n^2 \max(m_1, m_2) = 0.06$ and $c(n)$ is the exponentially decreasing damping coefficient, given by $c(n) = c_0 e^{-\zeta_d n}$ where n is the mass-number and ζ_d is determined such that the exponential function is equal to 0.01 after 5 wavelengths.

4.2. Higher harmonic generation

The finite chain is investigated for the same four frequencies as in Sec. 3.2, i.e., $\bar{\Omega} = \Omega/\omega_n = \bar{\omega}_1$, given in Table 2. The response of the finite chain is calculated for increasing values of the load amplitude F_0 . The simulation time for each simulation is chosen as the travel time for an acoustic wave from the left to the right end of a corresponding linear chain. This simulation time is chosen to avoid reflections from the right boundary in the investigated signals. The numerical simulations will be carried out for a chain with the material parameters given in Table 1. The numerically obtained response signals of the finite chain are processed by Fourier transforms, in order to obtain the spectral properties as well as the amplitudes of the different harmonics in the signal. The Fourier transforms are done in both the time and space domain, to obtain the actual wavenumber/frequency content of the wave travelling through the chain. The temporal Fourier transform is done for a specific mass, considering only the second half of the simulation time to ensure that a fully developed wave has reached the mass before beginning the transform. The time signal is additionally processed by cutting off any ‘‘partial periods’’ at either end of the signal, so that it is approximately periodic. The signal has further been windowed by a scaled Hann-window such that the amplitudes are conserved in the frequency spectrum, ensuring correct amplitude information. A similar window has been used for the spatial Fourier transform. Figure 8(a) shows how an excited wave travels through the chain by four snapshots in normalized time $\bar{t} = t/t_{\text{final}}$, where the dashed, vertical black line indicates where the damping stops and the dotted, vertical magenta lines indicate the domain processed by the spatial Fourier transform. Figure 8(b) is the temporal Fourier transform of the mass marked by the red dot in Figure 8(a). The simulation is carried out for the normalized wavenumber $\bar{\mu} = 0.2$ and load amplitude $F_0 = 0.25$.

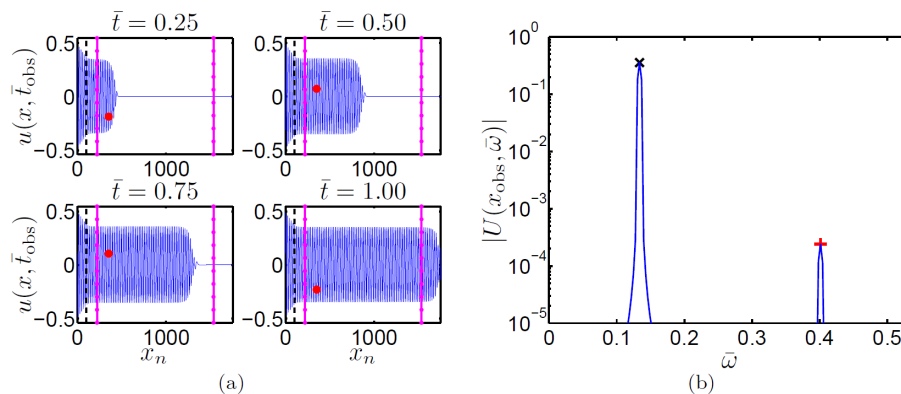


Figure 8: Example simulation for $\bar{\mu} = 0.2$ and $F_0 = 0.25$. Black cross: $\bar{\Omega}$. Red plus-sign: $3\bar{\Omega}$.

Considering Figure 8(b), the higher harmonic generation is evident from the peak at $3\bar{\omega}$. This higher harmonic generation from the numerical model will be compared to what is obtained by the analytical model described in Sec. 3.2. The analytical model requires information about the amplitude of the fundamental wave, α_{10} , as well as the wavenumber of the wave. The wavenumber is obtained directly from the spatial Fourier transform of the domain illustrated in Figure 8(a). Figure 9 shows the transform at the final time t_{final} , illustrating a peak at the expected normalized wavenumber $\bar{\mu} = 0.2$.

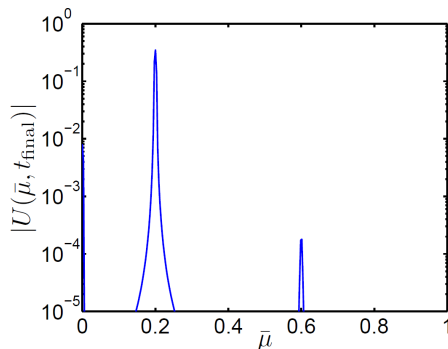


Figure 9: Spatial transform.

It should be noted that the wavenumber measured in the chain shifts slightly with nonlinearity, hence we use the measured wavenumber as input for the analytical calculations.

The amplitude of the fundamental wave is obtained from the temporal Fourier transform. It is related to the analytical amplitude α_{10} through the analytical order ε^0 solution when only the acoustic wave is present,

$$\mathbf{u}_j = \frac{1}{2}\alpha_{10} \left(\mathbf{v}_1 e^{i(\mu j + \bar{\omega}_1 T_0)} + \bar{\mathbf{v}}_1 e^{-i(\mu j + \bar{\omega}_1 T_0)} \right) \quad (30)$$

where an overbar means complex conjugate. The max displacement in the unit cell is given by

$$u_{j,max} = \alpha_{10} \max(\Re(\mathbf{v}_1)) \quad (31)$$

which can be compared directly to the numerically obtained amplitude of the fundamental harmonic, A_1 . Hence, the analytical amplitude α_{10} is obtained from the numerical simulation by

$$\alpha_{10} = \frac{A_1}{\max(\Re(\mathbf{v}_1))} \quad (32)$$

whereby the analytical model can be compared to the numerical model. Figure 10 compares the higher harmonic generation predicted by the analytical and numerical model respectively for the four loading frequencies given in Table 2.

The crosses and plus-signs represent the numerical and analytical results for measured amplitudes and wavenumbers respectively. The dashed black line approximate the continuous analytical prediction of the higher harmonic generation when the wavenumber is approximated as as the wavenumber corresponding to the input frequency on the linear acoustic dispersion curve rather than the measured wavenumber. The figure illustrates that the analytical model generally predicts the higher harmonic generation well for lower input energies. As the input energy increases, so does the higher harmonic generation, and after a certain threshold, the analytical model stops being accurate. In particular, the long-wave limit case where the higher harmonic is near the acoustic dispersion curve, the results from the analytical model is seen to deteriorate as the input energy E_0 approaches 1. The analytical predictions are noted to be larger than the numerical results for the investigated energy spectrum in the case with the higher harmonic in the optical pass band. Hence, it appears the the analytical model reaches its limits of accuracy *before* the

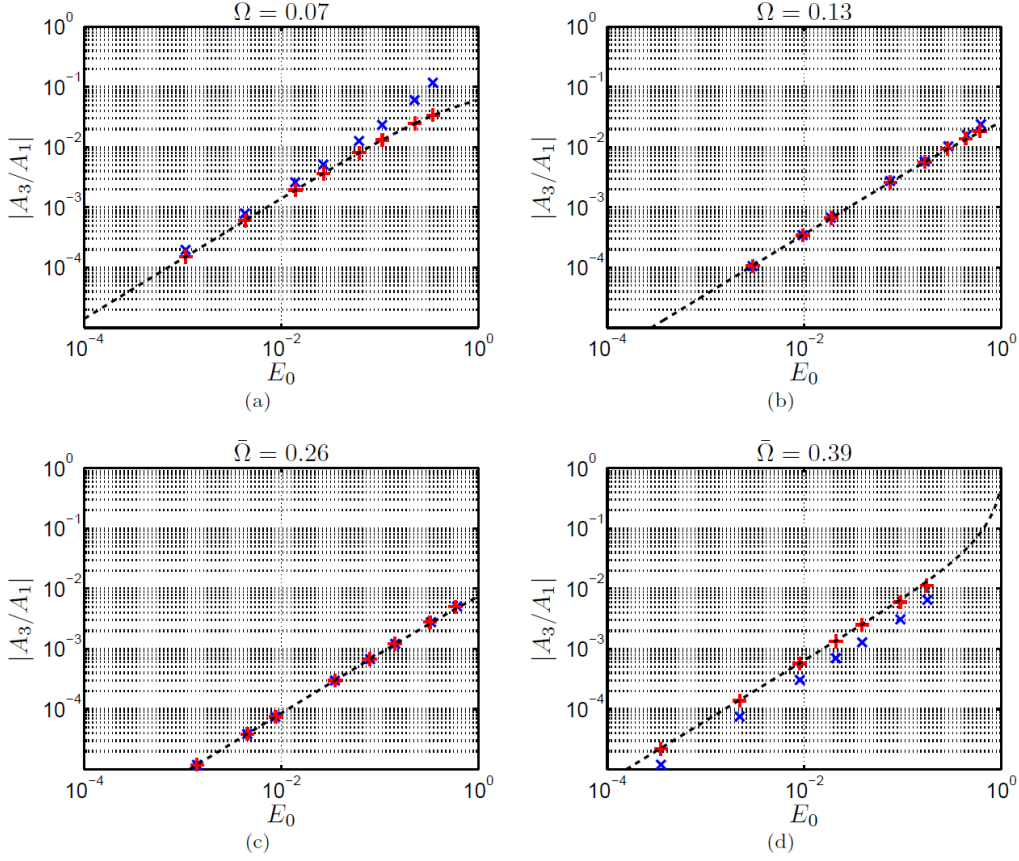


Figure 10: Higher harmonic generation. Blue crosses: Numerical simulation, red plus-signs: Analytical comparison, Dashed black line: Analytical approximation

internal resonance issue arises, since this is when the analytical curve starts to bend in Figure 10(d). This means that if the prediction of a very large energy transfer from the fundamental to the higher harmonic is desired, a different method than the method of multiple scales should be employed to quantitatively capture the generation. This result was expected, since the method is a perturbation approach, assuming that the order ε^1 solution is much smaller than the order ε^0 solution, however the results indicate that the qualitative trend can still be captured at low energy levels. Comparing the higher harmonic generation across different loading frequencies, it appears to depend on the input energy in a very similar manner, that is, the slope of the curves are similar. The long-wave limit is seen to generate the largest higher harmonic amplitude, while the loading frequency with the higher harmonic in the band gap is seen to generate the lowest, as seen in the analytical case as well. It is noted that the linear “approximation” of the wavenumber only has a significant effect for the largest loading frequency, at the largest input energies, which is supported by the notion that the shift in wavenumber is a function of nonlinearity.

Finally, the explanation for the numerical points being below the analytical points for $\bar{\Omega} = 0.39$ is provided, along with an illustration of the limits of the analytical model. Figure 11 presents the frequency spectra for the final point in Figure 10(d) as well as for a point with an even larger input force, which was not included in the comparison, because the analytical model is clearly not representative any longer, neither is the interpretation of “input energy” as the maximal kinetic energy in the linear acoustic mode. This can be seen clearly by comparing the two spectra, where the spectrum for the higher input force actually has a lower “fundamental” harmonic amplitude, but a much wider spectrum, i.e., the energy is dispersed among a greater range of frequencies. The energy dispersion almost looks continuous, compared to Figure 11(a) where distinct frequencies

are still seen to carry the energy of the system.

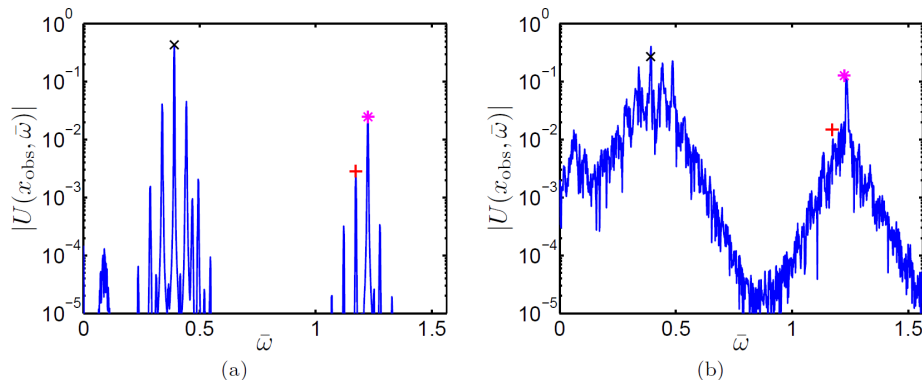


Figure 11: Frequency spectra for large input energies at $\bar{\Omega} = 0.39$. Left panel: $F_0 = 2$, right panel $F_0 = 3$.

The magenta asterisks are the limit frequencies of the optical pass band, which are points with a horizontal tangent on the dispersion curve, i.e., points with zero group velocity. This standing wave point on the dispersion curve is where the resonances of the finite system will gather since the least energy is required for motion at these wavenumbers. Hence, the spectra in Figure 11 illustrates that the energy is transferred from the higher harmonic to the nearby frequency with zero group velocity. This is actually what occurs for all the numerical simulations below the analytical predictions in Figure 10(d), which indicates the relevance of analyzing the finite system at hand rather than a constituent material.

5. Conclusions

The present paper investigates the effect of modal interaction on the dispersion of a weakly nonlinear, periodic mass-spring chain. Using the method of multiple scales, the band structure is determined, illustrating that modal interaction increases the frequency shift of the dispersion curve, in particular around the middle of the first Brillouin zone. Hence, the increase in wave-energy in the chain due to the presence of both wave-modes amplifies the intensity dependent effects in the band structure.

Furthermore, higher harmonic generation from an acoustic wave is investigated, analytically and numerically. The higher harmonic generation is seen to depend directly on the input energy as well as the strength of the nonlinearity. Moreover, it is shown that when the higher harmonic falls within a stop band, the generation is approximately one order of magnitude smaller than when it falls within a pass band. Additionally, higher harmonic generation appears to be larger in the long-wave limit. The analytical model is shown to produce reliable results at low energies, and away from internal resonance points. At internal resonance, the analytical model breaks down and predicts infinite order ε^1 response. The general accuracy of the analytical model deteriorates at lower energy levels than is required for internal resonance to occur, so the implications are not too severe. However, if one is to apply a systematic design approach based on the analytical model, this lack of robustness would be a major problem and the internal resonances must be addressed.

More generally, since internal resonance is a physical mechanism for transferring vibration energy between modes, it is of interest to develop analytical methods for capturing this effect. One approach is to consider the specific case of internal resonance in the order ε^1 equations, imposing solvability conditions to obtain the modulation equations in the internal resonance case. Different methods might be utilized, but in either case, the internal resonance issue for the investigated chain is seen to be a rather “singular” phenomena, occurring for specific wavenumber/amplitude and material parameter combinations. Determining these combinations might be of interest, but transferring the results to a finite setting could be enough of a perturbation to suppress the internal resonance. This sensitivity means that the analysis of using internal resonance as a method

of energy transfer is more suitable for specific structural systems rather than the constituent materials.

Acknowledgements

The authors were supported by ERC starting grant no. 279529 INNODYN. Furthermore, Niels M. M. Frandsen expresses his gratitude to Jon Juel Thomsen and Vladislav Sorokin for fruitful discussions on nonlinear dynamics.

- [1] L. Brillouin. *Wave Propagation in Periodic Structures*. Dover Publications, 1953.
- [2] C. Elachi. Waves in active and passive periodic structures: A review. *Proc. IEEE*, 64 (1976) 1666-1698.
- [3] D.J. Mead. Wave propagation in continuous periodic structures: Research contributions from Southampton, 1964-1995. *J. Sound Vib.*, 190(3) (1996) 495-524.
- [4] M. I. Hussein, M. J. Leamy, and M. Ruzzene. Dynamics of Phononic Materials and Structures: Historical Origins, Recent Progress, and Future Outlook. *Appl. Mech. Rev.*, 66(4) (2014) 040802.
- [5] S. Halkjær, O. Sigmund, and J. S. Jensen. Maximizing band gaps in plate structures. *Struct. Multidiscip. O.*, 32(4) (2006) 263-275.
- [6] G. Chakraborty and A. K. Mallik. Dynamics of a weakly non-linear periodic chain. *Int. J. Non-Linear Mech.*, 36 (2001) 375-389.
- [7] R. K. Narisetti, M. Ruzzene, and M. J. Leamy. A Perturbation Approach for Predicting Wave Propagation in One-Dimensional Nonlinear Periodic Structures. *Trans. ASME, J. Vib. Acoust.*, 132 (2010) 1-11.
- [8] R. K. Narisetti, M. Ruzzene, and M. J. Leamy. A perturbation approach for analyzing dispersion and group velocities in two-dimensional nonlinear periodic lattices. *Trans. ASME, J. Vib. Acoust.*, 133 (2011) 1-12.
- [9] K. L. Manktelow, M. J. Leamy, and M. Ruzzene. Multiple scales analysis of wave-wave interactions in a cubically nonlinear monoatomic chain. *Nonlinear Dyn.*, 63 (2011) 193-203.
- [10] N. Z. Swintek, K. Muralidharan, and P. A. Deymier. Phonon scattering in one-dimensional anharmonic crystals and superlattices: Analytical and numerical study. *J. Vib. Acoust.*, 135(4) (2013) 041016.
- [11] K. L. Manktelow, M. J. Leamy, and M. Ruzzene. Weakly nonlinear wave interactions in multi-degree of freedom periodic structures. *Wave Motion*, 51 (2014) 886-904 .
- [12] J. Cabaret, V. Tournat, and P. Béquin. Amplitude-dependent phononic processes in a diatomic granular chain in the weakly nonlinear regime. *Phys. Rev. E*, 86(4) (2012) 041305.
- [13] B. Yousefzadeh and A. S. Phani. Energy transmission in finite dissipative nonlinear periodic structures from excitation within a stop band. *J. Sound Vib.*, 354 (2015) 180-195.
- [14] F. Bloch. Über die quantenmechanik der elektronen in kristalgittern. *Z. Phys.*, 52 (1929) 555-600.
- [15] A. H. Nayfeh. *Introduction to Perturbation Techniques*. John Wiley and Sons, 1981.

Appendix A. Coefficient vectors

The coefficient vectors from Eq. (10) are given by

$$\mathbf{q}_1 = -i2\omega_1 \mathbf{M} \mathbf{M}^{-1/2} a'_1 \mathbf{z}_1 - 3a_1^2 \bar{a}_1 \sum_{l,m,n} \mathbf{h}_{lmn} z_1^l z_1^m \bar{z}_1^n - 6a_1 a_2 \bar{a}_2 \sum_{l,m,n} \mathbf{h}_{lmn} z_1^l z_2^m \bar{z}_2^n \quad (\text{A.1a})$$

$$\mathbf{q}_2 = -i2\omega_2 \mathbf{M} \mathbf{M}^{-1/2} a'_2 \mathbf{z}_2 - 3a_2^2 \bar{a}_2 \sum_{l,m,n} \mathbf{h}_{lmn} z_2^l z_2^m \bar{z}_2^n - 6a_2 a_1 \bar{a}_1 \sum_{l,m,n} \mathbf{h}_{lmn} z_2^l z_1^m \bar{z}_1^n \quad (\text{A.1b})$$

$$\mathbf{q}_{12} = -3a_1^2 \bar{a}_2 \sum_{l,m,n} \mathbf{h}_{lmn} z_1^l z_1^m \bar{z}_2^n, \quad \mathbf{q}_{21} = -3\bar{a}_1 a_2^2 \sum_{l,m,n} \mathbf{h}_{lmn} z_2^l z_2^m \bar{z}_1^n \quad (\text{A.1c})$$

$$\mathbf{p}_{12} = -3a_1^2 a_2 \sum_{l,m,n} \mathbf{g}_{lmn} z_1^l z_1^m z_2^n, \quad \mathbf{p}_{21} = -3a_1 a_2^2 \sum_{l,m,n} \mathbf{g}_{lmn} z_1^l z_2^m z_2^n \quad (\text{A.1d})$$

$$\mathbf{p}_1 = -a_1^3 \sum_{l,m,n} \mathbf{g}_{lmn} z_1^l z_1^m z_1^n, \quad \mathbf{p}_2 = -a_2^3 \sum_{l,m,n} \mathbf{g}_{lmn} z_2^l z_2^m z_2^n \quad (\text{A.1e})$$

The coefficient vectors \mathbf{h} and \mathbf{g} can be found in Tables A.3 and A.4 respectively.

Table A.3: Coefficient vector \mathbf{h}

l, m, n	$\mathbf{h}(1) \left[\frac{1}{m_1 m_2} \right]$	$\mathbf{h}(2) \left[\frac{1}{m_1 m_2} \right]$
1,1,1	$\frac{m_2}{\sqrt{m_1}} (\Gamma_1 + \Gamma_2)$	$-\frac{m_2}{\sqrt{m_1}} (\Gamma_1 + \Gamma_2 e^{i\mu})$
1,1,2	$-\sqrt{m_2} (\Gamma_1 + \Gamma_2 e^{i\mu})$	$\sqrt{m_2} (\Gamma_1 + \Gamma_2 e^{2i\mu})$
1,2,1	$-\sqrt{m_2} (\Gamma_1 + \Gamma_2 e^{-i\mu})$	$\sqrt{m_2} (\Gamma_1 + \Gamma_2)$
2,1,1	$-\sqrt{m_2} (\Gamma_1 + \Gamma_2 e^{-i\mu})$	$\sqrt{m_2} (\Gamma_1 + \Gamma_2)$
1,2,2	$\sqrt{m_1} (\Gamma_1 + \Gamma_2)$	$-\sqrt{m_1} (\Gamma_1 + \Gamma_2 e^{i\mu})$
2,1,2	$\sqrt{m_1} (\Gamma_1 + \Gamma_2)$	$-\sqrt{m_1} (\Gamma_1 + \Gamma_2 e^{i\mu})$
2,2,1	$\sqrt{m_1} (\Gamma_1 + \Gamma_2 e^{-2i\mu})$	$-\sqrt{m_1} (\Gamma_1 + \Gamma_2 e^{-i\mu})$
2,2,2	$-\frac{m_1}{\sqrt{m_2}} (\Gamma_1 + \Gamma_2 e^{-i\mu})$	$\frac{m_1}{\sqrt{m_2}} (\Gamma_1 + \Gamma_2)$

Table A.4: Coefficient vector \mathbf{g}

l, m, n	$\mathbf{g}(1) \left[\frac{1}{m_1 m_2} \right]$	$\mathbf{g}(2) \left[\frac{1}{m_1 m_2} \right]$
1,1,1	$\frac{m_2}{\sqrt{m_1}} (\Gamma_1 + \Gamma_2)$	$-\frac{m_2}{\sqrt{m_1}} (\Gamma_1 + \Gamma_2 e^{3i\mu})$
1,1,2	$-\sqrt{m_2} (\Gamma_1 + \Gamma_2 e^{-i\mu})$	$\sqrt{m_2} (\Gamma_1 + \Gamma_2 e^{2i\mu})$
1,2,1	$-\sqrt{m_2} (\Gamma_1 + \Gamma_2 e^{-i\mu})$	$\sqrt{m_2} (\Gamma_1 + \Gamma_2 e^{2i\mu})$
2,1,1	$-\sqrt{m_2} (\Gamma_1 + \Gamma_2 e^{-i\mu})$	$\sqrt{m_2} (\Gamma_1 + \Gamma_2 e^{2i\mu})$
1,2,2	$\sqrt{m_1} (\Gamma_1 + \Gamma_2 e^{-2i\mu})$	$-\sqrt{m_1} (\Gamma_1 + \Gamma_2 e^{i\mu})$
2,1,2	$\sqrt{m_1} (\Gamma_1 + \Gamma_2 e^{-2i\mu})$	$-\sqrt{m_1} (\Gamma_1 + \Gamma_2 e^{i\mu})$
2,2,1	$\sqrt{m_1} (\Gamma_1 + \Gamma_2 e^{-2i\mu})$	$-\sqrt{m_1} (\Gamma_1 + \Gamma_2 e^{i\mu})$
2,2,2	$-\frac{m_1}{\sqrt{m_2}} (\Gamma_1 + \Gamma_2 e^{-3i\mu})$	$\frac{m_1}{\sqrt{m_2}} (\Gamma_1 + \Gamma_2)$

Publication [P2]

Inertial Amplification in Continuous Structures: Large Band Gaps from
Small Masses

Inertial amplification of continuous structures: Large band gaps from small masses

Niels M. M. Frandsen,^{1,a)} Osama R. Bilal,^{2,b)} Jakob S. Jensen,³ and Mahmoud I. Hussein²

¹*Department of Mechanical Engineering, Section for Solid Mechanics, Technical University of Denmark, 2800 Kgs. Lyngby, Denmark*

²*Department of Aerospace Engineering Sciences, University of Colorado Boulder, Boulder, Colorado 80309, USA*

³*Department of Electrical Engineering, Centre for Acoustic-Mechanical Micro Systems, Technical University of Denmark, 2800 Kgs. Lyngby, Denmark*

(Received 12 November 2015; accepted 5 March 2016; published online 24 March 2016)

We investigate wave motion in a continuous elastic rod with a periodically attached inertial-amplification mechanism. The mechanism has properties similar to an “inertor” typically used in vehicle suspensions, however here it is constructed and utilized in a manner that alters the intrinsic properties of a continuous structure. The elastodynamic band structure of the hybrid rod-mechanism structure yields band gaps that are exceedingly wide and deep when compared to what can be obtained using standard local resonators, while still being low in frequency. With this concept, a large band gap may be realized with as much as twenty times less added mass compared to what is needed in a standard local resonator configuration. The emerging inertially enhanced continuous structure also exhibits unique qualitative features in its dispersion curves. These include the existence of a characteristic double-peak in the attenuation constant profile within gaps and the possibility of coalescence of two neighbouring gaps creating a large contiguous gap. © 2016 AIP Publishing LLC. [<http://dx.doi.org/10.1063/1.4944429>]

I. INTRODUCTION

The band structure of a material represents the relation between wave number (or wave vector) and frequency; thus it relates the spatial and temporal characteristics of wave motion in the material. This relation is of paramount importance in numerous disciplines of science and engineering such as electronics, photonics, and phononics.¹ It is well-known that periodic materials exhibit gaps in the band structure,² referred to as *band gaps* or *stop bands*. In these gaps, waves are attenuated whereby propagating waves are effectively forbidden. Their defining properties are the frequency range, i.e., position and width, as well as the depth in the imaginary part of the wave number spectrum, which describes the level of attenuation.

In the realm of elastic wave propagation, the two primary physical phenomena utilized for band-gap creation are Bragg scattering or local resonance (LR). Bragg scattering occurs due to the periodicity of a material or structure, where waves scattered at the interfaces cause coherent destructive interference, effectively cancelling the propagating waves. Research on waves in periodic structures dates back to Newton’s attempt to derive a formula for the speed of sound in air, see e.g., Chapter 1 in Ref. 2 for a historical review before the 1950s. Later review papers on wave propagation in periodic media include Refs. 3–5.

The concept of local resonance is based on the transfer of vibrational energy to a resonator, i.e., a part of the material/structure that vibrates at characteristic frequencies.

Within structural dynamics, the concept dates back, at least, to Frahm’s patent application.⁶ Since then, dynamic vibration absorbers and tuned mass dampers have been areas of extensive research within structural vibration suppression. In the field of elastic band gaps, the concept of local resonance is often considered within the framework of periodic structures, as presented in the seminal paper of Liu *et al.*,⁷ where band gaps are created for acoustic waves using periodically distributed internal resonators. The periodic distribution of the resonators does not change the local resonance effects; however, it does introduce additional Bragg scattering at higher frequencies, as well as allow for a unit-cell wave based description of the medium. Local resonance has also been used in the context of attaching resonators to a continuous structure, such as a rod,⁸ beam,⁹ or a plate^{10,11} in order to attenuate waves by creating band gaps in the low frequency range. A problem with this approach in general, which has limited proliferation to industrial applications, is that the resonators need to be rather heavy for a band gap to open up at low frequencies.

Another means for creating band gaps is by the concept of inertial amplification (IA) as proposed by Yilmaz and collaborators in Refs. 12–14. In this approach, which has received less attention in the literature, inertial forces are enhanced between two points in a structure consisting of a periodically repeated mechanism. This generates *anti-resonance* frequencies, where the enhanced inertia effectively cancels the elastic force; see e.g., Ref. 15 where two levered mass-spring systems are analysed for their performance in generating stop bands. While it is possible to enhance the inertia between two points by means of masses, springs, and levers, a specific mechanical element, *the inertor*,¹⁶ was created as the ideal inertial equivalent of

^{a)}nimmfr@mek.dtu.dk

^{b)}Currently at: Department of Mechanical and Process Engineering, ETH Zürich, Switzerland.

springs and dampers, providing a force proportional to the relative acceleration between two points. This concept, while primarily used in vehicle suspension systems,¹⁷ has been utilized in Refs. 12–14 in the context of generating band gaps in lattice materials by inertial amplification where the same underlying physical phenomenon is used for generating the anti-resonance frequencies. The frequency responses to various harmonic loadings were obtained, numerically and experimentally, and low-frequency, wide and deep band gaps were indeed observed for these novel lattice structures. In Ref. 18, size and shape optimization is shown to increase the band gap width further, as illustrated by a frequency-domain investigation.

Until now, both inerters and inertial amplification mechanisms have been used as a backbone structural component in discrete or continuous systems. In this paper, we propose to use inertial amplification to generate band gaps in conventional continuous structures, by attaching light-weight mechanisms to a host structure, such as a rod, beam, plate, or membrane, without disrupting its continuous nature (therefore not obstructing its main structural integrity and functionality). With this approach, we envision the inertial amplification effect to be potentially realized in the form of a *surface coating*, to be used for sound and vibration control.

For proof of concept, we consider a simple one-dimensional case by analyzing an elastic rod, with an inertial amplification mechanism periodically attached. The mechanism is inspired by that analyzed in Ref. 12; however, the application to a continuous structure increases the practicality and richness of the problem considerably and several intriguing effects are illustrated.

Our investigation focuses mainly on the unit-cell band-structure characteristics. However, we also compare our findings from the analysis of the material problem to transmissibility results for structures comprising a finite number of unit cells. The finite systems are modelled by the finite-element (FE) method.

II. MODEL

In order to utilize the concept of inertial amplification in a surface setting as proposed, the mechanisms should be much smaller than the host structure such that their distributed attachment does not change the main function of the structure, nor occupy a significant amount of space. Fulfilling this constraint requires a relatively large effect with only a modest increase in mass.

Considering the ideal mechanical element, the inerter, we know that the factor of proportionality, the inertance, can be much larger than the actual mass increase, as demonstrated experimentally in Refs. 16 and 19. We propose to utilize the same effect using a mechanism similar to the one considered in Refs. 12 and 14. Our two-dimensional interpretation of the system is seen in Fig. 1, illustrating the comparably small inertial amplification mechanisms distributed over the host-structure. In principle, the distributed effect of the mechanisms, in the long wave-limit, reduces to the notion of an inertially modified constitutive relation in the elastodynamic equations.

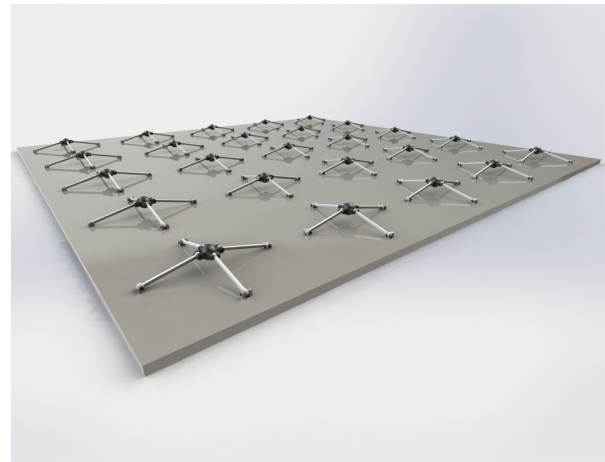


FIG. 1. General 2D realization of the proposed inertially amplified system.

A. Model reduction

In this study, we restrict ourselves to a one-dimensional structure with an inertial amplification mechanism attached, as illustrated in Fig. 2, where the mechanism is attached to the rod with bearings. A similar bearing is used at the top connection such that, ideally, no moment is transferred through the mechanism. This ensures that the connecting links do not deform, but move the amplification mass by rigid-body motion. The 1D-system is simplified further to a hybrid model consisting of a continuous, elastic bar and a discrete mechanism as seen in Fig. 3, as this allows for a rigorous analytical formulation for the underlying dynamics.

The bar has Young's modulus E , cross-sectional area A , mass density ρ , and unit-cell length $l = l_1 + l_2 + l_3$, while the amplification mass is denoted m_a and θ is the amplification angle. In Fig. 3, heavy lines indicate rigid connections and the corners between vertical and inclined rigid connections are moment-free hinges; hence, the motion of the amplification mass quantified by $z_1(t)$ and $z_2(t)$ is governed by the motion at the attachment points $u(x_1, t)$, $u(x_2, t)$ and the amplification angle θ , where $x_1 = l_1$ and $x_2 = l_1 + l_2$. From a physical standpoint, any increase in static stiffness of the mechanism would arise from frictional stiffness in the bearings or at the top point; however, it is outside the scope of this work to include these residual stiffness effects, among other things, since they are assumed to be small.

The inertial amplification model in Fig. 3 assumes rigid connections between the rod and the mechanism. Should the connections be flexible as illustrated in Fig. 4, the unit cell may be tuned to respond as either a locally resonant or an inertially amplified medium, depending on the specific system parameters. With the flexible springs, the two additional

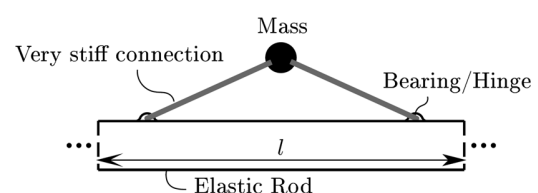


FIG. 2. 1D version of the proposed concept.

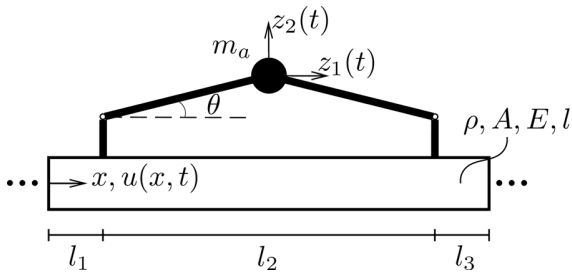


FIG. 3. Hybrid continuous-discrete model.

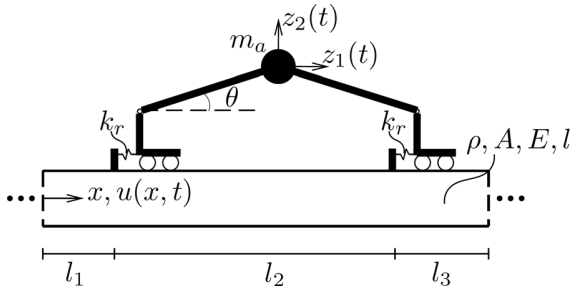


FIG. 4. Hybrid model including connection flexibility.

degrees of freedom introduced by the general mechanism create two local resonances which open up two LR-hybridization gaps. The IA mechanism on the other hand, being fixed to the host structure, does not add any additional degrees of freedom. Instead, it alters the intrinsic properties of the material and introduces anti-resonance frequencies throughout the entire frequency range. The LR type system recovers the ideal inertial amplification system for $k_r \rightarrow \infty$, and a standard local resonance system is realized when $l_2 = 0$.

The inertial amplification system in Fig. 3 is the main system investigated in this paper, while the system including the connection flexibility is used to investigate the transition between the fundamentally different types of gap generation possible for the general rod-mechanism configuration.

All the analytical formulations in this paper are based on the differential equation of a rod

$$\rho \ddot{u}(x, t) = \sigma'(x, t) + f(x, t), \quad (1)$$

where $u(x, t)$ is the longitudinal displacement and $\sigma(x, t)$ is the normal stress while $(\dot{}) = \partial^2()/\partial t^2$ and $()' = \partial()/\partial x$. The body force $f(x, t)$ will not be present in the material problem formulation considering infinite domains. The rod is considered to be homogeneous; however, a layered rod would pose no additional difficulty in terms of the transfer matrix method described in Section III B, since the method is applicable to layered materials.²⁰⁻²² The rod is further assumed to be linear elastic with infinitesimal strains, which provides the constitutive relation

$$\sigma(x, t) = E\varepsilon(x, t) = Eu'(x, t), \quad (2)$$

where $\varepsilon(x, t)$ is the longitudinal strain in the rod.

B. Mechanism equations

Before considering the hybrid systems in Figs. 3 and 4, the mechanisms are considered with constraint forces

applied to account for the rod. These constraint forces are determined in terms of the mechanism parameters, whereby the effect of the mechanism on the rod is given in terms of these constraint forces.

1. Kinematics

Considering the isolated inertial amplification mechanism in Fig. 5, the motions z_1 and z_2 can be determined in terms of y_1, y_2 , and θ . In the Appendix, the full non-linear kinematic relations are derived. In this paper, we consider the linearized version, whereby z_1 and z_2 are determined as

$$z_1 = \frac{1}{2}(y_2 + y_1), \quad (3a)$$

$$z_2 = \frac{1}{2} \cot\theta(y_2 - y_1), \quad (3b)$$

as seen in Ref. 12 as well.

2. Constraint forces

Considering the inertial amplification mechanism in Fig. 5, with the applied constraint forces P_1 and P_2 , the motions y_1 and y_2 correspond to longitudinal motion of the rod at the points x_1 and x_2 . Using Lagrange's equations, the governing equations for the mechanism are found

$$m_1 \ddot{y}_1 - m_2 \ddot{y}_2 = P_1, \quad (4a)$$

$$m_1 \ddot{y}_2 - m_2 \ddot{y}_1 = P_2, \quad (4b)$$

where $m_1 = \frac{m_a}{4}(\cot^2\theta + 1)$ and $m_2 = \frac{m_a}{4}(\cot^2\theta - 1)$. Assuming harmonic motion, $y_j = Y_j e^{i\omega t}$, we obtain

$$k_1(\omega)Y_1 - k_2(\omega)Y_2 = \hat{P}_1(\omega), \quad (5a)$$

$$k_1(\omega)Y_2 - k_2(\omega)Y_1 = \hat{P}_2(\omega), \quad (5b)$$

where \hat{P}_j are the frequency domain representations of P_j and the dynamic stiffness parameters $k_j(\omega)$ are defined as

$$k_j(\omega) = -\omega^2 m_j, \quad j = 1, 2. \quad (6)$$

Next, the constraint forces for the system with flexible connections in Fig. 4 are determined. Considering the isolated mechanism in Fig. 6, the constraint forces are applied at the constrained coordinates v_1 and v_2 , while the coordinates y_1 and y_2 are free.

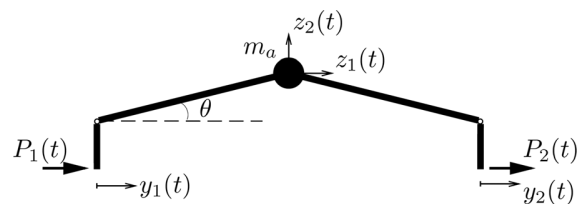


FIG. 5. IA mechanism with constraint forces.

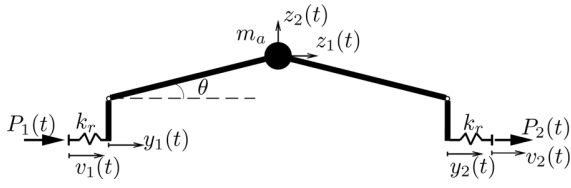


FIG. 6. LR mechanism with constraint forces.

The governing equations are found by Lagrange's equations

$$k_r(v_1 - y_1) = P_1, \quad (7a)$$

$$m_1\ddot{y}_1 + k_r y_1 - m_2\ddot{y}_2 - k_r v_1 = 0, \quad (7b)$$

$$m_1\ddot{y}_2 + k_r y_2 - m_2\ddot{y}_1 - k_r v_2 = 0, \quad (7c)$$

$$k_r(v_2 - y_2) = P_2. \quad (7d)$$

Assuming harmonic motion provides the frequency domain constraint forces, which in terms of the constraint coordinates V_1 and V_2 are

$$k_1^{lr}(\omega)V_1 - k_2^{lr}(\omega)V_2 = \tilde{P}_1(\omega), \quad (8a)$$

$$k_1^{lr}(\omega)V_2 - k_2^{lr}(\omega)V_1 = \tilde{P}_2(\omega), \quad (8b)$$

with the dynamic stiffness parameters defined as

$$k_1^{lr}(\omega) = \frac{\omega^2 \omega_{lr,1}^2 (\omega^2 (m_1 + m_2) - \omega_{lr,2}^2 m_1)}{(\omega_{lr,1}^2 - \omega^2)(\omega_{lr,2}^2 - \omega^2)}, \quad (9a)$$

$$k_2^{lr}(\omega) = \frac{-\omega^2 \omega_{lr,1}^2 \omega_{lr,2}^2 m_2}{(\omega_{lr,1}^2 - \omega^2)(\omega_{lr,2}^2 - \omega^2)}, \quad (9b)$$

where $\omega_{lr,1}$ and $\omega_{lr,2}$ are the local resonance frequencies defined by

$$\omega_{lr,1} = \sqrt{\frac{k_r}{m_1 + m_2}} = \sqrt{\frac{2k_r}{m_a \cot^2 \theta}}, \quad (10a)$$

$$\omega_{lr,2} = \sqrt{\frac{k_r}{m_1 - m_2}} = \sqrt{\frac{2k_r}{m_a}}. \quad (10b)$$

Eq. (10a) corresponds to the out-of-phase mode, while Eq. (10b) corresponds to the in-phase mode of the mechanism. It is noted that the dynamic stiffness coefficients for the inertial amplification system are recovered from Eq. (9) when $k_r \rightarrow \infty$.

III. ANALYSIS

In order to characterize the effects of the inertial amplification mechanism, the band structure of an infinite array

of hybrid rod-mechanism systems is determined using the transfer-matrix method. The method has its origins within electrodynamics and optics,²⁰ but has been widely used within elastic wave propagation.^{21,22} The method is briefly described in Section III B, with a focus on the specific extension required for the particular unit cell considered here. Before describing the general transfer-matrix methodology, we consider a simplified unit cell in Section III A in order to shed light on the band-opening mechanism. We do this by a *receptance approach*,²³ where we determine the displacement at one end of a single unit cell when applying harmonic forcing at the other end. The anti-resonance frequencies can then be determined as those frequencies with zero receptance for any forcing magnitude (zeros). These anti-resonance frequencies are shown to be the points of maximum attenuation in the infinite system, and are thus relevant quantities for maximum attenuation design.

A. Receptance approach

Consider the simplified rod-mechanism system in Fig. 3 with free boundary conditions, $l_1 = l_3 = 0$, and harmonic forcing, $F = F_0 e^{i\omega t}$, at $x = 0$. Both the applied and constraint forces can be included via the boundary conditions to the rod differential equation, Eq. (1). With harmonic forcing, the linear response will be harmonic, $u(x, t) = \bar{u}(x) e^{i\omega t}$, whereby

$$\bar{u}''(x) + \kappa_b^2 \bar{u}(x) = 0, \quad \kappa_b = \frac{\omega}{c_0}, \quad (11)$$

with wave number κ_b and wave-speed $c_0 = \sqrt{E/\rho}$ in the homogeneous rod. The solution to (11) is

$$\bar{u}(x) = \alpha \sin \kappa_b x + \beta \cos \kappa_b x, \quad (12)$$

where the constants α and β are determined by the boundary conditions, given by force equilibria at both ends. Utilizing the constitutive relation $\bar{\sigma}(x) = E\bar{u}'(x)$, the force equilibria yield

$$x = 0: \quad EA\bar{u}'(0) = F_0 - \hat{P}_1(\omega), \quad (13a)$$

$$x = l: \quad EA\bar{u}'(l) = -\hat{P}_2(\omega), \quad (13b)$$

which, when inserting the constraint forces from Eq. (5) and the solution $\bar{u}(x)$ from Eq. (12), is expressed in matrix form

$$\begin{bmatrix} 1 - \hat{k}_2 \sin \kappa_b l & \hat{k}_1 - \hat{k}_2 \cos \kappa_b l \\ \cos \kappa_b l + \hat{k}_1 \sin \kappa_b l & \hat{k}_1 \cos \kappa_b - \sin \kappa_b l - \hat{k}_2 \end{bmatrix} \mathbf{x} = \mathbf{f}, \quad (14)$$

with $\hat{k}_i = k_i(\omega)/(EA\kappa_b)$, $\mathbf{x} = [\alpha \beta]^T$, and $\mathbf{f} = [F_0/(EA\kappa_b) 0]^T$. Solving for α and β provides the solution for $\bar{u}(x)$

$$\bar{u}(x) = \frac{((\sin \kappa_b l - \hat{k}_1 \cos \kappa_b l + \hat{k}_2) \sin \kappa_b x + (\cos \kappa_b l + \hat{k}_1 \sin \kappa_b l) \cos \kappa_b x)}{\sin \kappa_b l (1 + \hat{k}_1^2 - \hat{k}_2^2) EA \kappa_b} F_0 = H_{0x}(\omega) F_0, \quad (15)$$

where $H_{0x}(\omega)$ is the receptance function. The displacement at $x = l$ is given by

$$\bar{u}(l) = \frac{1 + \hat{k}_2 \sin \kappa_b l}{\sin \kappa_b l (1 + \hat{k}_1^2 - \hat{k}_2^2) EA \kappa_b} F_0 = H_{0l}(\omega) F_0, \quad (16)$$

whereby the anti-resonance frequencies can be determined as the frequencies satisfying $H_{0l}(\omega) = 0$, i.e.,

$$k_2(\omega) \sin \kappa_b l + EA \kappa_b = 0. \quad (17)$$

This transcendental equation is solved numerically for any desired number of anti-resonance frequencies. The approximation for the first anti-resonance frequency is found in the long-wavelength limit where $\sin \kappa_b l \approx \kappa_b l$, i.e., in the sub-Bragg regime. The approximation $\tilde{\omega}_{a,1}$ is

$$-\omega^2 m_2 \kappa_b l + EA \kappa_b = 0 \Rightarrow \tilde{\omega}_{a,1} = \sqrt{\frac{EA/l}{m_2}} = \sqrt{\frac{EA/l}{m_a (\cot^2 \theta - 1)/4}}, \quad (18)$$

which is essentially the same as the anti-resonance frequency of a discrete system as presented in Ref. 12 with effective spring stiffness $k = EA/l$. Hence, discretizing the rod as a spring-mass system would provide the semi-infinite gap presented in the mentioned reference. The added complexity from the rod is illustrated by the higher roots of Eq. (17) and will be apparent from the band structures calculated in Section IV.

B. Transfer matrix method

The transfer matrix method is based on relating the state variables of a system across distances and interfaces, successively creating a matrix product from all the “sub” transfer matrices, forming the *cumulative transfer matrix*.

Consider the hybrid continuous-discrete, rod-mechanism system illustrated in Fig. 3, where the rod is modelled as a continuum and the mechanism is modelled by discrete elements. The transfer matrix for the unit cell is based on the host medium, i.e., the rod, representing the effects of the mechanisms by point force matrices at x_1 and x_2 . The state variables for the rod are the longitudinal displacement $u(x, t)$ and the normal stress $\sigma(x, t)$. Dividing the system into three layers separated at x_1 and x_2 , the solution for the longitudinal displacement in layer j can be written as a sum of forward and backward travelling waves

$$u_j(x, t) = (B_j^{(+)} e^{i\kappa_b x} + B_j^{(-)} e^{-i\kappa_b x}) e^{i\omega t}, \quad (19)$$

where $B_j^{(+)}$ and $B_j^{(-)}$ are the amplitudes of the forward and backward travelling waves. Using the linear elastic constitutive relation for the stress, the state variables are expressed as

$$\mathbf{z}_j(x) = \begin{bmatrix} u_j(x) \\ \sigma_j(x) \end{bmatrix} = \begin{bmatrix} 1 & 1 \\ Z & -Z \end{bmatrix} \begin{bmatrix} B_j^{(+)} e^{i\kappa_b x} \\ B_j^{(-)} e^{-i\kappa_b x} \end{bmatrix} = \mathbf{H} \begin{bmatrix} B_j^{(+)} e^{i\kappa_b x} \\ B_j^{(-)} e^{-i\kappa_b x} \end{bmatrix}, \quad (20)$$

thus defining the **H**-matrix, where $Z = iE\kappa_b$. Relating the state variables at either end of a homogeneous layer separated by the distance l_j yields

$$\mathbf{z}_j^R = \mathbf{H} \begin{bmatrix} e^{i\kappa_b l_j} & 0 \\ 0 & e^{-i\kappa_b l_j} \end{bmatrix} \begin{bmatrix} B_j^{(+)} e^{i\kappa_b x^{jL}} \\ B_j^{(-)} e^{-i\kappa_b x^{jL}} \end{bmatrix} = \mathbf{H} \mathbf{D}_j \begin{bmatrix} B_j^{(+)} e^{i\kappa_b x^{jL}} \\ B_j^{(-)} e^{-i\kappa_b x^{jL}} \end{bmatrix}, \quad (21)$$

defining the “phase-matrix” **D**_{*j*}. The coordinate at the left end of layer j is denoted x^{jL} . Solving Eq. (20) with $\mathbf{z}_j = \mathbf{z}_j^L$ for the vector of amplitudes and inserting into Eq. (21) define the transfer matrix for layer j

$$\mathbf{z}_j^R = \mathbf{H} \mathbf{D}_j \mathbf{H}^{-1} \mathbf{z}_j^L = \mathbf{T}_j \mathbf{z}_j^L \quad \mathbf{T}_j = \begin{bmatrix} \cos \kappa_b l_j & \frac{1}{E\kappa_b} \sin \kappa_b l_j \\ -E\kappa_b \sin \kappa_b l_j & \cos \kappa_b l_j \end{bmatrix}. \quad (22)$$

Having defined the transfer matrices **T**_{*j*}, $j = 1, 2, 3$, we turn to the constraint forces at the attachment points of the mechanism.

We base our derivation of the point force matrices on a frequency domain force equilibrium at the attachment points, considering x_1 first

$$A\sigma_2^L = A\sigma_1^R + \hat{P}_1 = A\sigma_1^R + k_1(\omega)u_1^R - k_2(\omega)u_2^R. \quad (23)$$

It is noted that the force balance at point x_1 depends on the displacement at x_2 . Using the transfer matrix for layer 2, u_2^R is expressed as

$$u_2^R = u_2^L \cos \kappa_b l_2 + \frac{\sigma_2^L}{E\kappa_b} \sin \kappa_b l_2, \quad (24)$$

which, along with the continuity requirement $u_1^R = u_2^L$, yields the force equilibrium

$$\left(A + \frac{k_2(\omega)}{E\kappa_b} \sin \kappa_b l_2 \right) \sigma_2^L = A\sigma_1^R + (k_1(\omega) - k_2(\omega) \cos \kappa_b l_2) u_1^R, \quad (25)$$

whereby the point force matrix, relating the state vector \mathbf{z}_2^L to \mathbf{z}_1^R , can be identified

$$\mathbf{z}_2^L = \begin{bmatrix} 1 & 0 \\ \frac{E\kappa_b(k_1(\omega) - k_2(\omega) \cos \kappa_b l_2)}{AE\kappa_b + k_2(\omega) \sin \kappa_b l_2} & \frac{AE\kappa_b}{AE\kappa_b + k_2(\omega) \sin \kappa_b l_2} \end{bmatrix} \times \mathbf{z}_1^R = \hat{\mathbf{P}}_1 \mathbf{z}_1^R. \quad (26)$$

Using a similar approach at point x_2 provides the point force matrix $\hat{\mathbf{P}}_2$ as

$$\hat{\mathbf{P}}_2 = \begin{bmatrix} 1 & 0 \\ \frac{k_1(\omega) - k_2(\omega) \cos \kappa_b l_2}{A} & 1 + \frac{k_2(\omega)}{AE\kappa_b} \sin \kappa_b l_2 \end{bmatrix}, \quad (27)$$

which allows for relating the state vector at the right end of the unit cell to the state vector at the left end through the cumulative transfer matrix \mathbf{T}

$$\mathbf{z}_3^R = \mathbf{T}_3 \hat{\mathbf{P}}_2 \mathbf{T}_2 \hat{\mathbf{P}}_1 \mathbf{T}_1 \mathbf{z}_1^L = \mathbf{T} \mathbf{z}_1^L. \quad (28)$$

The present framework is fully compatible with the local-resonator-type system described in Section II by changing the dynamic stiffness parameters in the point-force matrices to those of Eq. (9), rather than those defined by Eq. (5). Finally, it is noted that when the internal distance l_2 approaches zero, the point force matrices for the inertial amplification system approach that of an attached point mass, while the local-resonance point force matrices approach that of an attached local resonator with resonance frequency $\omega_{lr,2} = \sqrt{2k_r/m_a}$, recovering the expected limits.

With the cumulative transfer matrix for a unit cell determined, the Floquet-Bloch theorem for periodic structures²⁴ is used to relate the state vector at either end through a phase multiplier

$$\mathbf{z}_3^R = \mathbf{z}_1^L e^{i\kappa l}, \quad (29)$$

where $\kappa = \kappa(\omega)$ is the wave number for the periodic material and l is the unit-cell length. Combining Eqs. (28) and (29) yields a frequency-dependent eigenvalue problem in $e^{i\kappa l}$

$$(\mathbf{T} - e^{i\kappa l} \mathbf{I}) \mathbf{z}_1^L = 0, \quad (30)$$

whereby the band structure of our periodic material system is determined within a $\kappa(\omega)$ -formulation.

IV. BAND STRUCTURE

In this section, the band structure is calculated for the systems in Figs. 3 and 4 as well as a standard local resonator configuration, with primary focus on the inertial amplification system. The mechanism is attached to an aluminum rod with Young’s modulus E , density ρ , width b , height h , and length l . These parameters are given in Table I along with the equivalent mass and stiffness parameters m_b and k_b and the first natural frequency ω_b .

The effect of the primary parameters of the system is investigated, with special attention devoted to gap width and depth. We begin by considering the case where the internal length of the mechanism is equal to the unit-cell length, i.e., $l_1 = l_3 = 0$, illustrating the effect of the added mass m_a , after which we consider the effect of reducing the mechanism size compared to the unit-cell length. Next, we consider the system with flexible connections and the transition from local resonance to ideal inertial amplification, after which we compare the performance of the IA system to that of a

TABLE I. Parameters of the host rod.

E (GPa)	ρ (kg/m ³)	$b \times h$ (m) \times (m)	l (m)	ω_b (rad/s)	m_b (kg)	k_b (N/m)
69.8	2700	0.025×0.025	0.55	$\frac{\pi}{l} \sqrt{\frac{E}{\rho}}$	$\rho A l$	$\frac{EA}{l}$

TABLE II. Reference mechanism parameters.

m_a	θ	l_2
$m_b/10$	$\pi/18$	l

standard local resonator system where the resonator is attached to the rod at a point within the unit cell.

A. Band structure and anti-resonance frequencies

We begin by considering a reference case, with the rod parameters in Table I and the mechanism parameters given in Table II.

For the reference case, the anti-resonance frequencies are predicted by numerically solving Eq. (17), while the band structure is calculated using the transfer-matrix method described in Sec. III B. Figure 7 shows the band structure with the anti-resonance frequencies indicated by red crosses, in the normalized frequency range $\bar{\omega} = \omega/\omega_b$.

It is clear that the solution of Eq. (17) predicts the peak values of the imaginary part of the wave number. A feature unique to inertial amplification seen in the band structure in Fig. 7 is the appearance of two peaks within the odd-numbered gaps that are noted to have merged with the odd-numbered Bragg gaps with upper limits at $\bar{\omega} = 1, 3, 5, \dots$. This double-peak behaviour is previously observed in Refs. 14 and 15, however, in the frequency response functions of finite structures rather than the band structure of the system. The reason that the inertial amplification gaps and Bragg gaps merge is the fact that the mechanism is attached to the ends of the unit cell; hence, the wavelengths most significant for activation of the inertial amplification mechanism are the same as those relevant for Bragg scattering. The number of attenuation peaks within a band gap is determined by the number of anti-resonance frequencies separating the two wave modes on either side of the gap. Hence when two resonance frequencies (poles) are separated by more than one anti-resonance frequency (zero), multiple attenuation peaks will occur. The low-pass filters shown in Ref. 15 are designed such that all

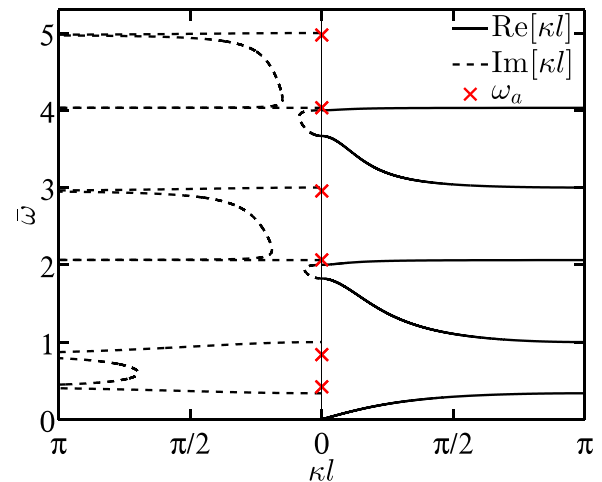


FIG. 7. Band-structure for reference case.

the anti-resonance frequencies are larger than the largest resonance frequency, whereby the multiple peaks are all found above the filter frequency. It is further noted that the even gaps are of Bragg-type; however, they exhibit an asymmetry, being distorted towards the double-peak gaps which is also common when Bragg gaps are close to the peak of local-resonance gaps.^{25,26}

When considering the band structure for increasing frequency, it appears that for higher band gaps, the anti-resonance frequencies get further separated, increasing the gap width at the cost of decreasing the gap depth. Furthermore, as the gap widens, the anti-resonance frequencies approach the gap limits. This indicates that the anti-resonance frequencies can be used as a design-parameter for gap width. This is investigated further in the Sec. IV C, where it is shown that this is only strictly true for “full-length” mechanisms, i.e., when $l_1 = l_3 = 0$.

B. Mass variation

Consider the model shown in Fig. 3 with $l_1 = l_3 = 0$. We investigate the effect of the attached mass m_a for the general rod parameters in Table I and the mechanism parameters in Table II. It is expected that increasing the attached mass will increase the gap width as well as decrease the frequency range. These effects are illustrated for distinct values of the mass ratio $\mu = m_a/m_b$ in Fig. 8(a) as well as by the attenuation profile in Fig. 8(b) which in this paper refers to a contour plot of the natural logarithm of the imaginary part of the normalized wave number. The four band structures in Fig. 8(a) are for the μ -values indicated by the four vertical dashed lines in the attenuation profile in Fig. 8(b). It is noted that for the mass ratio $\mu = 5\%$, the first gap is purely of Bragg-type since the inertial forces generated by the mechanism are not sufficient to generate anti-resonance frequencies, i.e., to fulfil Eq. (17). As μ is increased, the inertial forces are increased (by a factor of m_a), and $\mu = 7\%$ is seen to be the limiting value for generating true anti-resonance frequencies in the first gap. At this value, we see a single

anti-resonance frequency which branches into two distinct anti-resonance frequencies as μ is further increased.

Aside from this double-peak behaviour, the width of the first gap is rather wide for relatively low mass-ratios, e.g., for a mass ratio of 10% we have a normalized first gap width of

$$\Delta\bar{\omega}_1 = \frac{\bar{\omega}_1^u - \bar{\omega}_1^l}{\bar{\omega}_1^c} = 99\%, \tag{31}$$

which, compared to gaps obtained by standard LR effects, is rather wide, as will be shown in Sec. IV E. The attenuation profile in Fig. 8(b) illustrates the continuous progression of the band gaps as the mass varies. Regions with color indicate band gaps and the color bar represents the magnitude of attenuation as a function of μ and $\bar{\omega}$. The logarithmic scale illustrates the order of magnitude of the gap depth. Between the peak values at the anti-resonances, the attenuation is seen to stay at a relatively high level, a level that decreases with gap-width as observed for increasing gap number in Section IV A.

C. Effect of attachment points

Investigating the effect of the relative mechanism length $\bar{l} = l_2/l$, it is expected that the performance metrics, i.e., the gap width and depth, of the mechanism will decrease with a smaller internal length due to the decreased lever-arm for the mass. This, however, is not a trivial investigation because decreasing the mechanism size can provide new ways for gaps to hybridize, e.g., the even-numbered wave-modes will be affected by the mechanism. Figure 9 illustrates the effect of varying the relative attachment length, $\bar{l} = l_2/l$, with four band diagrams in Fig. 9(a) and the attenuation profile in Fig. 9(b), for the general rod parameters in Table I and the mechanism parameters from Table II. The four band structures in Fig. 9(a) correspond to the vertical dashed lines in the attenuation profile in Fig. 9(b). Considering the attenuation profile first, the first striking feature is the multitude of coalescence

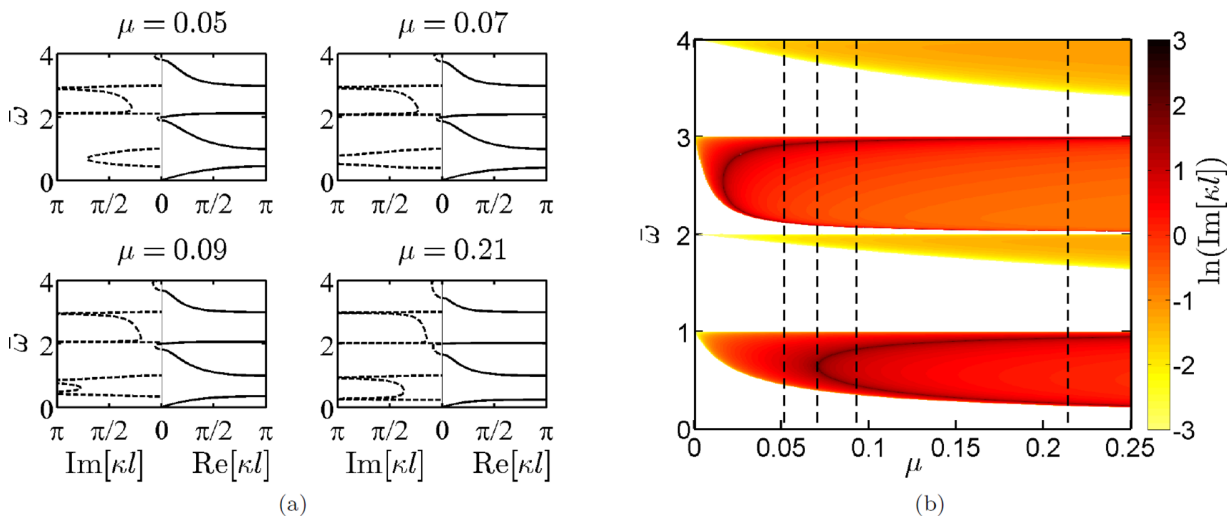


FIG. 8. Effect of amplification mass for full length mechanism. (a) Band structures. (b) Attenuation profile showing the normalized imaginary wave number in logarithmic scale.

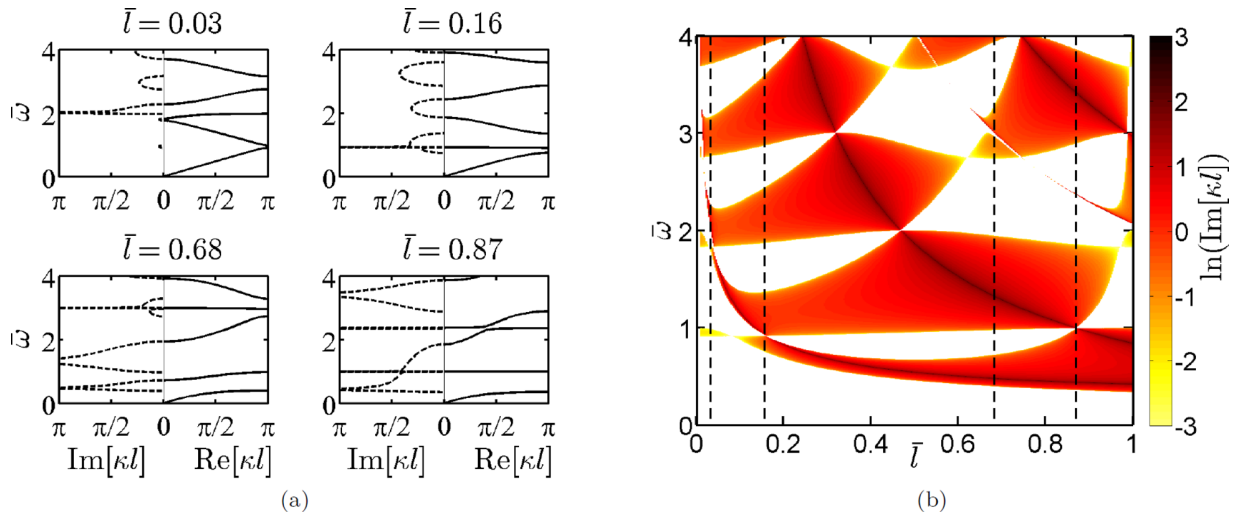


FIG. 9. Effect of decreasing $\bar{l} = l_2/l_1$. $\theta = \pi/18$, $\mu = 0.1$. (a) Band structures. (b) Attenuation profile.

points between the gaps, where the anti-resonance frequencies jump from one gap to another. At these coalescence points, the gap width is effectively increased to the sum of the two coalescent gaps, e.g., at $\bar{l} = 87\%$, we get an effective, normalized gap width of $\Delta\bar{\omega} = 136\%$. The corresponding band-structure illustrates that the two gaps do not coalesce completely, rather there is a standing-wave mode separating the two gaps. Hence, the second anti-resonance frequency is in fact larger than the second resonance frequency, whereby the first gap only contains one anti-resonance frequency. This indicates the presence of a *critical region* between the gap limits, especially for practical designs where design inaccuracies will make an exact realization of, for example, $\bar{l} = 87\%$ difficult. The three remaining band structures, at $\bar{l} = 3\%$, 16% , and 68% , respectively, illustrate various effects. The first of these illustrates the limiting behaviour towards the pure Bragg gaps from periodically attached masses when $\bar{l} \rightarrow 0$. It is noted that this transition occurs earlier for lower gaps, due to the shorter wavelengths of the higher gaps. The $\bar{l} = 16\%$ band structure illustrates the first coalescence point between the first and second gap, the effect of which is not quite as powerful as for the $\bar{l} = 87\%$ case; however, this can be explained by the smaller lever ratio, thus providing smaller inertial forces. The band-structure for $\bar{l} = 68\%$ illustrates the first two distinct gaps, as well as a Bragg-type gap which is virtually unaffected by the anti-resonance frequency very close to it.

D. Transition from local resonance

In this section, we illustrate how the behaviour of the general local-resonator-type system illustrated in Fig. 4 tends toward that of the pure inertial amplification mechanism as the connection stiffness increases, $k_r \rightarrow \infty$. The local resonance frequencies seen in Eq. (10) are for the two modes supported by the mechanism, i.e., where the mechanism ends move out-of-phase and in-phase, respectively. Figure 10 shows the attenuation profile for increasing the relative connection stiffness $\bar{k}_r = k_r/k_b$, both in a low range to illustrate the local-resonance effect and a larger range to illustrate the limiting behaviour. The dash-dot lines are the resonance frequencies

for the local resonance-system predicted by Eq. (10), noted to follow gap limits, rather than peak attenuation points, as is the case for a standard local resonator attached at a point. This has a rather simple physical explanation when considering the working principle of the two types of systems. At their specific resonance frequencies, both resonators are maximally activated, but the fundamental difference lies in the number of attachment points. While the standard local resonator will “take out” some of the mechanical energy of the travelling wave, the two-terminal system will work as a path of travel for the wave whereby the mechanical energy is not “deposited” as in the standard local resonator case. Hence, the peak attenuation frequency for the system including connection flexibility should be predicted from the anti-resonance equation, Eq. (17), but with the dynamic stiffness coefficient given by Eq. (9b), $k_2 = k_2^l$. The black horizontal lines in Fig. 10(b) are the anti-resonance frequencies predicted by Eq. (17) using the IA dynamic stiffness coefficient, $k_2 = -\omega^2 m_2$, in which the peak attenuation lines can be seen to converge towards, starting at the lower frequencies. Hence, as the connection stiffness increases, the lower gaps become dominated by inertial amplification effects, followed by the higher gaps. This is illustrated further by considering the band structures corresponding to the vertical dashed lines in Figs. 10(a) and 10(b). In the low-stiffness limit in Fig. 10(c), we see a behaviour that is similar to what is observed for classical local resonance; however, we know that the local resonance frequency actually represents the upper limit of the gap. The peak attenuation frequency however is the anti-resonance frequency, where energy *cannot* be transferred through the mechanism. In the high-stiffness limit in Fig. 10(d), we observe the ideal inertial amplification behaviour (where we have two anti-resonance frequencies separating the first and second wave modes leading to the appearance of the characteristic double peak).

E. Comparison to a standard local resonator

The performance metrics are now investigated for a rod with periodic, point-wise attached local resonators, in order

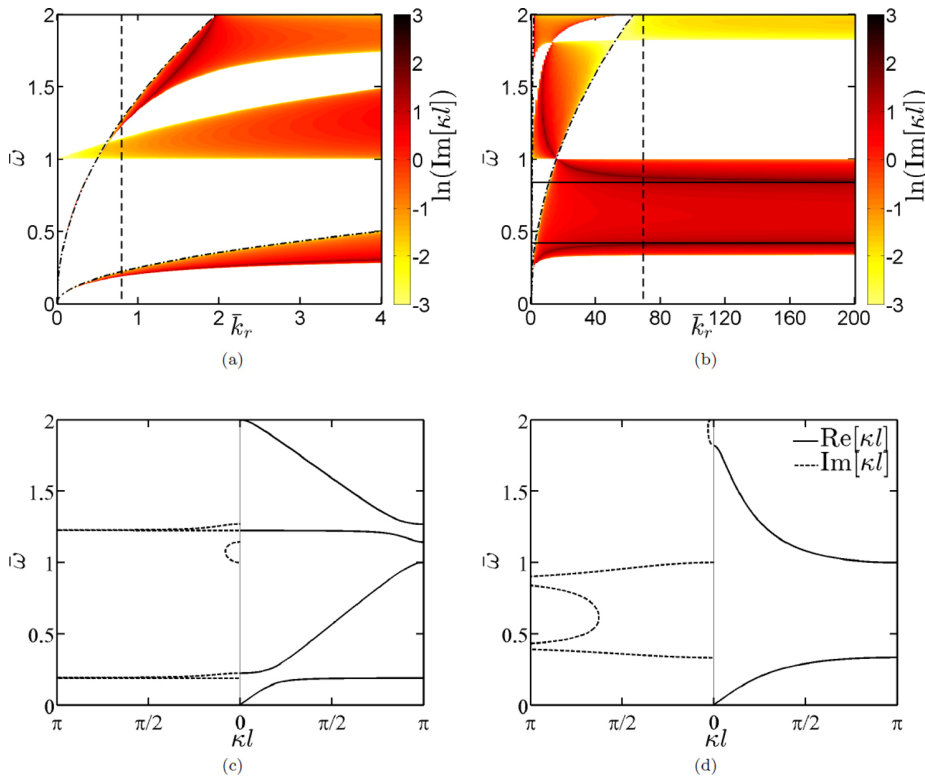


FIG. 10. Effect of connection stiffness $\bar{\kappa}_r = k_r/k_b$, $\theta = \pi/18$, $\mu = 0.1$, $\bar{l} = 1$. (a) Attenuation profile in a low range. (b) Attenuation profile in a wide range. (c) Band structure for $\bar{\kappa}_r = 0.8$ (local resonance). (d) Band structure for $\bar{\kappa}_r = 69.3$ (inertial amplification).

to provide a direct performance comparison with the proposed inertial amplification system. The transfer matrix of such a rod is known and given in, e.g., Ref. 27. One strength of the classical local resonator configuration is the ability to create *any* anti-resonance frequency, given complete freedom in the design variables. This is equally possible for the inertial amplification configuration proposed here, which is evident from the anti-resonance equation, Eq. (17). Hence, the local resonator offers no design flexibility advantage over the inertial amplification mechanism in this regard. A primary parameter for both the inertial-amplification and local-resonator systems is the added mass m_a . The effect of the added mass is illustrated for the local-resonator system

for two tuning cases of local resonator stiffness, k_{eq} . One is where the local-resonance frequency is tuned to the approximate first anti-resonance frequency for the inertial amplification system, $\bar{\omega}_{1,a}$ from Eq. (18), in order to attain the same peak attenuation frequency for the two systems. The second case is where the local resonator system is tuned to allow the local-resonance gap to coalesce with the first Bragg gap-since; it is known that this is where local resonance gaps achieve maximal width.^{25,27,28} Fig. 11 illustrates the effect of increasing the mass ratio μ for the two cases. The attenuation profile seen in Fig. 11(a) illustrates how the local-resonance gap decreases in frequency range with increasing mass, while the Bragg gaps stay centred around the same

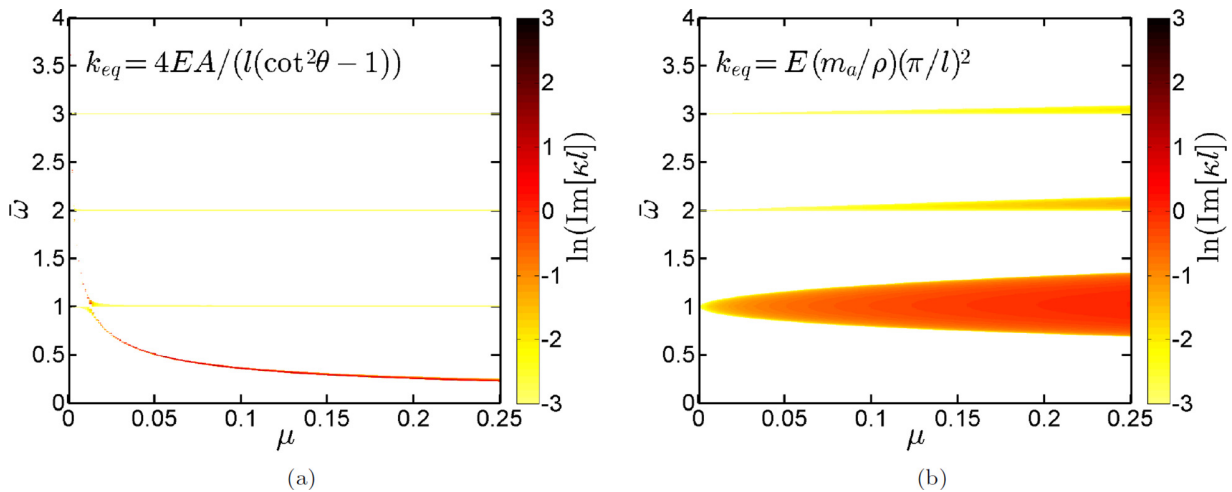


FIG. 11. Attenuation profiles illustrating the effect of the mass ratio μ in a standard local resonance configuration. (a) Stiffness tuning for similar first peak attenuation frequency. (b) Stiffness tuning for local-resonance-Bragg coalescence.

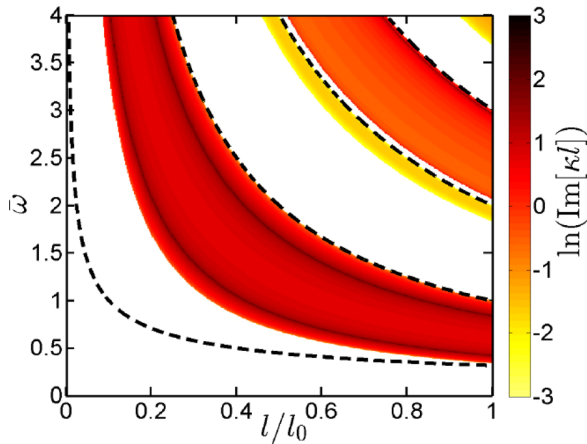


FIG. 12. Attenuation profile illustrating the dependence on unit-cell size. Local resonator: dashed lines, Inertial amplifier: colored regions.

frequency with mass increase. Comparing to the inertial amplification system for $l_1 = l_3 = 0$, the inertial amplification system is seen to perform better in terms of both gap width and depth, see Fig. 8. The attenuation profile for local-resonance-Bragg coalescence in Fig. 11(b) shows superior gap width than seen for the local-resonance attenuation profile in Fig. 11(a); however, the lowest and widest gap is centred around the first Bragg-gap frequency, thus not providing any low-frequency attenuation. Furthermore, the inertial amplification configuration still offers a wider and deeper gap, while being lower in frequency.

F. Effect of unit-cell size

Now the attenuation profile for the inertial amplification system is compared to that of a local resonance system when the unit-cell size is decreased. This is done to examine the practical limitation of the inertial amplification system, given that an internal length is needed to generate the enhanced inertia to cancel the elastic forces in the rod. This limitation is similar to the one investigated in Sec. IV C concerning the internal length between attachment points, \bar{l} ; however, now we look into the unit cell size l rather than relative internal length. The standard local resonance system does not need any internal length and, as such, can operate unaltered as the unit-cell size goes towards zero. Figure 12 compares the attenuation profile for the two systems, when decreasing the unit cell size l/l_0 for the parameters seen in Table III, where both μ and \bar{k}_{eq} are based on the original length l_0 . The dashed lines represent the gap frequencies for the local-resonator system. The first line represents the local resonance frequency $\omega_{eq} = \sqrt{k_{eq}/m_a}$ where k_{eq} is kept constant, while m_a decreases with unit cell size as μ is kept constant. The subsequent lines represent the Bragg-gap limits $\omega_{Bragg} = j\omega_b, j = 1, 2, 3, \dots$. For this particular mass ratio

TABLE III. Parameters for unit-cell size investigation.

l_0 (m)	μ	θ (rad)	\bar{k}_{eq}	$l_1 = l_3$
0.55	0.1	$\pi/18$	0.1	0

$\mu = 10\%$, the actual gaps are very narrow. Thus, they are covered entirely by the line representation in Fig. 12.

The conclusion in this section is that for realistic and comparable parameters, the local-resonance system can provide wave attenuation at lower frequencies than the inertial-amplification system, as the unit-cell size decreases. This is a clear advantage of the classical locally resonant systems from the point of view of constraints on unit-cell size.

V. FINITE STRUCTURES

In this section, the band-structure results from Section IV are compared to the transmissibility for finite systems comprising a certain number of unit cells, illustrating that the material results are representative in a structural setting as well. The transmissibilities are calculated from a finite-element model of the continuous-discrete system in Fig. 3, using standard linear elements to discretize the continuous rod, with stiffness and mass matrix contributions from the mechanism at appropriate nodes. The simple FE model is compared to an FE model created in the commercial software ABAQUS, using 3D beam elements.

A. Transmissibility gaps

Using the FE implementation to model the 1D finite array illustrated in Fig. 13 with the number of unit cells denoted n , the transmissibility is expressed as the natural logarithm to the ratio between the output and input displacement divided by the number of unit cells. Hence, the transmissibility expresses the wave propagation/decay per unit cell, and is thus comparable to the dispersion curves.

The transmissibilities are calculated for the same aluminum rod as considered in Section IV, using the same rod parameters from Table I. We consider the case where the relative mechanism length is equal to the full unit cell length, i.e., $\bar{l} = 1$. Figure 14 compares the band structures from the infinite systems to the transmissibilities calculated using $n = 5$ for two values of the mass-ratio μ , illustrating the branching point at $\mu = 7\%$ and the double-dip at $\mu = 21\%$ corresponding to the single- and double-peak in the attenuation profiles, respectively. The grey areas correspond to band gaps predicted by the infinite model. It is noted that some boundary effects exist, i.e., the finite systems have resonances within band-gaps, which is due to the symmetry breaking of the system.^{29,30} In spite of the boundary effects, the comparison shows that the infinite-system properties carry over to the finite case, and perhaps equally important that within the band gaps, the curves for the imaginary part of the wavenumber and the transmissibility have similar shapes and magnitudes. This is expected from the exponential decaying behaviour of waves within the band gaps, but it does illustrate the design potential for finite structures by just considering the shape of the band-structure within the gaps calculated for infinite structures.

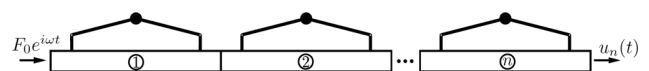


FIG. 13. Finite array.

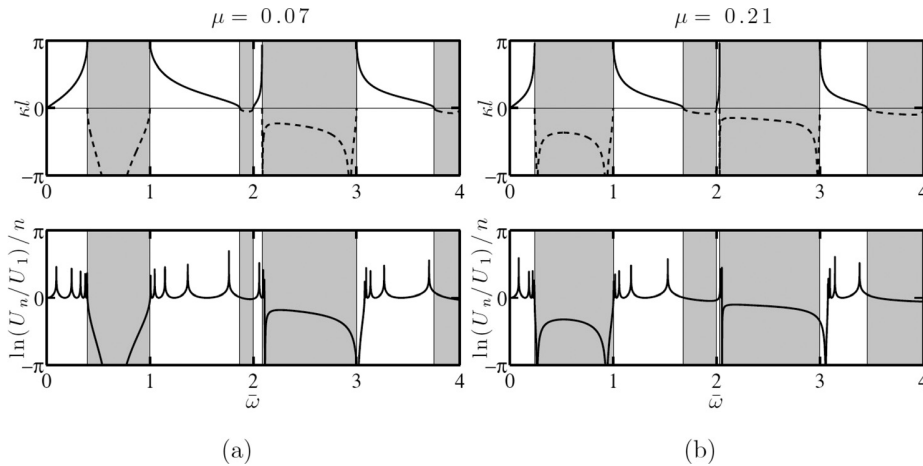


FIG. 14. Comparison of band structures to transmissibilities for $\bar{l} = 1$. (a) Single peak behaviour. (b) Double peak behaviour.

B. ABAQUS verification

The FE implementation of the hybrid rod-mechanism system is tested against an implementation of the finite system in the commercial FE-software ABAQUS. The ABAQUS model is created as a 3D deformable “wire” model, using three-dimensional beam elements for both rod and mechanism. The mechanisms are distributed above and below the main structure to have equal but opposite transverse force components from the mechanisms. This is necessary to avoid bending phenomena, and may easily be implemented in an experimental setting as well. The rigid connecting links are modelled by assigning very large Young’s modulus and very low density to the elements. The ideal connections are modelled using translatory constraints to connect the rigid connectors to the bar. Hence, the ABAQUS model is used to illustrate the phenomena in a finite setting without obstructing

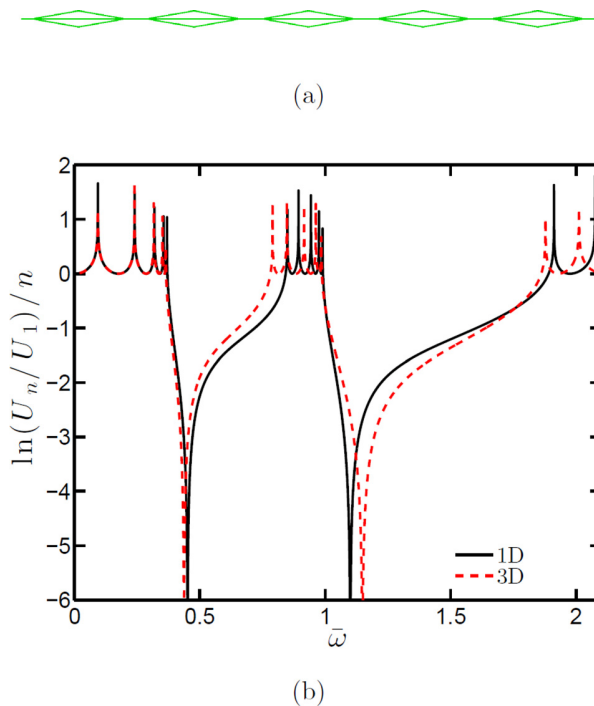


FIG. 15. (a) ABAQUS Model. (b) Comparison of 3D to 1D model. $\bar{l} = 0.8$, $\mu = 0.1$.

the results with, for the present purpose, unnecessary complexities. Indeed, it is a subject of a future research paper to investigate more realistic models of the physical configuration in Fig. 2 both numerically and experimentally. The ABAQUS model is created with the general rod parameters seen in Table I and the general mechanism parameters $\theta = \pi/18$ and $\bar{l} = 0.8$. An illustration of the created ABAQUS model is seen in Fig. 15(a).

Figure 15(b) shows the comparison between the transmissibilities calculated by the 1D FE implementation of the rod-mechanism system and the 3D FE implementation in ABAQUS, respectively, for the mass ratio $\mu = 10\%$.

Comparing both maximum attenuation frequencies and gap limits, the transmissibility predicted by ABAQUS matches rather well, especially for the first gap. Concerning the deviations in the transmissibilities, it is worth considering the case of gap-coalescence which, as seen in Fig. 9, is a rather “singular” phenomena. As expected, using the “coalescence-parameters” predicted by the analytical model does not cause the gaps to coalesce in the 3D model. Figure 16 shows the transmissibility comparison for the analytically predicted coalescence-parameters and the ones found by inverse analysis in ABAQUS. This pass band could be detrimental for design if not taken into account, since the resonances are so closely spaced. Hence, designing for gap-coalescence should be done with care, as mentioned in Sec. IV C.

VI. CONCLUSIONS

We have investigated the wave characteristics of a continuous rod with a periodically attached inertial amplification mechanism. The inertial amplification mechanism, which is based on the same physical principles as the classical inerter, creates band gaps within the dispersion curves of the underlying continuous rod. The gap-opening mechanism is based on an enhanced inertial force generated between two points in the continuum, proportional to the relative acceleration between these two points. An inertial amplification mechanism has been used previously as a core building block for the generation of a lattice medium, rather than serve as a light attachment to a continuous structure as done here. Several prominent effects are featured in the emerging band structure of the hybrid rod-mechanism configuration. The anti-

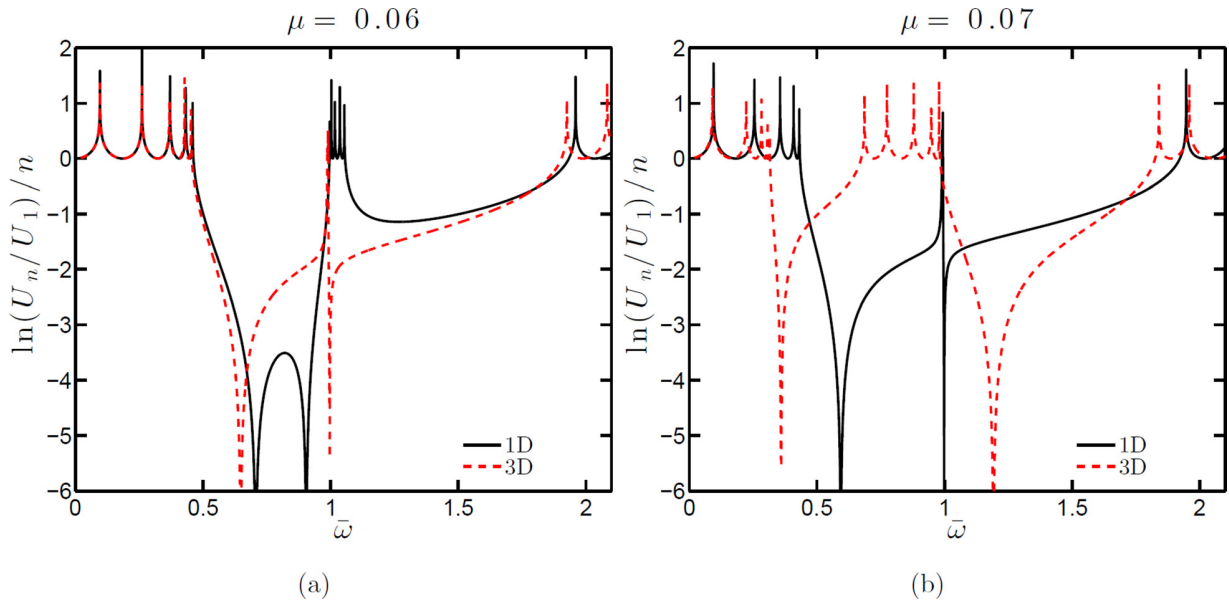


FIG. 16. Transmissibility comparison for coalescence in 1D and 3D models for (a) $\mu = 0.06$ and (b) $\mu = 0.07$.

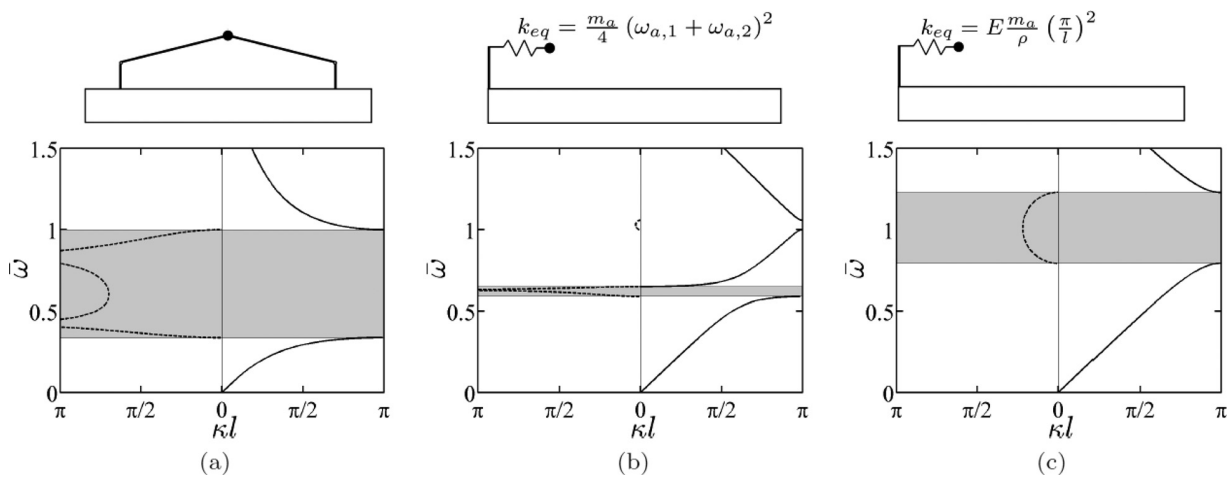


FIG. 17. Various band-gap opening mechanisms for constant mass ratio $\mu = 10\%$ $\bar{l} = 1$. (a) Inertial amplification. (b) Local resonance. (c) Bragg scattering.

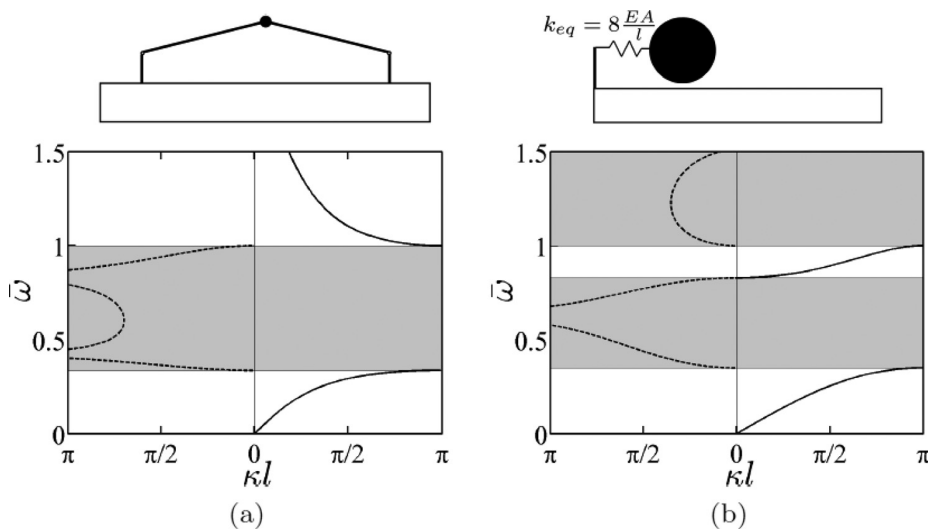


FIG. 18. Band structure for (a) proposed inertially amplified rod with $\mu = 10\%$, $\bar{l} = 1$ and (b) standard locally resonant rod with $\mu = 204\%$. The systems have almost equal-sized gaps despite a factor of 20 difference in added mass size.

resonance frequencies are governed by both mechanism- and rod-parameters. Hence, rather than a single anti-resonance frequency, we see an infinite number (by virtue of the continuous nature of the underlying rod), all of which can be predicted for a simple choice of unit-cell parameters. For an example choice of parameters, we illustrate the presence of multiple attenuation peaks within the same gap. Furthermore, when generalizing the parameters of the unit cell, we observe that the anti-resonance frequencies can jump between gaps whereby double-peak behaviour cannot be guaranteed for all parameters. At the specific values of the anti-resonance jump, band-gap coalescence emerges providing a very wide and deep contiguous gap. This gap, however, is rather sensitive to design and modelling inaccuracies.

In addition to these intriguing effects, we demonstrate how attaching an inertial amplification mechanism to a continuous structure may be practically superior to attaching a classical local resonator in that the former produces much larger gaps for the same amount of added mass. Figure 17 compares the band structure of the proposed inertial amplification system to those of a classical local resonator configuration for two different tunings of the local resonator stiffness k_{eq} . Figures 17(b) and 17(c) represent two cases of stiffness tuning that provide a locally resonant band gap (with equal central frequency) and a Bragg coalescence gap, respectively. The central frequency is determined by solving Eq. (17) numerically for the first two roots, $\omega_{a,1}$ and $\omega_{a,2}$. The comparison illustrates that when the same mass is used, the proposed concept achieves a first gap that is much wider than what is obtainable by the classical local resonator configuration, irrespective of the stiffness tuning for the local resonator. In order to obtain comparable performance in terms of band-gap width for the classical local-resonator system, the added mass m_a should be increased significantly. Figure 18 compares similar gap widths for an inertial amplification system and a local resonance system. From the figure, we see that the inertial amplification system is superior in terms of the magnitude of added mass, as the local resonance system requires an approximately twenty times heavier mass to obtain a comparable band-gap width (a mass that is more than two times as heavy as the rod it is attached to). The classical local resonator configuration, on the other hand, faces less constraints on unit-cell size as demonstrated in Fig. 12.

The presented concept of an inertially amplified continuous structure opens a new promising avenue of band-gap design. Potentially, it could be extended to surfaces of more complex structures such as plates, shells, and membranes leading to a general surface-coating design paradigm for wave attenuation in structures. Steps toward achieving this goal include a generalization of the formulation to admit transverse vibrations, incorporation of frictional stiffness and damping in the bearings of the mechanism, and generalization to two dimensions.

ACKNOWLEDGMENTS

Niels M. M. Frandsen and Jakob S. Jensen were supported by ERC starting Grant No. 279529 INNODYN.

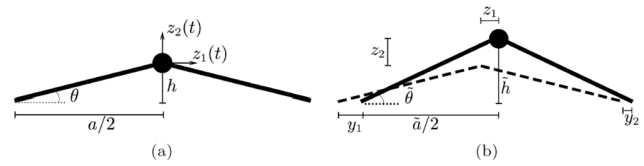


FIG. 19. Top triangle kinematics. (a) Undeformed triangle. (b) Deformed triangle.

Osama R. Bilal and Mahmoud I. Hussein were supported by the National Science Foundation Grant No. 1131802. Further, N.M.M.F would like to extend his thanks to the foundations: COWIfonden, Augustinusfonden, Hede Nielsen Fonden, Ingeniør Alexandre Haymnan og Hustrus Fond, Oticon Fonden and Otto Mønsted Fonden. All authors are grateful to graduate student Dimitri Krattiger for his assistance in generating the image of Figure 1.

APPENDIX: KINEMATIC DERIVATION

Considering the top part of the deformed mechanism as illustrated in Fig. 19, the motions z_1 and z_2 can be determined in terms of y_1 , y_2 , and θ . The horizontal motion z_1 is by geometric consideration determined as $z_1 = (y_1 + y_2)/2$. The vertical motion is given by the difference $z_2 = \tilde{h} - h$. It turns out to be convenient to consider the difference of the squared triangle heights

$$\begin{aligned} \tilde{h}^2 - h^2 &= \left(l^2 - \left(\frac{\tilde{a}}{2} \right)^2 \right) - \left(l^2 - \left(\frac{a}{2} \right)^2 \right) \\ &= \frac{a^2}{4} - \frac{(a + y_2 - y_1)^2}{4} \\ &= \frac{1}{4} \left(2a(y_2 - y_1) - (y_2 - y_1)^2 \right). \end{aligned} \quad (\text{A1})$$

Expressing the difference in squared heights as $\tilde{h}^2 - h^2 = (\tilde{h} + h)(\tilde{h} - h) = (2h + z_2)z_2$ and using a geometric relation for h lead to

$$(z_2 + a \tan \theta)z_2 = \frac{1}{4} \left(2a(y_2 - y_1) - (y_2 - y_1)^2 \right), \quad (\text{A2})$$

which provides a quadratic equation in z_2 . The equation is made explicit by assuming small displacements such that $(y_2 - y_1)^2 \ll 2a(y_2 - y_1)$ and $z_2 \ll a \tan \theta = h$, whereby the linearized kinematics of the mechanism has been determined as

$$z_1 = \frac{1}{2}(y_2 + y_1), \quad (\text{A3a})$$

$$z_2 = \frac{1}{2} \cot \theta (y_2 - y_1). \quad (\text{A3b})$$

¹C. Kittel, *Introduction to Solid State Physics* (Wiley, New York, 1976).

²L. Brillouin, *Wave Propagation in Periodic Structures* (Dover Publications, 1953).

³C. Elachi, *Proc. IEEE* **64**, 1666 (1976).

⁴D. Mead, *J. Sound Vib.* **190**, 495 (1996).

⁵M. I. Hussein, M. J. Leamy, and M. Ruzzene, *Appl. Mech. Rev.* **66**, 040802 (2014).

- ⁶H. Frahm, "Device for damping vibration of bodies," U.S. Patent 989,958A (1911).
- ⁷Z. Liu, X. Zhang, Y. Mao, Y. Y. Zhu, Z. Yang, C. T. Chan, and P. Sheng, *Science* **289**, 1734 (2000).
- ⁸D. Yu, Y. Liu, G. Wang, L. Cai, and J. Qiu, *Phys. Lett. A* **348**, 410 (2006).
- ⁹D. Yu, Y. Liu, G. Wang, H. Zhao, and J. Qiu, *J. Appl. Phys.* **100**, 124901 (2006).
- ¹⁰Y. Pennec, B. Djafari-Rouhani, H. Larabi, J. O. Vasseur, and A. C. Hladky-Hennion, *Phys. Rev. B* **78**, 104105 (2008).
- ¹¹T.-T. Wu, Z.-G. Huang, T.-C. Tsai, and T.-C. Wu, *Appl. Phys. Lett.* **93**, 111902 (2008).
- ¹²C. Yilmaz, G. M. Hulbert, and N. Kikuchi, *Phys. Rev. B* **76**, 054309 (2007).
- ¹³C. Yilmaz and G. Hulbert, *Phys. Lett. A* **374**, 3576 (2010).
- ¹⁴G. Acar and C. Yilmaz, *J. Sound Vib.* **332**, 6389 (2013).
- ¹⁵C. Yilmaz and N. Kikuchi, *J. Sound Vib.* **293**, 171 (2006).
- ¹⁶M. C. Smith, *IEEE Trans. Autom. Control* **47**, 1648 (2002).
- ¹⁷M. Z. Q. Chen, C. Papageorgiou, F. Scheibe, F. C. Wang, and M. Smith, *IEEE Circuits Syst. Mag.* **9**, 10 (2009).
- ¹⁸O. Yuksel and C. Yilmaz, *J. Sound Vib.* **355**, 232 (2015).
- ¹⁹C. Papageorgiou, N. E. Houghton, and M. C. Smith, *J. Dyn. Syst., Meas., Control* **131**, 011001 (2009).
- ²⁰W. L. Mochan, M. d. C. Mussot, and R. G. Barrera, *Phys. Rev. B* **35**, 1088 (1987).
- ²¹R. Esquivel-Sirvent and G. H. Coccoletzi, *J. Acoust. Soc. Am.* **95**, 86 (1994).
- ²²M. I. Hussein, G. M. Hulbert, and R. A. Scott, *J. Sound Vib.* **289**, 779 (2006).
- ²³R. E. D. Bishop, *The Mechanics of Vibration* (Cambridge University Press, 1979).
- ²⁴F. Bloch, *Z. Phys.* **52**, 555 (1929).
- ²⁵Y. Xiao, B. R. Mace, J. Wen, and X. Wen, *Phys. Lett. A* **375**, 1485 (2011).
- ²⁶L. Liu and M. I. Hussein, *J. Appl. Mech.* **79**, 011003 (2012).
- ²⁷R. Khajetourian and M. I. Hussein, *AIP Adv.* **4**(12), 124308 (2014).
- ²⁸Y. Xiao, J. Wen, and X. Wen, *New J. Phys.* **14**, 033042 (2012).
- ²⁹B. Djafari-Rouhani, L. Dobrzynski, O. H. Duparc, R. E. Camley, and A. A. Maradudin, *Phys. Rev. B* **28**(4), 1711 (1983).
- ³⁰J. S. Jensen, *J. Sound Vib.* **266**, 1053 (2003).

DTU Mechanical Engineering
Section of Solid Mechanics
Technical University of Denmark

Nils Koppels Allé, Bld. 404
DK-2800 Kgs. Lyngby
Denmark
Phone (+45) 4525 4250
Fax (+45) 4593 1475
www.mek.dtu.dk
ISBN: 978-87-7475-450-3

DCAMM
Danish Center for Applied Mathematics and Mechanics

Nils Koppels Allé, Bld. 404
DK-2800 Kgs. Lyngby
Denmark
Phone (+45) 4525 4250
Fax (+45) 4593 1475
www.dcammm.dk
ISSN: 0903-1685